Temperature and Freshwater Fluxes by Individual Eddies in the North Atlantic Ocean

Vom Fachbereich für Physik und Elektrotechnik der Universität Bremen genehmigte Dissertation zur Erlangung des akademischen Grades Doktor der Naturwissenschaften (Dr. rer. nat.)

vorgelegt von: Vasco Müller
aus Aachen

1. Gutachterin: Dr. Dagmar Kieke
2. Gutachter: Prof. Dr. Paul G. Myers

Eingereicht am: 21.08.2017
Tag des Promotionskolloquiums: 25.09.2017

Declaration of Originality

I, Vasco Müller, certify that the work presented here is, to the best of my knowledge and belief, original and the result of my own investigations, except as acknowledged, and has not been submitted, either in part or whole, for a degree at this or any other University. Large parts of Chapter 2 and Chapter 3, have been published in the peer-reviewed *Journal of Geophysical Research*, (Müller et al., 2017). The text of the previously published chapters has been partially adapted in order to fit the context of a thesis.

Vasco Müller 21.08.2017

Abstract

This study investigates the temperature and freshwater fluxes by individual eddies in the North Atlantic between 40°-55°N and 60°-10°W for the period January 1993 to April 2014. Focus is on a zonal section along 47°N, roughly at the boundary between the subpolar and the subtropical gyres. The main question is to what extent eddies are responsible for the variability and mixing in the region and how the anomalies of temperature and freshwater carried by eddies contribute to the overall fluxes across 47°N.

Almost 37000 eddies with a lifetime longer than one week are detected from surface geostrophic velocity fields derived from satellite-altimetry. First, only surface temperature fluxes based on collocating detected eddies with sea surface temperature observations from satellites are analyzed. The results are compared to two model simulations spanning the period from 2002 to 2013 with different horizontal resolution (1/4° and 1/12°), allowing to assess the impact of different resolution on the results. The analysis is then extended to three dimensional temperature and freshwater fluxes. The temperature and salinity fields used for the calculation of the fluxes stem from a new product that was derived from dynamic height using the Gravest Empirical Mode (GEM) technique. Using this new product allows for the first time to relate every detected eddy to profiles of temperature and freshwater and to analyze the respective fluxes across 47°N. Since the 1/12° model configuration shows the more realistic results for the surface temperature fluxes, the comparison of the observed temperature and freshwater fluxes is confined to this configuration.

The highest number of eddies is found along the pathway of the North Atlantic Current (NAC), roughly following the 4000 m isobath, and on the Grand Banks of Newfoundland. The typical vertical extent is around 1400 m, with anti-cyclonic eddies on average 200 m deeper than cyclonic eddies. Relating the observed eddies to the top-to-bottom velocity distribution from ship observations shows that the highest fluxes are linked to the fastest and most pronounced current branches in the western Newfoundland Basin.

The time series of surface temperature fluxes by eddies crossing 47°N reveal that single isolated eddies with large SST signatures contribute ∼25% to the surface temperature flux. Similarly, ∼15-35% of the three dimensional temperature and freshwater fluxes across 47°N stem from eddies with large temperature and freshwater anomalies. The largest contribution to the flux by individual eddies stems from cold and fresh eddies originating from the Western Boundary Current moving northward with the NAC. While the fluxes by individual eddies are very small compared to the basin-wide integrated total fluxes, eddies induce a large part of the variability of the total flux. The effect of fluxes by individual eddies is regionally confined, but eddies contribute to the cooling of the NAC in the region around the Grand Banks of Newfoundland, to the local recirculation in the Newfoundland Basin, and in part to the interior southward pathway of subpolar water.

Contents

List of Tables

List of Figures

1 Introduction

1.1 Heat and Freshwater Fluxes - From Global to Regional Scales

The world's oceans are an integral part of the climate system and play a key role for the global distribution of heat and freshwater. Due to the meridional imbalance of incoming short-wave solar radiation and outgoing long-wave radiation, the Earth takes up more heat in low latitudes than in high latitudes (Figure 1.1).

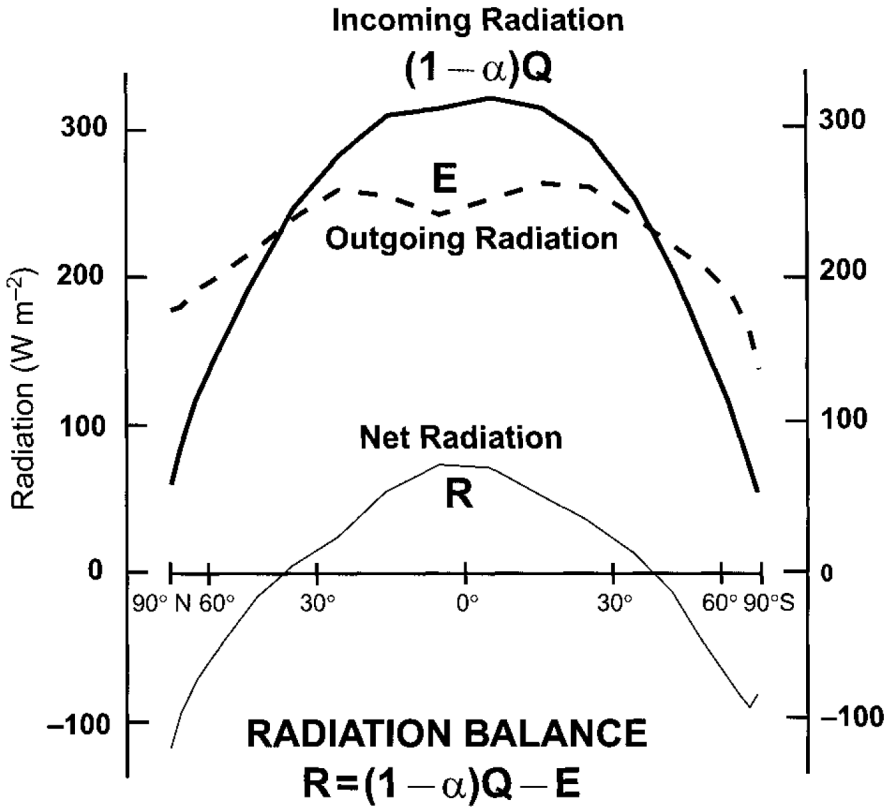

Figure 1.1: Latitudinal profiles of the top-of-the-atmosphere net incoming short-wave radiation $(1-\alpha)\,Q$, where α is the albedo and Q the incoming solar radiation, outgoing long-wave radiation E, and the net radiative heating of the Earth R (Bryden and Imawaki, 2001, their Figure 6.1.2).

In general, the surplus of heat in equatorial regions has to be transported away from the equator towards higher latitudes by the ocean and the atmosphere in order to maintain the energy balance of the Earth. The combined transport of the atmosphere and the ocean reaches up to ±5.5 PW (1 PW = 10^{15} W) around 35°N/S (e.g., Trenberth and Solomon, 1994; Bryden and Imawaki, 2001; Wunsch, 2005). Trenberth and Solomon (1994) estimated the oceanic fraction to account for 50% of the combined transport at around 20°N. Equatorward of this latitude, the oceanic fraction dominates the total heat transport, while the atmospheric fraction dominates the total transport in higher latitudes (Figure 1.2a).

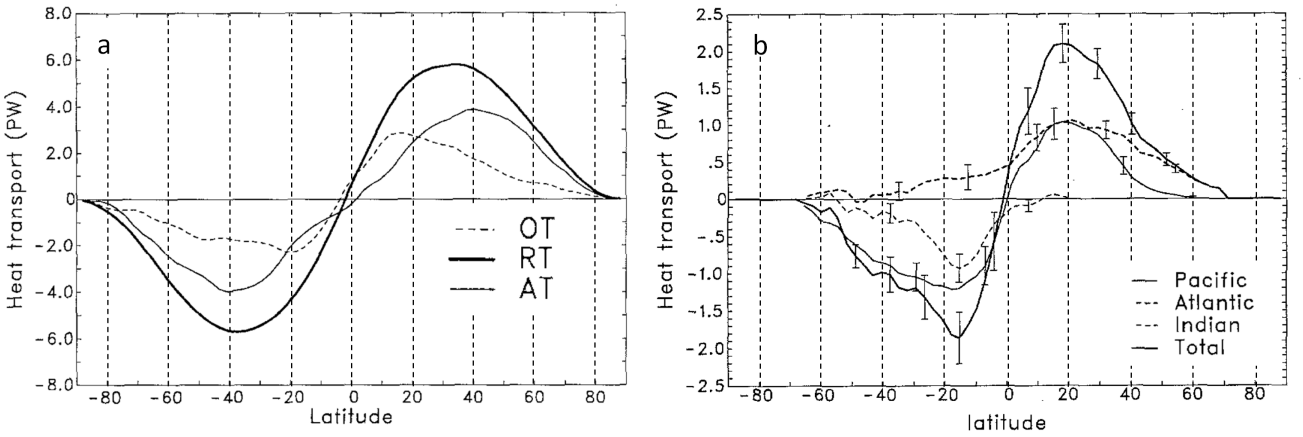

Figure 1.2: The top-of-the-atmosphere required northward heat transport from satellite radiation measurements RT, the estimated atmospheric transports AT, and the ocean transports OT computed as a residual (a). The poleward ocean heat transports in each ocean basin and summed over all oceans (total), as computed from the net flux through the ocean surface (b). Both plots show data from the Earth Radiation Budget Experiment for the year 1988. The figures are adapted from Trenberth and Solomon (1994, their Figures 16 and 17).

The mechanism responsible for most of the oceanic heat transport (almost 90% in mid-latitudes of the Atlantic, Johns et al., 2011) is the Meridional Overturning Circulation (MOC, Figure 1.3). This global circulation, also referred to as "global conveyor belt", can be separated into different components with different driving mechanisms: the buoyancy driven thermohaline circulation (THC) on the one hand and a system of wind driven surface currents on the other hand. The terms THC and MOC have both been used to describe the overturning phenomenon, but it is important to notice that in fact they are not synonyms (Wunsch, 2002). THC implies that the overturning is driven by buoyancy loss, while MOC does not imply any driving mechanism and is well-defined as the streamfunction of the entire meridional velocity field (Kuhlbrodt et al., 2007).

The main features of the global circulation are warm surface currents, cold deep currents, deep water formation regions, and upwelling regions (Figure 1.3). Deep water formation regions are located in the Nordic Seas, in the Labrador Sea, and around Antarctica where the stratification is weak and a strong buoyancy loss is induced by cold winds as well as sea-ice formation. The circulation is closed by mixing-driven (energy from tides and wind) upwelling in the subtropical gyres and wind-driven (Ekman) upwelling around Antarctica (e.g., Wunsch, 2002; Kuhlbrodt et al., 2007).

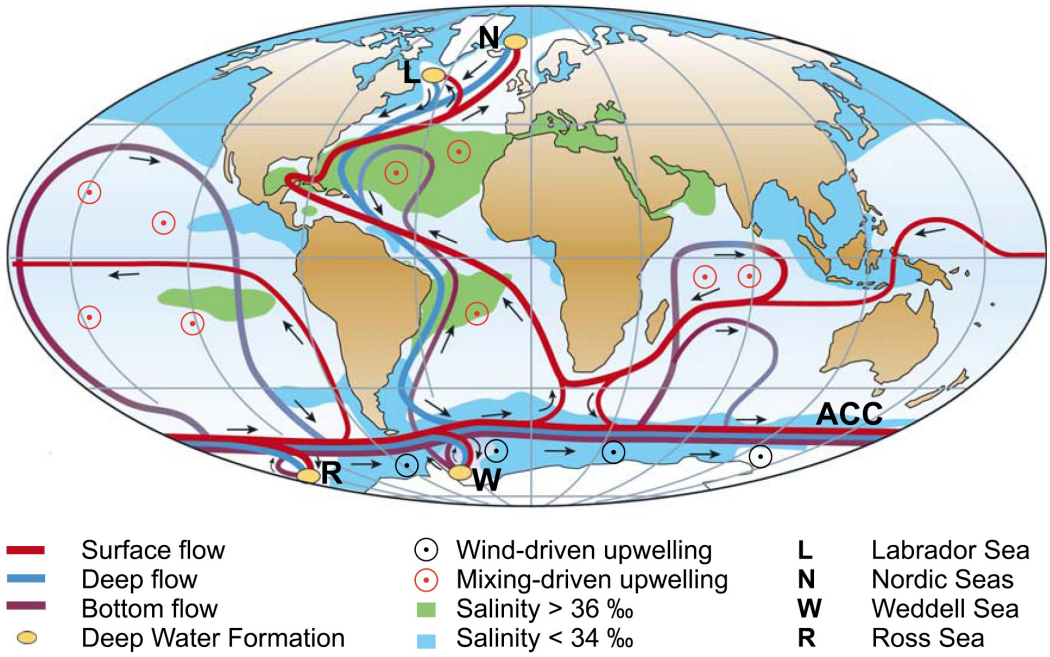

Figure 1.3: Sketch of the global overturning circulation system (Kuhlbrodt et al., 2007, their Figure 1)

The Atlantic part of this overturning circulation (AMOC) plays an exceptional role in the global circulation system (Figure 1.3 and Figure 1.2b). With a maximum northward heat transport between 1.3 PW (McCarthy et al., 2015) and 1.8 PW (Ganachaud and Wunsch, 2003), the Atlantic Ocean accounts for up to 25% of the combined oceanic and atmospheric northward heat transport.

The outstanding feature of the AMOC is the northward heat transport at almost all latitudes (Figure 1.2b). While all other oceans transport heat polewards from the equator, the transport in the Atlantic is directed northward almost everywhere. The reason for this exceptional characteristic can be found in the northern parts of the Atlantic. Only in the North Atlantic can water reach such high latitudes and therefore lose immense amounts of heat to the atmosphere, leading to the formation of deep water. This exceptional heat loss is compen-

sated by the continuous northward heat transport in the Atlantic. The mild western European climate is an effect of the continuous northward (and later on eastward) transport of heat by the AMOC and the atmosphere (e.g., Rhines et al., 2008).

Since eddies are the main focus of this thesis, I will give some examples of their role in the global circulation system and for the overall northward heat transport in the Atlantic. Eddies are relatively small (horizontal scale on the order of 100 km) swirling coherent vortices that are omnipresent in the ocean. They can carry water from their respective source region inside their cores and entrain surrounding water into their outer ring. The properties of these waters (e.g. temperature, salinity, oxygen or nutrients) are then transported with the eddy over longer distances and released gradually by mixing or more abruptly when the eddy decays (e.g., Robinson, 1983). In order to avoid misunderstandings, it is important to differentiate between "eddy" in the sense of a coherent vortex in the ocean and "eddy" in the sense of the turbulent component of a variable. In geophysical fluid dynamics, variables are often separated into a mean state and a turbulent component ($x = \overline{x} + x'$). In many cases, the high frequency component x' is also called "eddy" component. In this thesis, the term eddy always refers to coherent vortices unless explicitly stated otherwise (e.g. eddy kinetic energy). I will adhere from calling eddies vortices because many publications use the terms vortex and eddy interchangeable and there are ambiguous definitions for the term vortex (e.g., Jeong and Hussain, 1995).

One famous example of eddies in the Atlantic transporting water masses for long distances are Agulhas Rings. These large anticyclonic eddies are formed at the southern tip of Africa where the Agulhas Current retroflects eastwards back into the Indian Ocean (e.g. Biastoch et al., 2008). This so-called Agulhas leakage transports warm and saline water from the Indian Ocean northwestward across the Southern Atlantic, feeding into the North Brazil Current (NBC) and providing a northward heat transport across the equator. Agulhas Rings therefore play an important role in the global climate system (e.g., Beal et al., 2011).

Around 8°N the NBC retroflects eastward into the North Equatorial Countercurrent (NECC), shedding anticyclonic eddies (e.g., Fratantoni and Glickson, 2002). Part of the flow continues into the Caribbean Sea in the form of these so-called NBC Rings (e.g., Goni and Malanotte-Rizzoli, 2003). Just as Agulhas Rings, NBC Rings contribute to the overturning in the Atlantic by carrying water from the South Atlantic into the Northern Hemisphere. Their transport also

modulates the inflow into the Caribbean Sea and thus can have an impact on the variability of the AMOC (Mertens et al., 2009).

Eddies also influence the AMOC and the related meridional fluxes on smaller scales. Marsh et al. (2009) compared model simulations with different horizontal resolution (1/4° and 1/12°) in order to study the effects of different representations of eddies on the overturning in the Atlantic and on the meridional heat transport. The largest differences in the "non-MOC" component of the transport (i.e. total heat transport minus overturning component) are found in mid-latitudes (35°N - 55°N), where ocean eddies are most energetic (Marsh et al., 2009, their Figure 3c). This could be caused by a different representation of the North Atlantic Current due to higher resolution and/or by a better representation of the high frequency heat fluxes. Smith et al. (2000) have shown that higher horizontal resolution leads to a more realistic representation of the North Atlantic Current. Wunsch (1999) and Volkov et al. (2008) both suggest that "eddy" (i.e. high frequency) heat fluxes, while small in the oceanic interior, are significant in western boundary current regions and also significantly contribute to the variability of the total heat transport.

Similarly to heat, also freshwater input is not distributed evenly over all latitudes. Evaporation (E), precipitation (P), and runoff from land (R) vary substantially between different regions. The overall flux between ocean and atmosphere (E-P-R) is negative (i.e. into the ocean) in the tropics and subpolar regions, while it is positive in the subtropical regions due to high evaporation and low rain (as shown in the recent estimate of the global freshwater cycle in the ocean by Schanze et al., 2010, their Figure 4). In order to gain a better understanding of the global hydrological cycle and its impact on the climate system it is crucial to understand and quantify the oceanic processes that close the balance between evaporation, precipitation, and runoff.

In the subpolar North Atlantic, freshwater is of special interest due to its impact on the formation of deep water. While the formation of deep water in the Labrador Sea varies substantially between individual years (e.g., Kieke and Yashayaev, 2015), a general freshening of the North Atlantic could permanently weaken the deep water formation due to the stabilizing effect of freshwater on the stratification. This in turn could slow down the overturning in the Atlantic as well as the global MOC. The possibility of this happening has been shown by reconstructing past climate responses to melting ice sheets (e.g., Rahmstorf, 2002; McManus et al., 2004) and by so-called water hosing experiments with ocean

models where freshwater is induced into the North Atlantic (e.g., Rahmstorf, 1995; Rahmstorf et al., 2005).

Especially the effects of increased freshwater input due to melt water from Greenland (e.g., Böning et al., 2016) and increasing inflow of freshwater from the Arctic (e.g., Yang et al., 2016) have been the focus of recent studies. While the results show that increased freshwater input into the North Atlantic indeed weakens the formation of deep water and could affect the AMOC, separating the direct influence from increased freshwater from inter-annual and decadal variations remains a challenging task.

Similar to heat flux by eddies, eddies have an influence on the distribution of freshwater in the ocean, on balancing the differences in E-P-R, and on the local stratification. For the subtropical North Atlantic, (e.g., Gordon and Giulivi, 2014) found that freshwater fluxes by eddies are a significant part of the marine hydrological budget, balancing more than 50% of the evaporation loss in this region. In the subpolar North Atlantic eddies carry freshwater e.g. from the West Greenland Current into the Labrador Sea and have been found to be an important factor for the restratification of the water column after a winter convection event (e.g., Lilly et al., 2003; Katsman et al., 2004).

1.2 The Subpolar North Atlantic - Main Circulation and Relevance of Eddies

The study region for this thesis is the subpolar North Atlantic. In the following the major current systems and the relevance of eddies in this region are presented in more detail.

Between 40°N - 55°N the North Atlantic is influenced by two vastly different regimes of currents and water masses: the subpolar gyre, a large-scale cyclonic circulation cell, and the anticyclonic circulation cell of the subtropical gyre. A well-defined meridional front, located off the shallow Grand Banks of Newfoundland that, to the east, widens and runs zonally, separates the warm subtropical gyre and the cold subpolar gyre. It is prominent in e.g. the spatial distribution of the mean sea surface temperature (SST) as well as the main circulation features (Figure 1.4).

In the Newfoundland Basin, the Western Boundary Current (WBC) and the North Atlantic Current (NAC) flow in different directions along the boundary of the two gyres. The deep reaching WBC originating in the north transports cold and fresh (subpolar) water southward, i.e. from the deep water formation

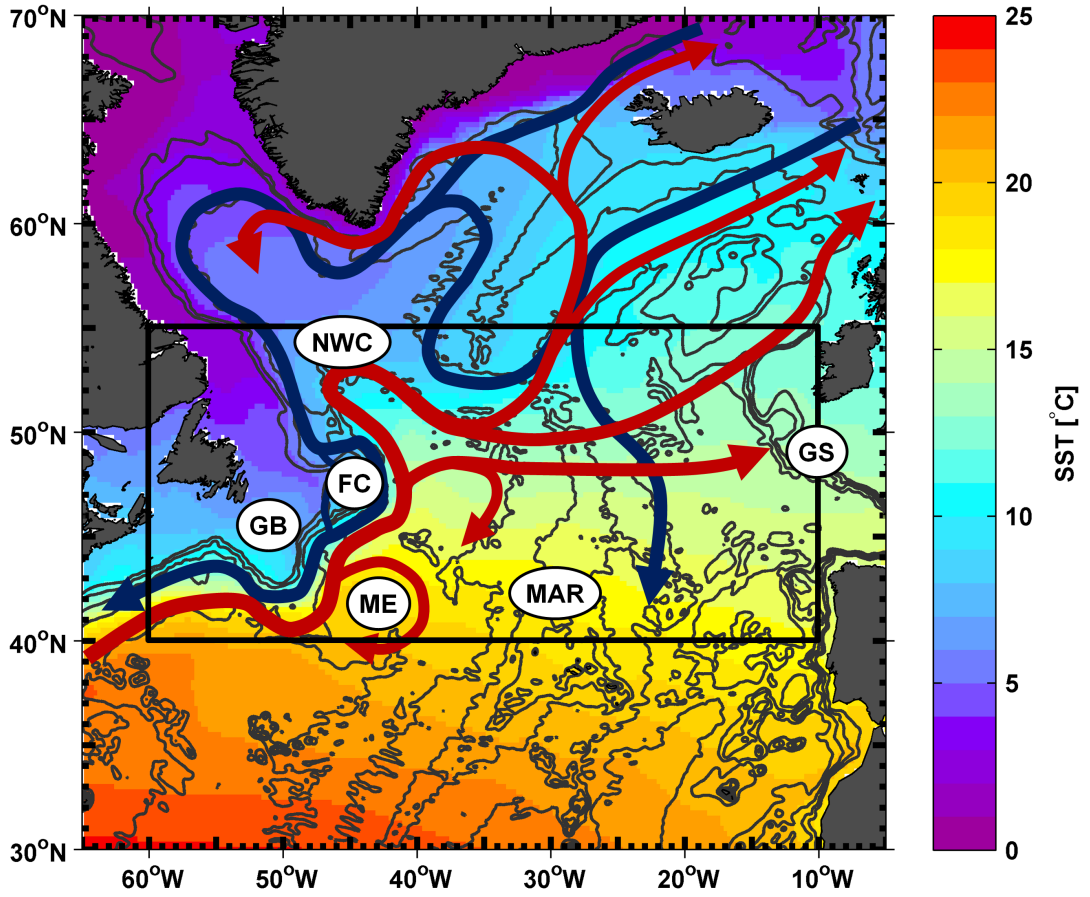

Figure 1.4: Overview of the study region (black box) in the subpolar North Atlantic with prominent topographic and circulation features (ME: Mann Eddy, GB: Grand Banks, FC: Flemish Cap, NWC: North West Corner, GS: Goban Spur, MAR: Mid-Atlantic Ridge). The background colors represent the mean NOAA Optimum Interpolation SST V2 for the period January 2002 to December 2013. Isobaths are given every 1000 m using bathymetry derived from the ETOPO1 data set (Amante and Eakins, 2009). The bathymetry is lowpass-filtered to highlight general features.

regions along the western continental margin towards lower latitudes (Figure 1.4). It feeds the cold limb of the AMOC, making the North Atlantic one of the key regions impacting the global climate (e.g., Marshall et al., 2001). Here, the term WBC will be used not only for the bottom intensified part of the deep southward flow, but for the total southward flow along the continental margin.

The NAC, on the other hand, is part of the warm limb of the AMOC. It transports warm, saline (subtropical) surface and subsurface waters as the continuation of the Gulf Stream (e.g., Rossby, 1996), as well as recirculating subpolar gyre water from the boundary current in deeper layers (Mertens et al., 2014). Southeast of the Grand Banks of Newfoundland, the NAC flows in a northeastward direc-

tion, forming a permanent anticyclonic feature centered around 42°N and 44°W (the so-called Mann-Eddy) (Mann, 1967; Rossby, 1996). The NAC then follows the topography northward roughly along the 4000 m isobath and forms several recirculation cells in the Newfoundland Basin (Rossby, 1996; Kearns and Rossby, 1998; Mertens et al., 2014). Mertens et al. (2014) quantified the strength of this recirculation to be about 2/3 (80 Sv) of the total NAC transport crossing 47°N (110 Sv). At the so-called Northwest Corner, an anticyclonic feature located at around 52°N, the NAC turns eastward. The NAC then crosses the Mid-Atlantic Ridge (MAR), often splitting into different branches and alternating between different pathways close to or through the fracture zones located between 48°N and 53°N (Schott et al., 1999; Bower and von Appen, 2008).

On its way along the western continental margin, the NAC has to cross several topographic obstacles (e.g. New England -, Corner Rise -, and Newfoundland Seamounts) where it experiences disruptions, forms meanders, and sheds individual eddies (e.g., Rossby, 1996). This leads to regions of increased eddy kinetic energy (EKE, i.e. increased energy in the high frequency component of the velocity field) along the pathway of the NAC and in the Newfoundland Basin (Figure 3.1a) (e.g., White and Heywood, 1995; Rossby, 1996; Carr and Rossby, 2001; Fratantoni, 2001).

There is significant exchange between the boundary and the interior of the North Atlantic by subpolar water detaching from the WBC, as observed by Bower et al. (2009) and Kieke et al. (2009). This exchange was quantified by e.g. Bower et al. (2013) and Mertens et al. (2014). The southward flow of the WBC transports about 30 Sv of deep water ($\sigma_\Theta > 27.68$ kg m^{-3}) towards 47°N, with about 15 Sv leaving the WBC, recirculating northward between 42°N and 47°N and thus contributing to the deep NAC (Mertens et al., 2014).

All of the above mentioned studies and many more have shown that the region between 45°N - 50°N in the western subpolar North Atlantic is a highly dynamic region. In this region eddies and other mesoscale features are of great relevance for the local exchange and horizontal mixing and stirring of water masses from different origin and of different properties (e.g., Robinson, 1983; Abraham and Bowen, 2002; Waugh and Abraham, 2008). Fluxes by eddies can provide an important mechanism of cross-frontal transport between the subpolar and subtropical gyres of the North Atlantic (Dutkiewicz et al., 2001) and between the subpolar water from the WBC and the open ocean in the Newfoundland Basin (Bower et al., 2011, 2013). Using the 1/12° resolution FLAME model, Rhein et al. (2011) found that $\sim 60\%$ of the modeled heat flux variability at 47°N is caused

by the turbulent (i.e. high frequency) component of the velocity field. However, quantified knowledge on the role of individual eddies for this variability and the horizontal exchange is still limited, and their respective contribution needs to be investigated.

1.3 Eddy Formation Processes

Since eddies and the fluxes that are related to individual eddies are the main focus of this thesis, some processes that lead to instabilities of the flow and to the formation of eddies will be discussed in the following chapter.

In general, all motions in the ocean have to be a solution of the equations of motions. While there are many known steady solutions to the equations of motion, none of them has been found to be stable to small perturbations that inevitably occur in nature (Vallis, 2006). This means that every flow will form instabilities sooner or later. A detailed analysis of the conditions necessary for the formation of different instabilities can be found in books on geophysical fluid dynamics (e.g., Vallis, 2006; Olbers et al., 2012).

In the following, I will give examples of (i) barotropic instabilities and (ii) baroclinic instabilities, that give rise to the formation of eddies:

(i) Barotropic instabilities (or shear instabilities) can occur if there is a horizontal shear of the background velocity. As no vertical shear is needed for this form of instability, it can occur in a barotropic flow (hence the name). This type of instability transfers *kinetic energy* from the mean flow to the turbulent flow. The simplest case of a system giving rise to barotropic instabilities is a flow of constant density with a shear perpendicular to the fluid's mean velocity (Figure 1.5). A small perturbation of a fluid parcel in y-direction around $y = 0$ will grow exponentially and lead to the rise of instabilities of the flow (a so-called Kelvin-Helmholtz instability).

(ii) Baroclinic instabilities are the most common form of instabilities and omnipresent in both atmosphere and ocean. In the atmosphere, they give rise to weather patterns and in the ocean they are the major source of mesoscale eddy energy (e.g., Olbers et al., 2012). Baroclinic instabilities transfer *available potential energy* from the mean flow to the turbulent flow.

A simple way of looking at baroclinic instabilities is that of "sloping convection" (Vallis, 2006). In order to allow for baroclinic instabilities, the fluid has to be stably stratified and rotating. These two conditions allow for a system where density increases with depth (i.e. low density at the surface, high density at the

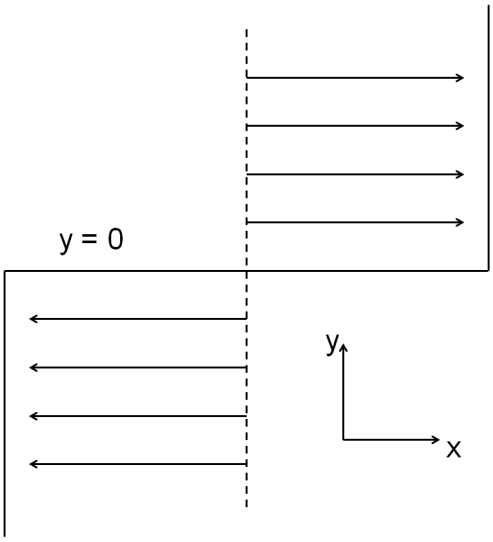

Figure 1.5: Schematic of a basic state flow giving rise to shear instabilities (Kelvin-Helmholtz instabilities) when perturbed. Figure adapted from Figure 6.1 in Vallis (2006).

bottom, $\rho_1 < \rho_2 < \rho_3 < \rho_4$) and with latitude (i.e. low density at the equator, high density at the poles). The rotation is necessary in order to balance the meridional pressure gradient that would otherwise cause the fluid to accelerate. A schematic of such a flow is shown in Figure 1.6.

So what happens to this fluid when it experiences a perturbation? Interchanging the fluid parcels 'A' and 'C', will lead to both parcels experiencing a restoring force since the fluid is stratified. However, if parcels 'A' and 'B' are interchanged, parcel 'A' is less dense than the new surrounding water and will be buoyant. At the same time it is located higher up in the water column than it was before. Parcel 'B' on the other hand, will be denser than the surrounding, have negative buoyancy and will be located lower than before. Thus, the overall center of gravity of the new system will be lower than before and therefore the potential energy will be lowered and converted into kinetic energy. The upward (downward) movement of the fluid parcels means that the water column is being vertically stretched (squeezed). This in turn induces cyclonic (anticyclonic) relative vorticity due to the conservation of potential vorticity.

Several studies have found analytical solutions for the necessary criteria when different background states give rise to baroclinic instabilities (e.g., Eady, 1949; Phillips, 1954). However, in order to find an analytical solution, the system has to be simplified so that the equations of motion are solvable. The model by Eady (1949) assumes no variations in the Coriolis Parameter (f-plane), a uniformly stratified fluid, a uniform vertical shear in the fluid, and the fact that the motion

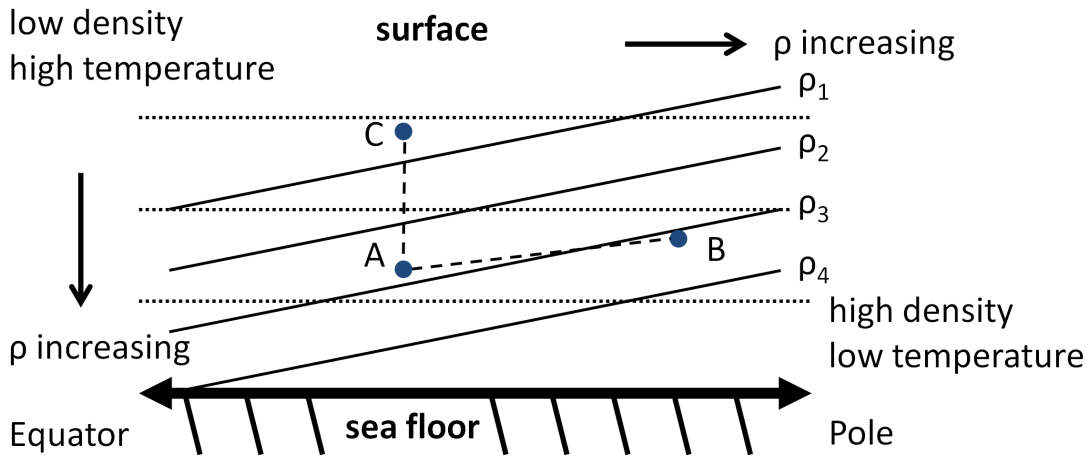

Figure 1.6: Schematic of a steady state giving rise to baroclinic instability. The fluid is stratified and density increases with depth and towards the poles ($\rho_1 < \rho_2 < \rho_3 < \rho_4$). Isopycnals are indicated by solid lines and isobars are indicated by dashed lines. The associated horizontal density gradient is balanced by the Coriolis force. Parcel 'A' is heavier than 'C', and so statically stable, but it is lighter than 'B'. Hence, if 'A' and 'B' are interchanged there is a release of potential energy. The Figure was adapted from Figure 6.9 in Vallis (2006).

happens between two rigid, flat surfaces. The model by Phillips (1954) takes into account meridional variations of the Coriolis parameter (β-effect), but the vertical structure is less resolved than in Eady's case. While these models greatly help with understanding the formation of instabilities and eddies, the assumptions necessary to find an analytical solution are not realistic for the ocean. Stratification and vertical shear in the ocean are far from uniform, and the seafloor is not flat. For more complex conditions, as they actually occur in the ocean (i.e. β-effect, non-uniform stratification, non-uniform shear, realistic bathymetry), only numerical solutions are possible.

The size of eddies formed by baroclinic instabilities is related to the baroclinic Rossby Radius. The n-th baroclinic Rossby radius is give by:

$$R_n = \frac{1}{n\pi\,|f|} \int_{-H}^{0} N\,(z)\,dz, \quad n \geq 1, \tag{1.1}$$

where $f = 2\Omega sin\,(\phi)$ is the Coriolis parameter for the Earth's rotation rate Ω and latitude ϕ, H is the water depth, and $N\,(z)$ is the Brunt-Väisälä frequency; $N = \sqrt{-\frac{g}{\rho_0}\frac{\partial\rho(z)}{\partial z}}$ (e.g., Chelton et al., 1998). This means the size of the Rossby radius is dominated by the Coriolis parameter f and therefore decreases with increasing latitude (and becomes relatively small in high latitudes). Observing mesoscale eddies, especially in high latitudes, can thus be a challenging task. A

brief overview of the development of eddy observations will be discussed in the following chapter.

1.4 Observations of Mesoscale Eddies

Mesoscale eddies in the ocean were first observed in the 1930s. During hydrographic cruises with the research vessel "Atlantis", Iselin (1936) found depressions of the isotherms between Nova Scotia and Bermuda and related this feature to an anticyclonic eddy. Another eddy was found south of Cape Sable. Already then, Iselin (1936) speculated that "deep whirls may be a more general characteristic of the waters bordering the northern edge of the Gulf Stream than is now realized".

Despite these early findings, it wasn't until the 1960s and 1970s that the role of eddies in the ocean was investigated more systematically (e.g., Fuglister, 1972; Doblar and Cheney, 1977; Richardson et al., 1978). Even though these studies were limited to a small number of observed eddies, they already found that the scales of mesoscale eddies range from tens to hundreds of km and tens to hundreds of days. The formation of eddies was mainly linked to baroclinic and shear instability processes of the boundary currents (e.g., Gill et al., 1974; Robinson, 1983). At this time, information about the distribution of eddies in space and time was still lacking due to the limited number of observations. Wyrtki et al. (1976) used observations of ship drift made by merchant ships to calculate global maps of the kinetic energy of the mean flow as well as the kinetic energy of the fluctuations (i.e. EKE). They found that the EKE is generally higher than the mean kinetic energy and highest in regions with the strongest mean flows. This supported the findings by Gill et al. (1974) that potential energy available in the mean circulation is converted into eddy energy by baroclinic instabilities.

The understanding of mesoscale eddies improved drastically with the introduction of satellite altimetry in the late 1970s. The *SeaSat* satellite, launched in 1978, was NASA's first Earth observation satellite dedicated solely to the remote sensing of the ocean. Among other sensors, it was equipped with a radar altimeter which allowed first global studies of mesoscale ocean variability (e.g., Cheney et al., 1983). However, the accuracy of the measurements was not sufficient for the detection of Rossby waves or individual mesoscale eddies (Fu et al., 1988). The TOPEX/POSEIDON satellite altimetry mission launched in the early 1990s was specifically designed for studying the circulation of the world's ocean (Fu et al., 1994). It revealed new insight on the short and long term ocean variability on a global scale focusing on the propagation of Rossby waves (e.g., Chelton and

Schlax, 1996) and the distribution of eddy kinetic energy in the ocean (e.g. Stammer, 1997). Lilly et al. (2003) used a "wavelet-based automated census algorithm for the alongtrack altimeter data" of TOPEX/POSEIDON in order to identify individual eddies in the Labrador Sea.

The quality of the altimetry product was greatly improved by merging data from different satellites which drastically increased the resolution (Chelton and Schlax, 2003) and eventually led to the SSALTO/Duacs multimission altimeter product (Le Traon et al., 1998; Ducet et al., 2000). This high resolution altimetry data set (initially 1/3°horizontal resolution, 1 week temporal resolution, later improved to the version used in this thesis) made it possible to detect mesoscale eddies directly from altimetry maps using automated eddy detection schemes (e.g., Chelton et al., 2007; Chaigneau et al., 2008; Nencioli et al., 2010; Chelton et al., 2011).

With the possibility to detect individual eddies from satellite altimetry it has become common practice to assess the role of individual eddies rather than the turbulent component of the velocity field. Dong et al. (2014) and Zhang et al. (2014) have demonstrated that it is possible to relate tracer anomalies (e.g. temperature, salinity) to individual eddies detected from satellite observations. This allows to follow the anomalies along the eddy's trajectory and calculate fluxes by individual eddies on a global scale.

However, data from the ocean interior is still scarce, which makes calculating three dimensional fluxes related to eddies so challenging. Both Dong et al. (2014) and Zhang et al. (2014) use data from autonomous profiling floats (so called Argo floats, `http://www.argo.ucsd.edu`, `http://argo.jcommops.org`). The Argo program is an international collaboration of 30 different countries aimed at collecting temperature and salinity profiles from the upper 2000 m. For this purpose autonomous profiling floats were released in the ocean that drift with the currents in a "parking depth" of around 1000 m. Typically every 10 days, the drifter sinks down to 2000 m and then ascends to the surface, measuring a profile of temperature and salinity in the water column. Once the float has reached the surface, the collected data is transmitted via satellite. Currently around 3800 Argo floats are being used in the world's oceans.

Even this seemingly high number of floats is by far not sufficient to relate every detected eddy to an anomaly of temperature and salinity. Both Dong et al. (2014) and Zhang et al. (2014) have to group Argo profiles into 5°×5° boxes in order to calculate an average background state of temperature and salinity. Furthermore, both studies have to rely on constructing composite profiles from Argo profiles

that are actually located inside of an eddy. The respective fluxes by eddies are then extrapolated from the composites by assuming the other eddies in the 5°×5° box have the same structure.

1.5 Modeling Mesocscale Eddies - Parametrization and Resolution

Since observing mesoscale eddies is such a challenging task, numerical models can be a great tool to help understanding the involved processes and dynamics. One great advantage of models is the availability of complete fields for any variable, especially in the deep ocean. However, modeling mesoscale eddies is far from being trivial since they are usually too small to be directly resolved by the model grid. This is a problem for ocean models because the kinetic energy of mesoscale features is larger than the kinetic energy of the mean flow in most parts of the world's ocean (e.g., Robinson, 1983). Many small scale processes (such as eddies) therefore have to be implemented into ocean models by parametrization (depending on the model's resolution).

Since gravity induces a strong anisotropy between the lateral and vertical motions in the ocean, these subgrid-scale processes can be separated into a horizontal (D^h) and a vertical component (D^v) (e.g., Madec and the NEMO team, 2008). The vertical turbulent fluxes are assumed to depend linearly on the gradients of the respective tracers or momentum, similar to molecular diffusion. The vertical momentum and tracer diffusive operators are then of second order. For example for the vertical mixing of temperature this would mean: $D^{vT} = \frac{\partial}{\partial z}\left(A^{vT}\frac{\partial T}{\partial z}\right)$, with the vertical diffusivity parameter A^{vT}. For the momentum equation the term looks the same but with a vertical viscosity parameter A^{vm} instead of A^{vT}. The easiest case would be taking a constant A^{vm} and A^{vT}, but it is more reasonable to assume some dependency on the physical properties of the respective grid cell of the model (e.g., Brunt-Väisälä frequency N or Richardson number $Ri = \frac{N^2}{S^2}$, where S is the vertical shear of the horizontal velocity), or using a turbulent-closure model (e.g., Bougeault and Lacarrere, 1989).

In the horizontal direction there is turbulent mixing by eddies as well as by even smaller, submesoscale variability. If the horizontal model resolution is coarse and eddies are not explicitly resolved in the model all horizontal turbulent mixing can be parametrized in a single term. This term is similar to the vertical mixing parametrization and the lateral diffusive and dissipative operators are of second order (Madec and the NEMO team, 2008). The idea of accounting for

eddy mixing by using a horizontal diffusion scheme has already been used in very early models of the ocean (e.g., Bryan, 1969). However, since lateral mixing in the ocean happens mainly along isopycnals (which are not necessarily horizontal), a purely horizontal parametrization is not ideal. Redi (1982) introduced a scheme that rotates the horizontal diffusion tensor in order to take into account the slope of isopycnals, but also this parametrization still had great problems, especially when tracers are distributed nearly like potential density (Danabasoglu and McWilliams, 1995).
A simple diffusive mixing along isopycnals also does not affect the potential energy in the ocean, which - as discussed in chapter 1.3 - is the main source of turbulence and eddies caused by baroclinic instabilities. The lateral mixing parametrization by Gent and Mcwilliams (1990) first overcomes this problem by introducing an additional horizontal advection term to the isopycnal diffusion term. This advective term is related to eddies and reduces the potential energy in the ocean.

If the resolution of the model is high enough to resolve individual eddies, the horizontal diffusivity and viscosity have to be lower, so that the horizontal mixing is not overestimated. The role of subgrid-scale physics is then to "dissipate the energy that cascades toward the grid scale and thus to ensure the stability of the model while not interfering with the resolved mesoscale activity" (Madec and the NEMO team, 2008).
The strengths and weaknesses of different mixing parametrizations have been discussed in detail (e.g., Danabasoglu and McWilliams, 1995; Griffies et al., 1998; Olbers et al., 2012). However, in all cases the specification of the lateral eddy coefficients remains the problematic point. One example of the representation of eddies in models with different resolution and the different mixing parametrizations used for the respective simulations is given by Marsh et al. (2009).

In general, three types of ocean models can be distinguished when it comes to their ability to represent eddies: (i) coarse resolution models, that do not represent eddies at all (horizontal resolution $\mathcal{O}\,(> 1/2°)$), (ii) eddy-permitting high resolution models (horizontal resolution $\mathcal{O}\,(< 1/2°)$), and (iii) eddy-resolving high resolution models (horizontal resolution $\mathcal{O}\,(< 1/10°)$). While the differentiation into three types makes sense intuitively, there is no clear definition of the resolution needed for a model to be called eddy-permitting or eddy-resolving, respectively.

Since the size of eddies in a respective region is determined by the Rossby radius of deformation, one way of looking at the capability of a model to resolve eddies is by checking the relation between horizontal mesh distance and the Rossby

radius. In this thesis, the models will be assumed to be eddy-resolving if the Rossby radius is represented by more than 2 grid points. Regions where the Rossby radius is resolved by 1-2 grid points will be regarded as eddy-permitting. In regions with less than 1 grid point per Rossby radius, the model is not able to resolve eddies at all. The two different model setups used in this thesis and their respective capability to resolve eddies will be discussed in chapter 2.3.

1.6 Objectives

The general aim of this thesis is to improve the understanding of the role that eddies play in the subpolar North Atlantic - especially in the Newfoundland Basin - by quantifying the temperature and freshwater fluxes by individual eddies across 47°N.

The Oceanography Department of the University of Bremen has installed a long-term observation system (North Atlantic Changes array, NOAC) along 47°N in the North Atlantic. The array consists of deep-sea moorings, inverted echo-sounders with pressure sensors (PIES) and annually repeated ship sections. Focus has been on the variability of the formation and spreading of deep water, as well as on the changes and variability of the NAC and its interaction with the western boundary current (e.g., Kieke et al., 2009; Rhein et al., 2011; Mertens et al., 2014; Roessler et al., 2015). One of the remaining open questions is to what extent eddies are responsible for the variability and mixing in the region and how the anomalies of temperature and freshwater carried by eddies contribute to the overall fluxes across 47°N.

This thesis will contribute to fill this gap and help to better understand the small scale dynamics that drive the variability in the region. My analyses are based on a combination of altimeter-derived velocity observations, satellite measurements of sea-surface temperature, hydrographic measurements as well as a new three dimensional temperature and salinity data set for the North Atlantic derived from satellite altimetry (Stendardo et al., 2016). First, only surface parameter of eddies and the respective surface fluxes are calculated using satellite measurements. In the second part of the thesis, the analysis is extended to volume fluxes using the three dimensional fields of temperature and salinity.

The analysis is also applied to output from two NEMO (Nucleus for European Modelling of the Ocean, Madec and the NEMO team, 2008) model simulations with different horizontal resolution: (1) *Arctic Northern Hemisphere Atlantic* configuration with 1/4° horizontal resolution (ANHA4) and (2) ANHA4 with a

nested 1/12° horizontal resolution encompassing the subpolar North Atlantic, called ANHA4-SPG12. The ANHA4 setup has the same horizontal resolution as the altimeter-derived velocity observations, and the ANHA4-SPG12 setup represents finer resolution allowing to assess the impact of different spatial resolution on the results.

The ANHA4 configuration has been used in the past for studying the circulation and deep convection in the Labrador Sea (Holdsworth and Myers, 2015) and the spreading of Greenland freshwater in the sub-Arctic seas (Dukhovskoy et al., 2016). This thesis gives an evaluation of how realistically eddies are represented in the model and will help to better understand the fluxes by eddies for future model studies. A paper that resulted from this thesis (Müller et al., 2017) is the first published analysis of the high-resolution nesting configuration (ANHA4-SPG12).

This thesis focuses on the following main questions:

- What is the spatial distribution of eddies in the southern subpolar North Atlantic? Are there regions where eddies occur predominantly?
- What are the properties of the detected eddies?
- How large are the temperature and freshwater fluxes carried by individual eddies?
- How well are the distribution of eddies, their properties, and the respective fluxes represented in the two model simulations with eddy-permitting and eddy-resolving resolution, respectively?
- Can the observation of surface signals help to understand deep signals below the surface?
- How well suited for the analysis of eddies is the new temperature and salinity data set derived from satellite altimetry using the Gravest Empirical Model (GEM) method?

The data used for the analysis, the numerical model and the method to detect eddies from satellite altimetry are introduced in Chapter 2. The surface properties of detected eddies and the related surface temperature fluxes are analyzed in chapter 3. In chapter 4 a new three dimensional product of temperature and salinity constructed from sea surface data is used to calculate volume fluxes of temperature and freshwater by eddies. The results are discussed and put into a broader context in chapter 5.

2 Data and Methods

2.1 Velocity Fields from Satellite Altimetry Data

To identify surface signatures of eddies, I used geostrophic velocity fields derived from a mapped sea level anomaly data set, specifically the "all-sat-merged" delayed time DT-MSLA product, version 15.0, provided by AVISO (`http://www.aviso.altimetry.fr/duacs/`). The sea level anomaly (SLA) observations stem from the SSALTO/Duacs multimission altimeter product (Le Traon et al., 1998; Ducet et al., 2000), a combined product from different satellite altimetry missions. Using the altimetry data from multiple platforms reduces the error of the SLA, while improving the spatial resolution (Le Traon et al., 2003). The considered SLA fields are mapped on a $1/4° \times 1/4°$ Mercator grid, have a daily resolution, and are available at the time of writing for the period January 1993 to April 2014. The daily resolution is a product of the processing of the data and cannot be achieved directly by satellite coverage. The corresponding near-real time product is available for a longer period and contains more recent data but is lower in quality than the delayed time data (SSALTO/Duacs, 2014). The sea level anomalies in the data set are calculated with respect to the 20 year mean for the years 1993 to 2012 (SSALTO/Duacs, 2014). Velocity anomalies (u,v) are then derived from each SLA map assuming geostrophic balance:

$$u = -\frac{g}{f}\frac{\partial SLA}{\partial y}, v = \frac{g}{f}\frac{\partial SLA}{\partial x}, \tag{2.1}$$

where g is the gravitational acceleration, f is the Coriolis parameter, and $\frac{\partial SLA}{\partial x}$ ($\frac{\partial SLA}{\partial y}$) is the gradient of the sea level anomaly in zonal (meridional) direction. For the purpose of eddy detection, only the intraseasonal changes of the velocity are of interest. The mean annual cycle was therefore removed from the velocity fields. For that I calculated the mean annual cycle for each velocity component at every grid point and subtracted it from the original velocity field. The analysis is focused on the region 60°W -10°W and 40°N - 55°N. For inferring the mean velocity field shown in Figure 2.1, the absolute geostrophic velocities from absolute

dynamic topography (DT-MADT, sum of SLA and mean dynamic topography) were used, since averaging over the SLA would result to zero.

2.2 Shipboard Velocity Observations

Satellite observations only reveal information from the ocean surface because they cannot penetrate deeper into the ocean. Since I want to relate the surface signal from eddies with the velocity field below, I used top to bottom profiles of current velocity from lowered Acoustic Doppler Current Profilers (LADCP) measurements. The data were obtained on 11 research cruises. These were carried out nominally along the 47°N section between 2003 and 2014 (Tab. 2.1).

Table 2.1: List of cruises carried out between 2003 and 2014 with LADCP stations along 47°N.

Ship and Cruise	Period of LADCP sections along 47°N	No. LADCP profiles	Longitudinal range of section
Meteor M59/2	16 - 26 Aug 2003	45	44°W - 13°W
Thalassa SUBPOLAR	4 Jun - 12 Jul 2005	30	43°W - 10°W
Maria S. Merian MSM5/1	28 - 30 Apr 2007	13	44°W - 41°W
Maria S. Merian MSM9/1	4 - 10 Aug 2008	27	44°W - 29°W
Maria S. Merian 12/3	30 Jul - 5 Aug 2009	26	47°W - 31°W
Meteor M82/2	6 - 28 Aug 2010	45	47°W - 15°W
Meteor M85/1	25 Jun - 16 Jul 2011	44	47°W - 11°W
Maria S. Merian MSM21/2	8 - 14 Jul 2012	31	47°W - 31°W
Maria S. Merian MSM27	20 - 22 Apr 2013	16	47°W - 43°W
Maria S. Merian MSM28	29 May - 14 Jun 2013	39	44°W - 11°W
Maria S. Merian MSM38	19 - 28 May 2014	51	47°W - 29°W

All 11 sections included the western basin and the continental slope, while only 5 of them (2003, 2005, 2010, 2011, 2013) extended all the way to the eastern basin. In the western basin the cruise tracks typically start at Flemish Pass and nominally follow 47°N. In the eastern part of the section, the tracks deviate from the 47°N section and are inclined northward towards the shelf where they end around Goban Spur (Figure 2.1). The shelf regions on either side of the Atlantic are not covered by LADCP data. All cruises and the extent of the respective velocity sections along 47°N are summarized in Tab. 2.1. Most of the cruises were carried out as part of the BMBF (German Federal Ministry or Education and Research) funded RACE (Regional Atlantic Circulation and Global Change) program and its predecessors ("North Atlantic" and SFB460).

Measurements were taken with two LADCP-devices of the type Teledyne RDI 300 kHz Workhorse Monitor. The instruments were operated in a synchronized mode with a ping rate of 1 Hz and a vertical bin size of 10 m. The processing of

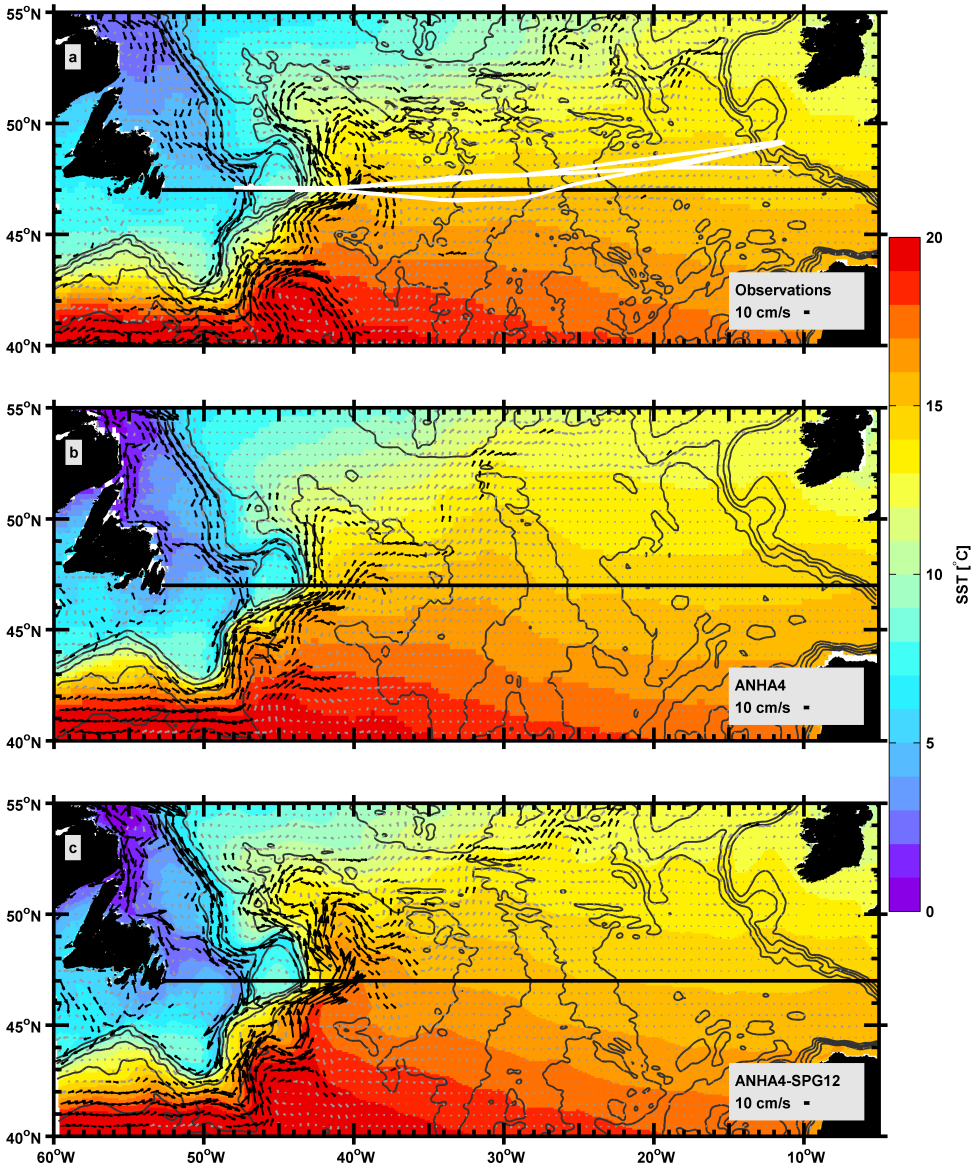

Figure 2.1: Mean geostrophic velocities and mean SST in the study region for the period January 2002 to December 2013. Mean AVISO geostrophic velocities from absolute dynamic topography (DT-MADT) and mean NOAA Optimum Interpolation SST V2 are shown for the observations (a). For the model simulations (1/4°ANHA4 simulation (b) and 1/12°ANHA4-SPG12 simulation (c)), the mean geostrophic velocities and mean SST from the respective model runs are shown. Mean velocities exceeding 10 cm s^{-1} are indicated with black arrows. Only every second velocity vector is plotted for the observations and the ANHA4 simulation and every sixth vector for the ANHA4-SPG12 simulation. The white lines in panel (a) indicate the tracks of the 11 cruises conducted along nominally 47°N between 2003 and 2014. The black line indicates the section at 47°N. Isobaths are given every 1000 m using bathymetry derived from the ETOPO1 data set (Amante and Eakins, 2009) for the observations and the respective model bathymetry of the model simulations. The bathymetries in the panels (a) and (c) are lowpass-filtered to highlight general features.

the raw data follows Visbeck (2002). All LADCP profiles were detided using the TPXO7.2 tidal model (Egbert and Erofeeva, 2002) and then linearly interpolated onto a regular grid with a horizontal resolution varying between 4 km at the western continental slope (west of 43°W), 8 km between 43°W and 42°W (and east of 15°W) and 15 km in the interior ocean. The vertical resolution is 10 m. Data from the western basin west of 36°W prior to 2012 has already been used by Mertens et al. (2014) to calculate the NAC transport, WBC transport, and the strength of the recirculation in the Newfoundland Basin (NBR).

2.3 ANHA4 and ANHA4-SPG12 Configurations of the NEMO Model

The model simulations analyzed in this thesis were carried out by the Numerical Modeling Group at the University of Alberta (Xianmin Hu, Clark Pennelly) using the *Nucleus for European Modeling of the Ocean* (NEMO) model numerical framework version 3.4 (Madec and the NEMO team, 2008). The model consists of an ocean component including the 3D, linear free surface, hydrostatic, primitive-equations, which is coupled to the *Louvain-la-Neuve sea-ice model* (LIM2) (Fichefet and Maqueda, 1997). The ocean model has 50 vertical levels in z-coordinates with 1 m thickness for the top layer and decreasing vertical resolution with depth. The layer thickness increases to ∼100 m at around 600 m depth, ∼200 m at around 1500 m depth, ∼300 m at around 2500 m depth and a maximum thickness of ∼450 m for the lowest layer. The distribution of variables is a three-dimensional Arakawa C grid (Arakawa and Lamb, 1977). Following Madec and the NEMO team (2008) several assumptions are made in order to formulate these equations:

1. Spherical Earth (geopotential surfaces are spheres, i.e. gravity is always vertical)
2. Thin shell, i.e. ocean depth (H_{Ocean}) << Earth's radius (R_{Earth})
3. Turbulent closure approximation (turbulent fluxes, representing small scale motion, are parametrized in terms of large-scale features)
4. Boussinesq approximation (density variations are neglected except for their contribution to the buoyancy force)
5. Hydrostatic approximation (balance between vertical pressure gradient and gravitational force)

6. Incompressibility approximation (water is assumed to be incompressible, i.e. $\nabla \cdot \mathbf{U} = 0$)

The equations of the model are described in detail by Madec and the NEMO team (2008). They are formulated so that the unit vectors $(\mathbf{i}, \mathbf{j}, \mathbf{k})$ are linked to the Earth's geometry. The vertical vector $\mathbf{k}$ is directed upward (aligned with gravity) and the horizontal vectors $(\mathbf{i}, \mathbf{j})$ are tangential to the geopotential surfaces. The main variables for the primitive equations are: velocity vector: $\mathbf{U} = \mathbf{U_h} + w\mathbf{k}$, where U_h is the horizontal velocity vector (i.e. $u\mathbf{i} + v\mathbf{j}$), potential temperature T, salinity S, and in situ density ρ. This leads to the following set of equations (momentum balance, hydrostatic equilibrium, incompressibility equation, temperature and salt conservation equations, and equation of state):

$$\frac{\partial \mathbf{U_h}}{\partial t} = -\left[(\nabla \times \mathbf{U}) \times \mathbf{U} + \frac{1}{2}\nabla\left(\mathbf{U}^2\right)\right]_h - f\mathbf{k} \times \mathbf{U}_h - \frac{1}{\rho_0}\nabla_h p + \mathbf{D^U} + \mathbf{F^U}$$

$$\frac{\partial p}{\partial z} = -\rho\, g$$

$$\nabla \cdot \mathbf{U} = 0$$

$$\frac{\partial T}{\partial t} = -\nabla \cdot (T\ \mathbf{U}) + D^T + F^T$$

$$\frac{\partial S}{\partial t} = -\nabla \cdot (S\ \mathbf{U}) + D^S + F^S$$

$$\rho = \rho\,(T, S, p)$$

where ∇ is the derivative vector operator in $(\mathbf{i}, \mathbf{j}, \mathbf{k})$ directions, t is the time, z is the vertical coordinate, ρ_0 is the reference density, p is the pressure, $f = 2\mathbf{\Omega} \cdot \mathbf{k}$ is the Coriolis parameter (with Ω as Earth's angular velocity vector), and g is the gravitational acceleration. $\mathbf{D^U}$, D^T and D^S are the parameterizations of small-scale physics for momentum, temperature and salinity, and $\mathbf{F^U}$, F^T and F^S are the surface forcing terms (Madec and the NEMO team, 2008).

The sea ice module has an elastic-viscous-plastic (EVP) ice rheology (Hunke and Dukowicz, 1997) with no-slip lateral boundary conditions for the sea ice and free-slip lateral boundary conditions for the ocean. This and the main components of the model are summarized in Figure 2.2.

Two different model configurations have been considered for this work. The *Arctic Northern Hemisphere Atlantic* configuration with 1/4° horizontal resolution (ANHA4) is a sub-domain of the global tripolar ORCA025 configuration (Bernard et al., 2006). The three poles are located on land over Russia, northern Canada and Antarctica. This allows for high spatial resolution in high latitudes

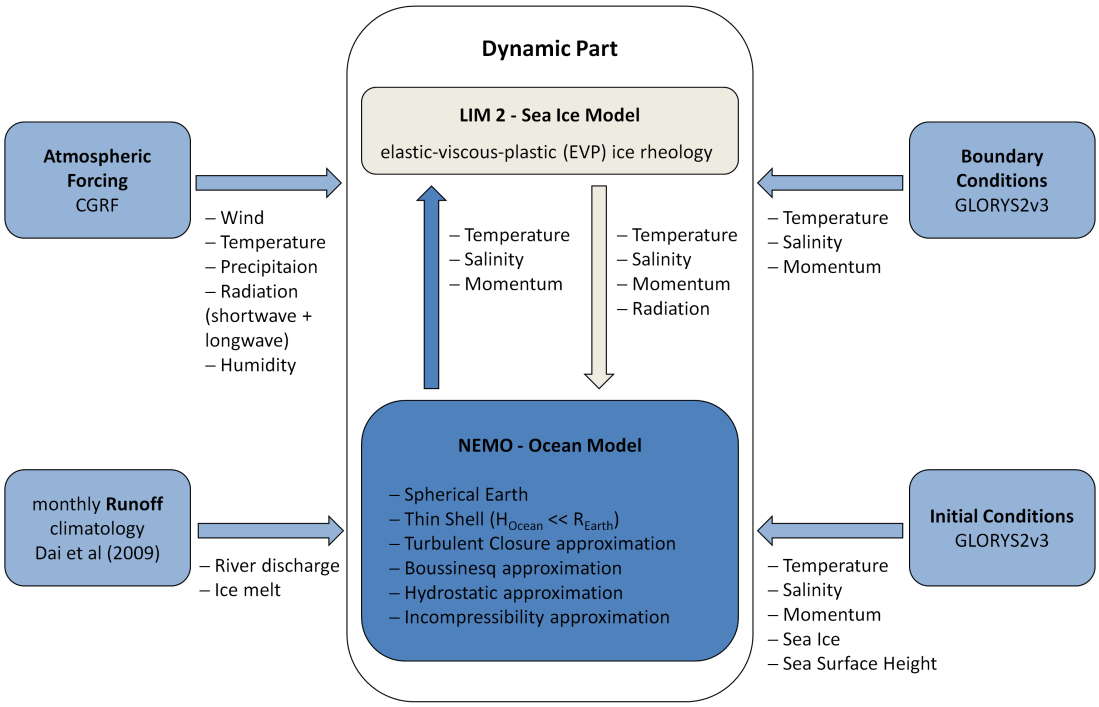

Figure 2.2: Schematic of the main components of the ANHA configuration.

while at the same time avoiding a grid singularity in the Arctic Ocean. A map of the model domain with the respective horizontal grid resolution is shown in Figure 2.3a. This regional configuration has been used in the past for studying the circulation and deep convection in the Labrador Sea (Holdsworth and Myers, 2015) and the spreading of Greenland freshwater in the sub-Arctic seas (Dukhovskoy et al., 2016). The model domain of this configuration covers the whole North Atlantic and the Nordic Sea (including the Gulf of Mexico in the west and the Mediterranean Sea in the east) with open boundaries at 20°S and the Bering Strait. The open boundary conditions are provided from the *Global Ocean Reanalyses and Simulations* (GLORYS2v3) reanalysis from MERCATOR (Ferry et al., 2010). The initial conditions for the model simulation stem from the same reanalysis product.

The model is forced with atmospheric data from the *Canadian Meteorological Centre's Global Deterministic Prediction System* (CGRF) (Smith et al., 2014), with 1 hour temporal resolution, and a horizontal resolution of 0.45° longitude and 0.3° latitude. Runoff forcing is obtained from the monthly runoff climatology by Dai et al. (2009), manually remapped to the model grid to preserve runoff and watershed volumes (X. Hu, University of Alberta, personal communication,

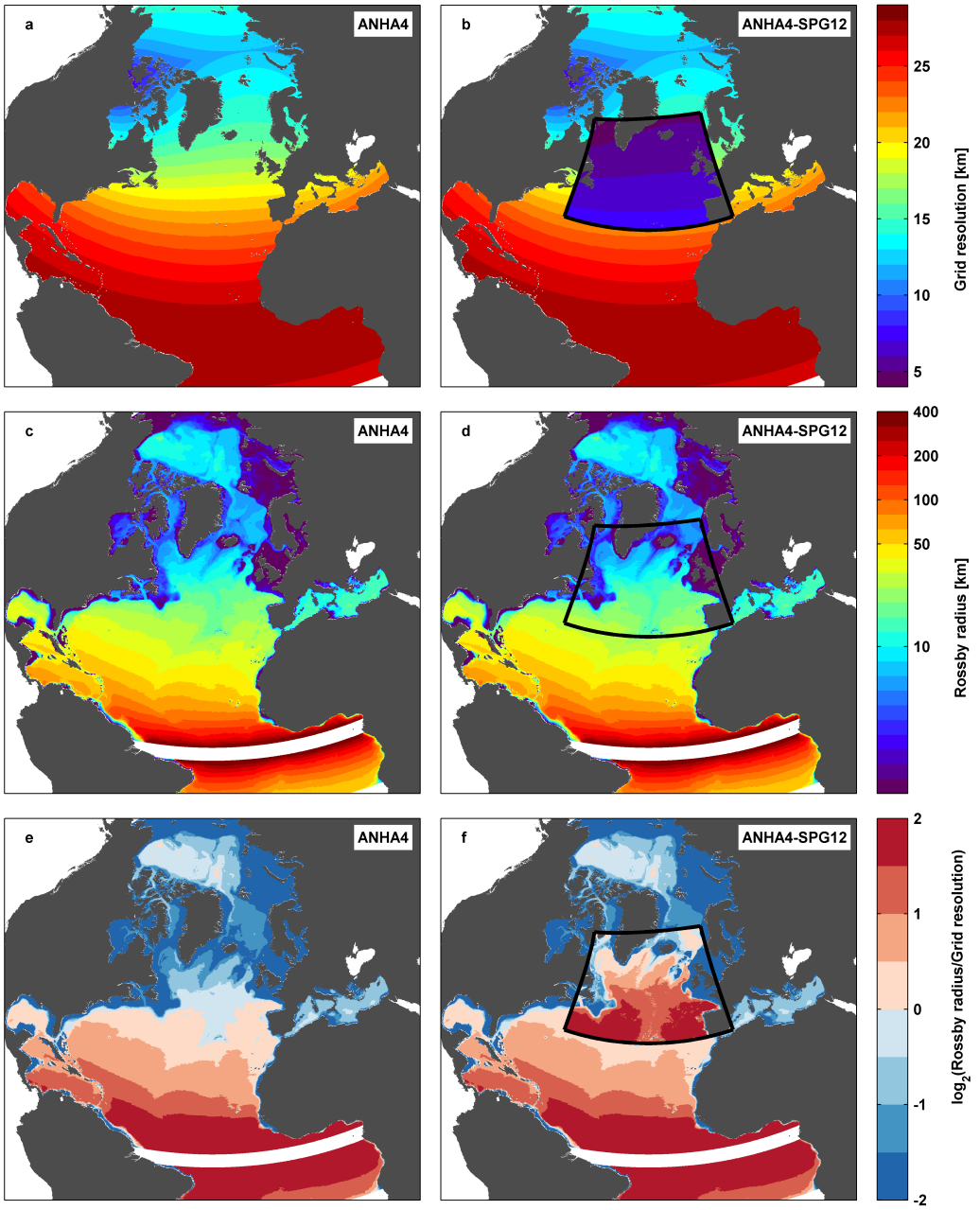

Figure 2.3: Horizontal grid resolution (average of X- and Y-direction) of the ANHA4 model domain (a) and the two-way nested ANHA4-SPG12 sub-domain in the subpolar gyre region (b). The respective Rossby radius of the two configurations (c, d) and the Rossby radius relative to the mesh resolution in log 2 (e, f). The model is eddy-resolving for values above 1 (dark red), eddy-permitting for values between 0 and 1 (light red); it does not resolve eddies for values below 0 (blue).

2015). The time-step of the ANHA4 configuration is 1080 s, and the output is saved every 5 days for the period January 2002 to December 2013.

The second model configuration (ANHA4-SPG12) consists of a sub-region with 1/12° horizontal resolution. The sub-region with high resolution is two-way nested in the ANHA4 configuration using the *Adaptive Grid Refinement In Fortran* (AGRIF) tool (Debreu et al., 2008). The inner high resolution nest covers the subpolar gyre region between 36°N and 70°N, with a zonal extent from 60°W south of Newfoundland and around 70°W in the northern Labrador Sea to 0°W (Figure 2.3b). Apart from resolution-dependent parameters (e.g. the model time-step, horizontal and vertical viscosity) all parameters as well as the vertical resolution are kept identical to the ANHA4 configuration. The time-step for the ANHA4-SPG12 simulation is 180 s, and the output is also saved every 5 days for the period January 2002 to December 2013. The time-step here is so much shorter than in the ANHA4 configuration because higher spatial resolution requires higher temporal resolution in order to keep numerical stability. According to the CFL-Criterion (named after mathematicians Richard Courant, Kurt Friedrichs, and Hans Lewy; Courant et al., 1928), the ratio of horizontal grid size (Δx) and time-step (Δt) always has to be smaller than the velocity u. Physically this means that an advective flux or a wave cannot always remain in neighboring grid cells during one time step and does not "skip" one grid cell.

Vertical mixing at sub-grid scales in both configurations is parameterized using a turbulent kinetic energy (TKE) closure model (Madec and the NEMO team, 2008). For lateral mixing the model uses a bi-Laplacian operator with an eddy viscosity of 1.5×10^{11} m^4/s^2 for the ANHA4 configuration and 1.0×10^{10} m^4/s^2 for the ANHA4-SPG12 configuration. Subgridscale tracer lateral diffusion is parameterized with an isopycnal Laplacian operator with a horizontal eddy diffusivity of 300 m^2/s for the ANAH4 configuration and 50 m^2/s for the ANHA4-SPG12 configuration.

No relaxation is applied to the model salinity during either of the simulations, meaning there is a drift away from the initial state towards higher salinity in the North Atlantic. For the first 7 years of the respective model simulations, the drift in the study region (10°W - 60°W and 40°N - 55°N) is between 0.07/year and 0.08/year, while it is slightly negative for the later years (between -0.03/year and -0.04/year).

My study region (40°N - 55°N) is located in the center of the model domain, so no spurious effects from the boundaries of the nesting region (ANHA4-SPG12) or from the open boundary conditions of the ANHA4 domain are expected. The sea level anomalies of the respective model simulations are linearly interpolated from the curvilinear model grid to a regular longitude/latitude grid. The geostrophic

velocities were then calculated exactly the same way as the velocities from the altimeter-derived observations using Eq. 2.1.

While the mean circulation is generally weaker and smoother in the ANHA4 simulation than in the observations and the ANHA4-SPG12 simulation, the patterns of the mean circulation in both model simulations correspond well to the observed mean absolute geostrophic velocities detected from satellite altimetry (Figure 2.1). In both simulations as in the observations, there are clearly defined northward and southward boundary currents, the Mann-Eddy, several recirculation cells in the Newfoundland Basin, as well as the Northwest Corner and the pathway over the fracture zones of the MAR. Only the coastal branch of the Labrador Current is more pronounced in the models than in the observations.

Assuming that at least two model grid points per Rossby radius are needed to resolve eddies, the 1/4° ANHA4 configuration is eddy-resolving only in the tropics up to around 20°N and eddy-permitting until roughly 45°N. In the subpolar gyre, the Labrador Sea, and the Northern Ocean, the horizontal resolution is too coarse to allow for a realistic representation of eddies in the model (Figure 2.3e). The 1/12° ANHA4-SPG12 nesting region is eddy-resolving up to around 50°N and eddy-permitting north of there (Figure 2.3f). For both configurations, the Rossby radius in the shallow shelf region of the Grand Banks of Newfoundland is too small to be resolved by the model ($\sim$ 5 km, Figure 2.3c/d).

2.4 Eddy Detection Method

Assessing the role of eddies for the temperature flux across 47°N requires an adequate automatic eddy detection technique. Automatic detection and tracking of eddies in the ocean has been (and still is) far from being a trivial task, and there are many studies making use of different methods of eddy detection. This was done for example by analyzing the Okubo-Weiss parameter (the ratio between strain/shear and relative vorticity, Okubo, 1970; Weiss, 1991; Isern-Fontanet et al., 2003; Chelton et al., 2007, 2011), by wavelet analysis of the relative vorticity (e.g., Doglioli et al., 2007), closed contours of SLA (e.g., Faghmous et al., 2015), or by direct analysis of the flow geometry (e.g., Nencioli et al., 2010). None of these detection methods is perfect, and every method has its strengths and weaknesses. A comparison of different algorithms, including the one used in this thesis, has been done for example by Escudier et al. (2016). While they showed that different algorithms give different results for the shapes and locations of eddies, none of the methods stands out as superior to the others.

For the study region in the North Atlantic, I choose the vector geometry-based algorithm following Nencioli et al. (2010) for both the observations and the model simulations. It is based directly on the velocity field and searches for regions where the velocity rotates around a center. This approach should be well suited for a region that is not only characterized by eddies but also by meanders and other small scale features that other methods might falsely detect as eddies. A full description and evaluation of the algorithm is given by Nencioli et al. (2010), but the major steps are summarized below. The algorithm consists of three steps: (1) Detecting eddy centers, (2) identifying the eddy boundary, and (3) tracking the eddy.

Step 1: For the detection of possible eddy centers, every snapshot of the velocity field (daily for the observations, 5-day for the model simulations) is analyzed using four constraints:

1. The meridional velocity v has to reverse sign and increase radially with distance from the center along a zonal section with the distance of "a" grid points around the potential eddy center.

2. For the points matching constraint (1), also the zonal velocity u has to reverse sign and increase radially within a meridional section of the same length "a" around the center. The sense of rotation for u has to be the same as for v (i.e. forming a circular pattern around the potential eddy center).

3. The potential eddy center has to be the local minimum of velocity within a box with edge length of "b" grid points around the center.

4. In order to avoid false identification of meanders and divergent zones as eddies, the velocity vectors have to rotate gradually in the same direction within a box of "$a-1$" grid points around the potential center of the eddy. This makes the algorithm ideal for the study region, which is characterized not only by eddies but also by strong meandering of the NAC.

Points on the grid that satisfy all four constraints are then defined as eddy centers (Figure 2.4). The algorithm requires the parameters a and b to be chosen with respect to the horizontal resolution of the velocity field. Liu et al. (2012) found the ideal set of parameters for the AVISO velocity field to be $a = 3$ grid points, and $b = 2$ grid points. These values are used here as well. Following Liu et al. (2012), the velocity fields from the observations and the ANHA4 simulation are linearly interpolated from $1/4° \times 1/4°$ to $1/6° \times 1/6°$ resolution before applying the algorithm. This does not change any features in the velocity field while

improving the algorithm's performance. For the ANHA4-SPG12 simulation with $1/12° \times 1/12°$ horizontal resolution I found a=5 grid points and b=3 grid points to be the setting with the highest detection rate. This was tested by repeatedly running the algorithm with different sets of parameters for a subregion in the NAC that includes eddies as well as meanders and comparing the success of eddy detection by visual inspection.

Step 2: The velocity field around each detected eddy center is integrated and the local streamfunction calculated. The streamfunction ψ is defined so that $u = \frac{\partial \psi}{\partial y}$ and $v = -\frac{\partial \psi}{\partial x}$. Following Nencioli et al. (2010), the eddy boundary is then defined as the largest closed contour of the local streamfunction around the eddy center. The eddy radius (R_E) is defined as the mean distance of all grid points of the eddy boundary to the eddy center. The analysis excludes very small features by not taking into account any eddies with a radius smaller than $R_{min} = 20 \times cos(\phi)$ km, where ϕ is the latitude of the eddy center (i.e. eddies with a radius that is only represented by one grid cell of the interpolated grid or two grid cells of the ANHA4-SPG12 grid are not taken into account).

Step 3: Last, the detected eddies are tracked through time to determine the eddies' trajectories. The eddy tracking method used here is in principal very similar to most automated eddy tracking procedures (e.g., Isern-Fontanet et al., 2003; Doglioli et al., 2007; Chelton et al., 2007, 2011; Chaigneau et al., 2008). An eddy track between successive time steps is defined when an eddy of the same rotation (cyclone/anticyclone) can be found at time step t_{n+1} within a defined search radius around the initial centers position at time step t_n. In case no successive eddy can be detected at t_{n+1}, the next time step t_{n+2} is analyzed. If no continuous eddy track can be found for two successive time steps, the eddy is regarded as dissolved.

The reliability of eddy tracking depends on the definition of the search radius. This in turn depends on the temporal and spatial resolution of the data, as well as on the phase speed of long baroclinic Rossby waves at the location of the respective eddy (Chelton et al., 2007, 2011). Since the eddy translation speed is not known a priori of running the algorithm, the typical phase speed of baroclinic Rossby waves in the study region (20 cm s^{-1}, (Chelton et al., 1998)) is used. Following Chelton et al. (2011), the search radius should be 1.75 times the distance that a long baroclinic Rossby wave would propagate. This leads to a search radius of 30 km for the observations with daily resolution. Using the same assumption in the 5 day resolution of the model output would suggest a search radius of about 150 km. In practice, 150 km led in almost all cases to ambiguous

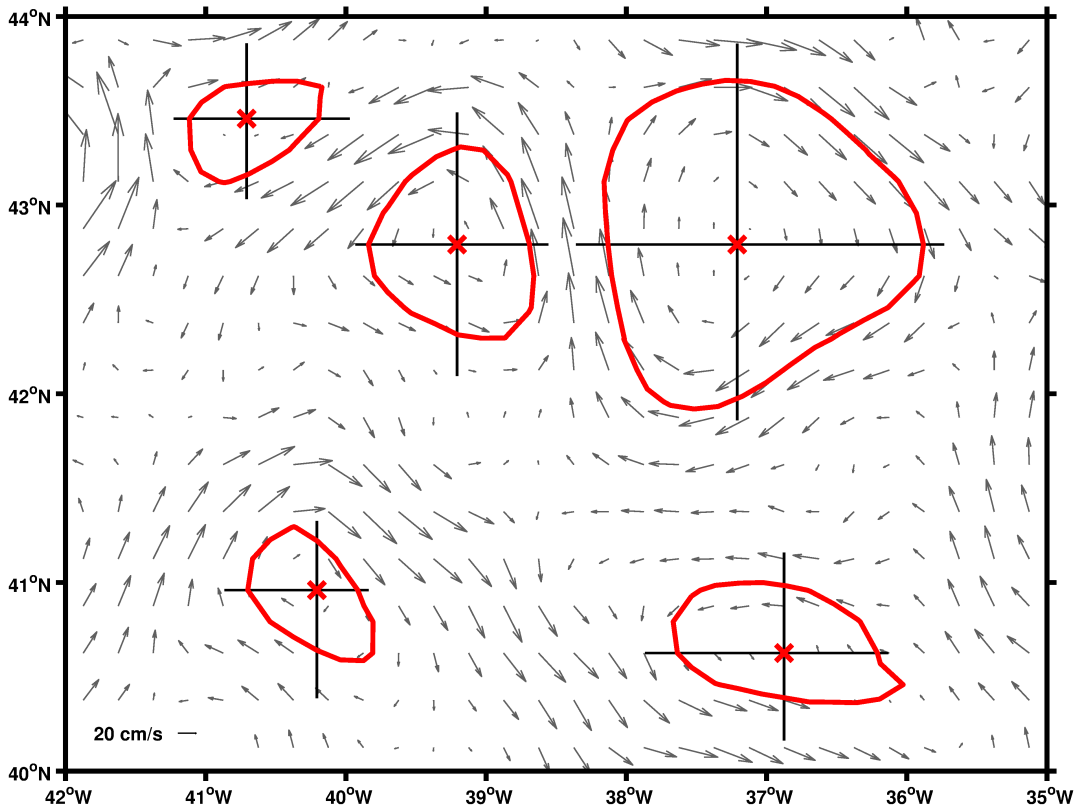

Figure 2.4: Example of eddies detected from a snapshot of geostrophic velocities (June 1, 1993, arrows) using the vector geometry-based algorithm following Nencioli et al. (2010). Eddy centers ($\mathbf{x}$) are detected using the four constrains described in step 1. The zonal and meridional lines through the respective eddy centers, indicate the lines along which the meridional and zonal velocities have to change sign (constrains 1 and 2). The outer shape is calculated from the local streamfunction around eddy centers (step 2).

eddy tracks, and therefore a smaller search radius of only 40 km was chosen as the most appropriate for the model simulations.

In order to improve the eddy tracking, the detected tracks are post-processed as suggested by Faghmous et al. (2015), by merging terminated trajectories with new trajectories starting in the neighborhood of the termination point. Nevertheless, some splitting of eddy tracks (in observations and model) cannot be avoided. After the post-processing step, very short lived eddies with a life time of less than 7 days are removed and not considered for further analysis. For the model simulations this means that an eddy has to exist for at least two steps of the saved output (i.e. 10 days). The eddy translation speed is then calculated simply as the distance of displacement of the eddy center between two snapshots divided by the time between the snapshots.

As the outer shape of the eddies is defined on a discrete grid, the eddy radius R_E may fluctuate between two grid cells and therefore may change by the distance between two grid cells between two time-steps. In order to avoid these fluctuations that result solely from the discrete grid, the eddy radii R_E and areas A are filtered with a 7 day moving average ($\pm$ 3 days) along the respective eddy trajectories. For the two model simulations, a 10 day moving average is used ($\pm$ 5 days, i.e. $\pm$ 1 output time-step).

3 Surface Properties and Surface Temperature Fluxes related to Eddies

3.1 Calculation of Surface Temperature Fluxes Related to Eddies

I seek to combine the results from the eddy detection with sea surface temperature (SST) data in order to investigate the surface temperature flux associated with the eddies' movements across 47°N. While T/S profiles from the international Argo program and ship-based observations may provide insight into the vertical structure of eddies and add salinity measurements, the available data from the deep ocean is still scarce in space and time compared to surface-limited satellite observations.

The first part of the observational analysis therefore focuses on surface temperature fluxes that can be measured on large scale from satellites. Surface freshwater fluxes are omitted because no suitable satellite measurements are available. Sea surface salinity (SSS) observations from satellites ("Soil Moisture and Ocean Salinity, SMOS" (e.g., Font et al., 2004) operated since 2009, and "Aquarius/SAC-D" (e.g., Melnichenko et al., 2016) in operation during 2011-2015) are only available for a short period of time, and the accuracy of SSS observations in the subpolar North Atlantic is not yet sufficient for quantitative studies (Köhler et al., 2015).

I use daily data from the NOAA 1/4°×1/4° Optimum Interpolation Sea Surface Temperature version 2 (OISST V2) analysis (Reynolds et al., 2007) and combine it with the eddy shapes detected in the daily AVISO geostrophic velocity fields. The SST data set is based on satellite observations with the Advanced Very High Resolution Radiometer (AVHRR) and corrected with in situ measurements from

ships and buoys. The surface temperature flux carried by individual eddies ($\mathbf{Q}$ [W m^{-1}], with 1 GW m^{-1} = 10^9 W m^{-1}) is calculated as follows:

$$\mathbf{Q} = \mathbf{u}_E \; 2R_E \; \rho_0 \; c_{p_0} \; \overline{SST'} \tag{3.1}$$

where $\mathbf{u}_E$ is the eddy's translation velocity, R_E is the radius of the individual eddy, ρ_0 = 1025 kg m^{-3} an average sea water density, c_{p_0} = 4200 J kg^{-1} K^{-1} an average specific heat capacity for sea water, and $\overline{SST'}$ is the average of all SST anomaly grid points within the area ($A = \pi R_E^2$) of the eddy. The daily SST anomaly at each grid point is calculated with respect to the mean annual cycle at the respective grid point. This is done to remove the dominant seasonal signal, since I am only interested in the influence of the eddy on the temperature anomaly and not in the mean seasonal cycle of the SST at the respective point. Calculating the anomaly with respect to the surrounding water yields somewhat different numbers for individual eddies but does not change the overall results. Unlike the velocity field, the SST is not interpolated to 1/6° × 1/6° resolution, as this was done for the velocities only to improve the performance of the eddy detection algorithm. The surface temperature flux calculated here can be seen as a surface heat flux relative to a varying reference temperature (i.e. the mean seasonal cycle of the temperature).

For the model simulations, the SST field from the respective model run is used instead of the OISST, but the calculation of the surface temperature flux for eddies detected in the model is exactly the same as for the observations. The structures of the mean SST fields of both model simulations are very similar to the mean SST field derived from observations, clearly showing the cold subpolar gyre and the warm subtropical gyre (Figure 2.1). However, both model simulations show warmer temperatures north-west of the Northwest Corner when compared to the observations, and the SST field in the ANHA4 simulation is smoother than the observations (Figure 2.1b).

3.2 Spatial Distribution of Eddies Detected in the Altimeter Data

To investigate whether or not EKE in the study region is mainly caused by individual eddies, the spatial distribution of eddies is related to the spatial distribution of EKE in the area averaged over the period of interest (Figure 3.1a). The EKE is computed as $\frac{1}{2}(u'^2 + v'^2)$, where primes denote deviations from the mean

annual cycle, so that it includes all intraseasonal components of the kinetic energy. The highest levels of EKE in the study region are found along the pathway of the NAC all the way up to the Northwest Corner (Figure 3.1a). Local maxima of EKE (> 1000 cm^2 s^{-2}) are visible south of the Grand Banks of Newfoundland, around 44°N at the northern side of the Mann-Eddy, and around 47°N east of the Flemish Cap. The region of elevated EKE then widens and spreads towards the eastern basin following the pathway of the NAC over the fracture zones at the MAR. In contrast, the western side of the region is characterized by a strong EKE gradient across the continental slope of the Grand Banks of Newfoundland and low EKE in the order of 10-100 cm^2 s^{-2} on the shallow shelf.

In the satellite observation period January 1993 to April 2014 a total of 36997 eddies (∼1800/year) are found with a lifetime of more than 7 days and a radius larger than $R_{min} = 20 \times cos(\phi)$ km in the region between 60°W - 10°W and 40°N - 55°N. In order to assess the distribution of the detected eddies in the study region, the number of eddy centers in each $1° \times 1°$ box is counted. An eddy is counted once for a box no matter how long its center remained inside the respective box (Figure 3.1b). The eddy will be counted again when entering a different box, thus just summing up the numbers of all boxes will not result in the total number of eddies. The highest numbers of eddies are found in the western basin along the NAC pathway and on the Grand Banks of Newfoundland. Along the NAC pathway eddies follow roughly the 4000 m isobath along the Grand Banks with regional maxima of 8-10 eddies per year north of the Mann-Eddy and east of the Flemish Cap. The band of abundant eddies then continues towards the Northwest Corner with around 6-8 eddies per year. The shelf break where the bathymetry is steepest shows fewer eddies than the surroundings while the shallow shelf region again shows numbers between 5-8 eddies per year. The trace of elevated numbers of eddies then follows the NAC eastward and forms a narrow band around 52°N close to the fracture zones of the Mid-Atlantic Ridge (MAR). The MAR region south of 50°N shows less eddy abundance with only 1-3 eddies per year. Higher numbers (5-8 eddies per year) are also observed along the shelf region in the eastern basin.

Only counting the boxes where eddies first appear results in a very similar pattern, even though the numbers are self-evidently lower. Most eddies are first detected along the boundary between NAC and WBC, in the region north-west of the Northwest Corner, on the Labrador shelf and the Grand Banks and along the eastern boundary of the basin (Figure 3.1c).

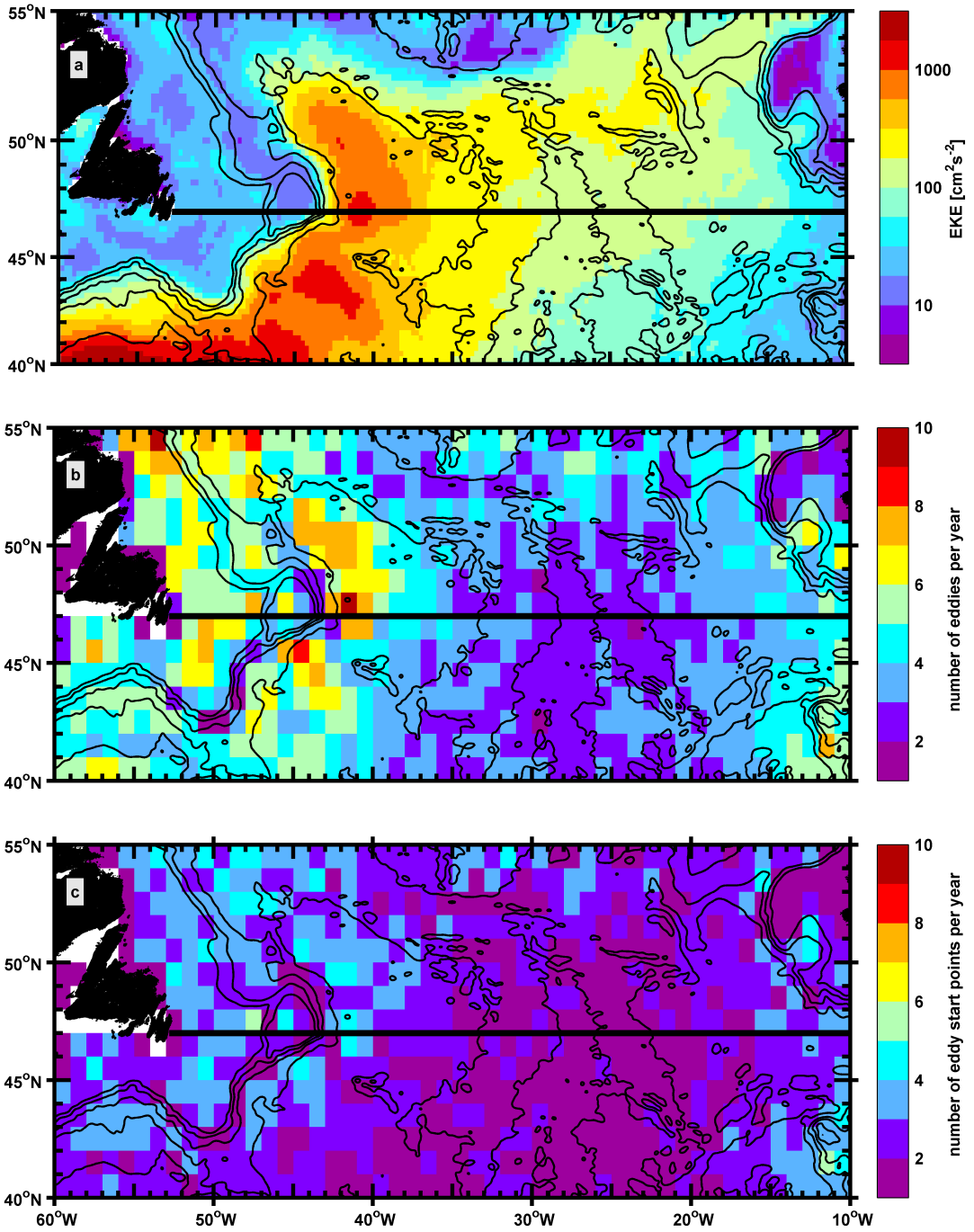

Figure 3.1: Mean eddy kinetic energy (EKE) derived from geostrophic velocity anomalies (a) compared to a map of the number of detected eddies per year (b) and the number of eddy start points per year (c) from January 1993 to April 2014 binned in $1° \times 1°$ boxes. Note that EKE [cm^2/s^2] is shown with a logarithmic scale. Isobaths are given every 1000 m using lowpass-filtered bathymetry derived from the ETOPO1 data set (Amante and Eakins, 2009).

Comparing the distribution of detected eddies with the average EKE in the area, I found that regions of eddy occurrences and regions of the highest EKE

do not necessarily coincide. While some local maxima of EKE indeed coincide with local maxima of eddy occurrence, many features in the EKE distribution cannot solely be explained by the presence of eddies. In fact, there are only few eddies in the regions where the highest EKE is found, especially south of the Grand Banks of Newfoundland between 40°N and 45°N. This suggests that the high EKE is caused by other processes (e.g. shifting of the mean NAC pathway, and meandering of the NAC) rather than by individual eddies.

Despite similar or even higher spatial resolution in the model simulations, fewer eddies are found (11397 in ANHA4 (∼950/year) and 14501 in ANHA4-SPG12, ∼1200/year) for the period January 2002 to December 2013 than in the observations for the same period (20267, ∼1700/year). The overall distribution is similar though, with the highest number of eddies along the pathway of the NAC. Only the shelf regions of the Grand Banks of Newfoundland show substantial differences where unlike in the observations, there are only very few eddies in both of the model simulations. Since the models are not able to resolve eddies in this region (Figure 2.3), this difference does not come as a surprise.

3.3 Comparison of Eddy Characteristics between Observations and Model

The following chapter focuses on the geometric and dynamic eddy characteristics (i.e. radius, lifetime, translation speed, and travel distance). These properties can be inferred from satellite observations and are a direct result of the vector geometry based algorithm. The average characteristics and their respective variability are analyzed within the study region between 60°W - 10°W and 40°N - 55°N for eddies detected from satellite altimetry as well as the model simulations. Since the distribution of properties is usually not Gaussian shaped (Figure 3.2), the respective variability is represented by the inner quartile range (i.e. the range of 50% of the values, shown in brackets), instead of using the standard deviation. The standard errors of the mean values within a 90% confidence interval (SEM) are calculated by bootstrapping the mean value with 1000 iterations. For the comparison of the observations with the two model simulations, the focus is on the model period ranging from January 2002 to December 2013. The mean value and the variability of all characteristics of the eddies from satellite observations remain essentially the same as for the full observation period January 1993 to April 2014. All eddy properties are listed in Tab. 3.1, and the respective probability density functions (PDFs) are shown in Figure 3.2.

Table 3.1: Characteristics of eddies detected in the region between 60°W - 10°W and 40°N - 55°N for observations and model experiments with different horizontal resolutions. Only eddies with a lifetime of more than 7 days and a radius > 20km$\times \cos(\phi)$ (where ϕ is the latitude) are taken into account. The variance of the values is represented by the inner quartile range (i.e. 50% of the values, shown in brackets). The standard error of the mean value within a 90% confidence interval (given in parentheses) was calculated from bootstrapping the mean value with 1000 iterations.

	Observations		**Model**	
			ANHA4	ANHA4-SPG12
period	Jan 1993 to Apr 2014	Jan 2002 to Dec 2013	Jan 2002 to Dec 2013	Jan 2002 to Dec 2013
total number of detected eddies	36997	20267	11397	14501
radius [km]	41.3 [32.3, 47.5] (0.02)	41.7 [32.6, 47.9] (0.03)	36.2 [27.0, 43.0] (0.06)	36.2 [28.4, 42.2] (0.05)
lifetime [days]	22.5 [10, 26] (0.2)	23.0 [10, 26] (0.2)	31.4 [20, 35] (0.3)	33.4 [20, 40] (0.3)
translation speed [cm s^{-1}]	4.1 [1.9, 5.7] (0.02)	4.1 [1.9, 5.7] (0.03)	2.0 [1.1, 2.8] (0.02)	2.6 [1.5, 3.6] (0.02)
travel distance [km]	73 [23, 95] (0.5)	74 [23, 95] (0.7)	58 [19, 80] (0.7)	80 [27, 108] (0.8)

The radius and lifetime of eddies in the two model simulations are essentially independent of the respective horizontal resolution of the model and do not differ substantially between the two model set-ups (Tab. 3.1). With around 36 km the average eddy radius in the models is somewhat smaller than in the observations (42 km), and the average eddy lifetime in the models (about one month) is one week longer than in the observations (23 days, Tab. 3.1). These differences are also clearly visible in the PDFs for radii and lifetimes (Figure 3.2a/b). Especially the distinct tail with high probabilities for long eddy lifetimes in the model simulations, compared to the peak of shorter lifetimes in the observations, is clearly recognizable.

The observed spatial distribution of eddy radii shows a similar pattern as the spatial variation of the first Rossby radius of deformation derived by Chelton et al. (1998). Both eddy and Rossby radius vary with latitude and water depth and the eddy radius is about 1.5-3 times the Rossby radius ($R_E = 0.7 \times R_{Rossby} + 27.7$). I find a correlation of 0.7 when comparing the local eddy radius with the local Rossby radius of deformation (both binned in $1° \times 1°$ boxes, Figure 3.3).

Contrary to eddy radii and lifetimes, estimates regarding the number of eddies detected in the region, the average translation speed, and the average travel distance do depend on the respective horizontal resolution of the model grid. The respective PDFs differ substantially between the two simulations (Figure 3.2c/d). There are more eddies in the higher resolved ANHA4-SPG12 than in

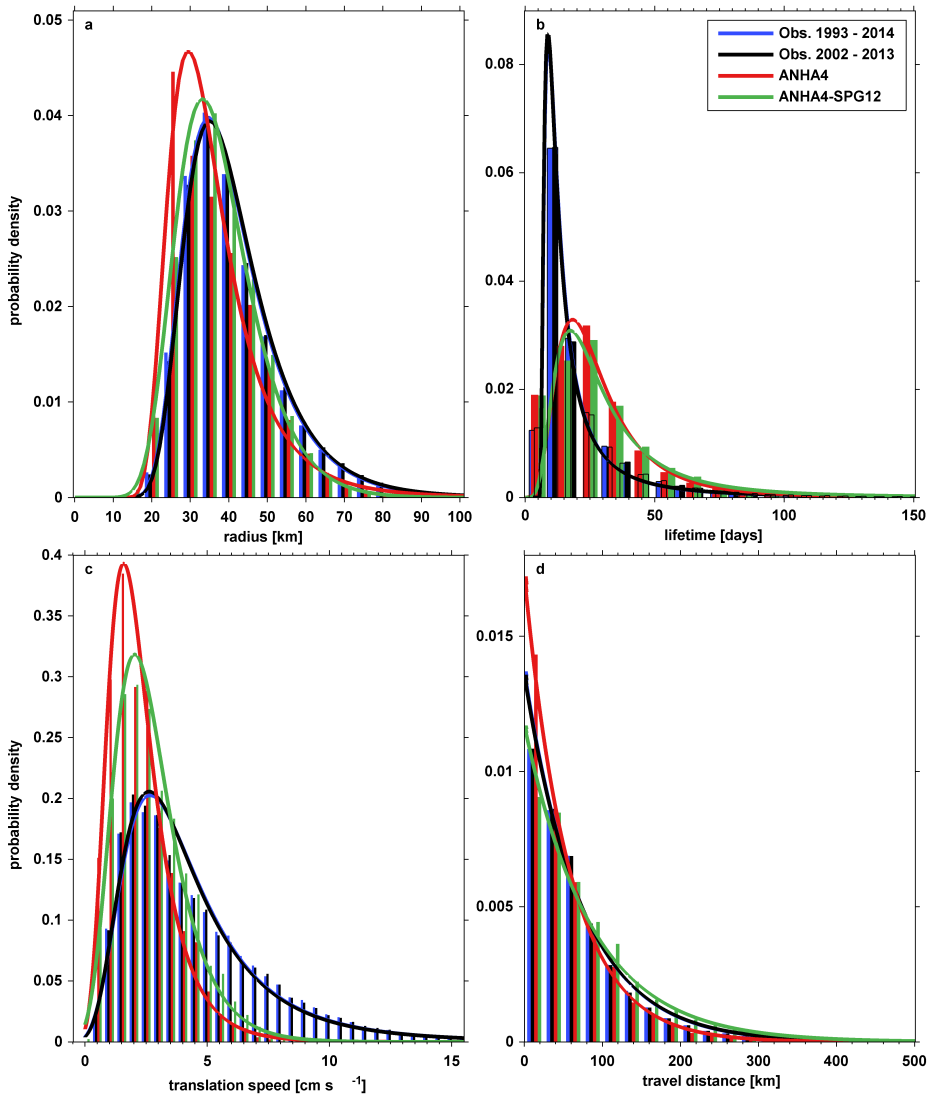

Figure 3.2: Probability density of characteristics associated with eddies detected between 60°W and 10°W and 40°N and 55°N in observations and two model simulations; (a) radius, (b) lifetime, (c) translation speed, and (d) travel distance. Only eddies with a lifetime of more than 7 days and a radius $> 20\text{km} \times \cos(\phi)$ (where ϕ is the latitude) are taken into account. Due to the different temporal resolution of the observations (daily) and the model runs (5 days), the bar plots of the lifetimes in panel (b) have different bins that overlap sometimes. For panels (a), (b), and (c) the probability distributions fitted to the histograms is a generalized extreme value distribution. The fit for the distribution of the travel distance in panel (d) is exponential.

ANHA4, they move faster (2.0 [1.1, 2.8] cm s^{-1} in ANHA4, and 2.6 [1.5, 3.6] cm s^{-1} in ANHA4-SPG12) and travel longer distances (58 [19, 80] km in ANHA4 and 80 [27, 108] km in ANHA4-SPG12). While the average travel distance of eddies in the models is in a similar range as that of the altimeter-derived eddies (73 [23, 95] km), the eddy translation speed in the models is only around 50-60%

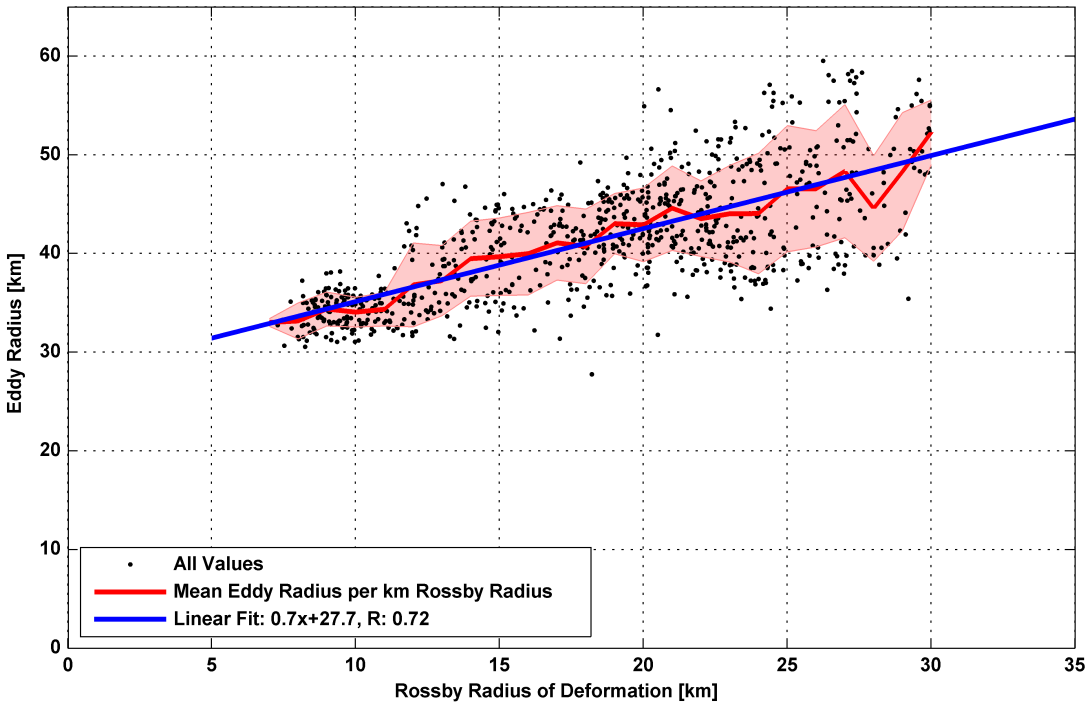

Figure 3.3: Correlation of the first baroclinic Rossby radius binned in 1° × 1° boxes (data from Chelton et al. (1998)) and the eddy radii binned in 1° × 1° boxes. All values between 60°W - 10°W and 40°N - 55°N are plotted in black dots, the average eddy radius per 1km Rossby radius is plotted in red (the shaded envelope represents one standard deviation). The linear fit through all points is shown in blue.

of the observed speed. The PDF for the translation speeds shows long tails for the observations compared to a rather sharp drop for the two model simulations (Figure 3.2c), likely caused by the different temporal resolutions (5 days in the model vs. daily for the observations).

The variability of the above mentioned properties (except the eddy radius) is always higher in the ANHA4-SPG12 simulation and decreases when the horizontal resolution of the model grid is coarser. Overall, the eddy characteristics in the higher resolution 1/12°ANHA4-SPG12 simulation are closer to those of the altimeter-derived eddies than the 1/4°ANHA4 simulation, even though the latter has the same resolution as the observations.

3.4 Surface Temperature Fluxes carried by Eddies across 47°N

The focus will now be on the surface temperature flux (**Q** as defined in equation 3.1) across the zonal section at 47°N. All eddies crossing the section between 53°W (Newfoundland) and 10°W are identified and the surface temperature fluxes of the eddies at the time of the crossing merged into a time series covering the period January 1993 to April 2014 for the observations and January 2002 to December 2013 for the two model simulations, respectively (Figure 3.4). Four different cases will be considered separately: (i) warm eddies moving northward, (ii) cold eddies moving southward, (iii) cold eddies moving northward, and (iv) warm eddies moving southward. Cases (i) and (ii) result in a positive (northward, Q_N) surface temperature flux, while cases (iii) and (iv) lead to a negative (southward, Q_S) surface temperature flux. As for the previous analysis, all numbers displayed here are given as a mean value, and the variability is represented by the inner quartile range. All numbers together with the SEM within a 90% confidence interval are listed in Tab. 3.2. The SEM was calculated by bootstrapping the mean value with 1000 iterations.

In the observations between January 1993 and April 2014, a total of 823 eddies with a lifetime of more than 7 days and radius larger than $R_{min} = 20 \times cos(\phi)$ were detected crossing 47°N (Figure 3.4a). The average travel distance of eddies after crossing 47°N is around 80 km, with about 1/3 of all eddies traveling further than 100 km and individual eddies traveling up to 300 km (Figure 3.5). Of the detected eddies, 51% move northward, and 49% move southward. Similarly, 52% (48%) have a positive (negative) surface temperature flux. Also the sense of rotation (52% anticyclones, 48% cyclones) and the type of SST anomaly (48% warm, 52% cold) are evenly distributed. Whilst there is no dominance of any type of eddy, there is a clear connection between the sense of rotation and the temperature anomaly carried by the eddy. The majority (58%) of anticyclones crossing 47°N are related to a warm SST anomaly, while the majority of cyclones (63%) have a cold SST anomaly.

The surface temperature flux across 47°N varies substantially between different eddies leading to a high temporal variability (Figure 3.4a and Tab. 3.2). However, there is no long term trend recognizable. Since northward and southward fluxes often cancel out each other, the net flux is small even though there are large fluxes in both direction. Here, the mean flux in either direction is around ±60

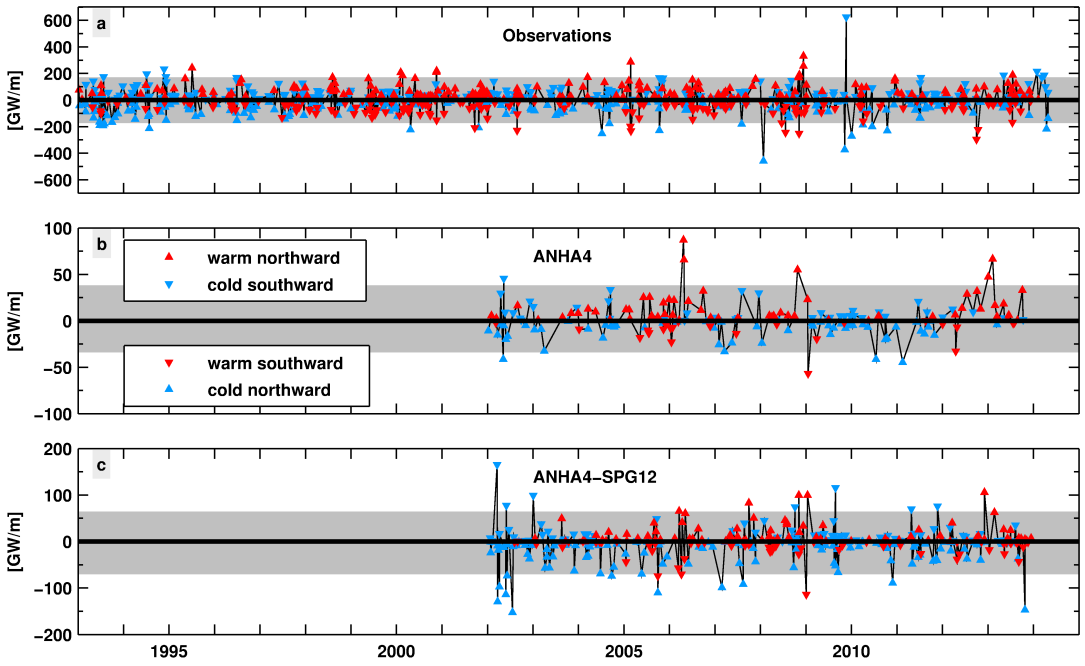

Figure 3.4: Time series of the meridional surface temperature flux by eddies across the zonal section at 47°N in the observations (a), 1/4°ANHA4 simulation (b) and 1/12°ANHA4-SPG12 simulation (c), 1 GW m^{-1} = 10^9 W m^{-1}. Red (blue) triangles indicate eddies with a warm (cold) SST anomaly. The direction of the triangle indicates the direction of meridional eddy movement across 47°N (northward/southward). A positive (northward) surface temperature flux can be achieved by northward moving warm eddies as well as southward moving cold eddies (and vice versa for a negative surface temperature flux, see text for details). The gray areas indicate two times the standard deviation of each time series. Note that the panels have different vertical scales.

GW m^{-1}, while averaging over all eddies results in a mean net flux $\overline{Q}$ that is effectively zero (0.5 [-46.8, 44.6] GW m^{-1}).

A substantial fraction of the surface temperature flux in either direction is achieved by eddies with an anomalously high flux. These so-called "strong eddies" are defined as all those eddies with a surface temperature flux that exceeds the mean flux plus two times the standard deviation in either direction ($\overline{Q} \pm 2 \times \sigma(Q)$, where the overbar denotes the mean, and σ is the standard deviation, Figure 3.4 gray area). All other eddies are defined as "regular eddies". In order to account for the extreme values while calculating the standard deviations, the calculation is repeated 10000 times with random subsamples of the time series, each with 1/3 of the length of the original time series, and then averaged.

Since the mean net flux is so small, it can be more practical to look at the absolute values of surface flux (i.e. without regard of the direction). The absolute surface temperature flux by eddies is calculated as the sum of the fluxes of

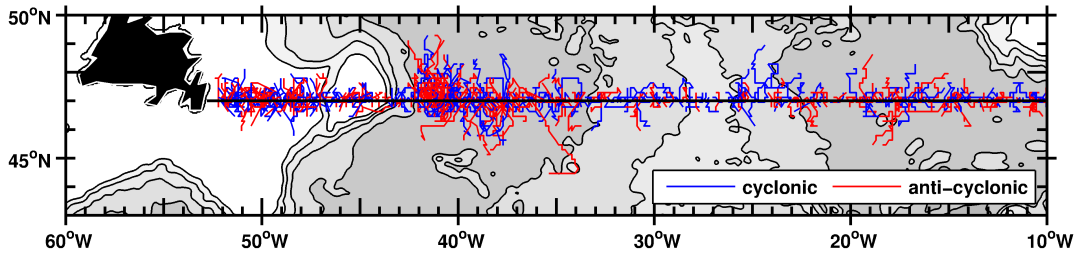

Figure 3.5: Trajectories of cyclonic (red) and anticyclonic (blue) eddies detected from satellite altimetry crossing 47°N between January 1993 and December 2014.

all eddies without regard for the direction of the flux, i.e. $\sum_i |Q_i|$. While this does not tell anything about the net effect of eddies, it gives us an idea about the overall strength of fluxes, their contribution to the variability, and the contribution of strong eddies to the total surface temperature flux by eddies (i.e. $\sum |Q_{strong}| \,/\, \sum |Q_{all}|$).

While only 46 out of 823 eddies are strong eddies (5.6% of all eddies), these strong eddies make up for 21% of the absolute surface temperature flux across 47°N (18% of the northward and 24% of the southward flux). This means that an average strong eddy ($\overline{|Q_{strong}|}$) accounts for 4-5 times of the surface temperature flux of regular eddies ($\overline{|Q_{regular}|}$).

As for the whole domain, there are fewer eddies crossing 47°N in the model simulations from January 2002 to December 2013 than in the observations for the same period (Figure 3.4b/c and Tab. 3.2). The mean surface temperature fluxes in either direction are substantially lower in both model simulations than in the observations (∼20% in ANHA4, ∼30% in ANHA4-SPG12; Tab. 3.2). The focus is therefore on the relative contribution of strong and regular eddies to the surface temperature flux since it is well represented in both model configurations.

Also the variability of the surface temperature fluxes relative to the respective mean is comparable between observations and models (Tab. 3.2). Considering only the model period from January 2002 to December 2013 for the satellite observations, 5.9% (26 out of 437) of the altimeter-derived eddies are strong eddies, and they account for 25% of the observed absolute surface temperature flux by eddies.

In the ANHA4 simulation 182 eddies are detected of which 10 (5.5%) are strong eddies. The mean flux in either direction is around 11-12 GW m^{-1} and the mean net flux across 47°N is 2.2 [-6.2, 8.2] GW m^{-1}. Strong eddies account for 25% of the absolute surface temperature flux by eddies, supporting the findings in the satellite observations.

Table 3.2: Number of eddies crossing 47°N and the respective surface temperature fluxes. The variance shown in brackets represents the inner quartile range (i.e. the range of 50% of the values). The uncertainty of radius, translation speed and SST anomaly are given as one standard deviation. The standard error of the mean value within a 90% confidence interval (given in parentheses) was calculated from bootstrapping the mean value with 1000 iterations. See text for the definition of strong eddies.

	Observations		**Model**	
			ANHA4	ANHA4-SPG12
period	Jan 1993 to Apr 2014	Jan 2002 to Dec 2013	Jan 2002 to Dec 2013	Jan 2002 to Dec 2013
total number of eddies	823	437	182	360
strong eddies	46 (5.6%)	26 (5.9%)	10 (5.5%)	26 (7.2%)
regular eddies	777	411	172	334
eddy radius R_E [km]				
regular eddies	42.1 ± 11.0	42.6 ± 11.9	37.5 ± 11.0	36.1 ± 9.2
strong eddies	50.6 ± 12.7	52.4 ± 13.0	45.6 ± 15.4	42.4 ± 8.7
transl. speed $\mathbf{u}_E$ [cm s^{-1}]				
regular eddies	20.4 ± 3.9	20.0 ± 4.2	5.2 ± 2.3	4.9 ± 2.8
strong eddies	21.4 ± 1.5	21.4 ± 2.0	8.6 ± 2.9	9.6 ± 2.3
$\lvert SST' \rvert$ [°C]				
regular eddies $\lvert SST'_r \rvert$	0.7 ± 0.5	0.7 ± 0.5	0.6 ± 0.5	0.8 ± 0.8
strong eddies $\lvert SST'_s \rvert$	2.6 ± 0.9	2.8 ± 1.0	1.9 ± 0.6	3.0 ± 1.0
Q_N [GW m^{-1}]	60.1 [21.0, 82.7] (3.7)	59.4 [19.3, 82.7] (5.4)	12.8 [3.2, 17.1] (2.0)	17.7 [2.1, 21.3] (2.5)
% by strong eddies	18%	16%	29%	37%
Q_S [GW m^{-1}]	-64.0 [-86.7, -19.7] (3.9)	-63.3 [-77.5, -16.6] (6.2)	-11.0 [-14.6, -3.9] (1.6)	-21.4 [-31.4, -2.3] (2.7)
% by strong eddies	24%	34%	21%	35%
$\overline{Q}$ [GW m^{-1}]	0.5 [-46.8, 44.6] (3.9)	1.5 [-39.0, 45.1] (5.5)	2.2 [-6.2, 8.2] (1.7)	-2.8 [-9.2, 6.7] (2.3)
% by strong eddies[1]	21%	25%	25%	36%

[1] $\sum \left| Q_{strong} \right| / \sum |Q_{all}|$

In the ANHA4-SPG12 simulation, 360 eddies are detected of which 26 (7.2%) are strong eddies. Here, the contribution of strong eddies is higher than in the observations, accounting for 36% of the absolute surface temperature flux by eddies. The flux by eddies in both directions is larger than in the ANHA4 simulation (around 18-21 GW m^{-1}, Tab. 3.2), and the mean net flux is directed southward (-2.8 [-9.2, 6.7] GW m^{-1}).

Following equation 3.1, three parameters (translation speed $\mathbf{u_E}$, radius R_E, and SST anomaly $\overline{SST'}$) have to be taken into account as possible causes for the anomalously high surface temperature flux of strong eddies. The values for $\mathbf{u}_E$, R_E, and $\overline{SST'}$ (mean ± one standard deviation) are listed in Tab. 3.2.

1. Translation speed ($\mathbf{u}_E$): The average meridional translation speed of strong eddies crossing 47°N is larger than that of regular eddies. This difference is

negligibly small in the observations. In the model simulations the difference is more pronounced with regular eddies moving substantially slower (almost by a factor of two) than strong eddies (Tab. 3.2). Nevertheless, these differences are not large enough to explain the notable difference in surface temperature flux between regular and strong eddies.

2. Eddy radius (R_E): For the observations and both model simulations, strong eddies crossing 47°N are 1.2 times larger than regular eddies (Tab. 3.2). While this can explain a small fraction of the difference between regular and strong eddies, the differences in radii are not large enough to explain the anomalously high surface temperature flux of strong eddies.

3. SST anomaly ($\overline{SST'}$): Most importantly, strong eddies show a substantially larger temperature anomaly than regular eddies. The composite fields of the SST anomalies surrounding strong and regular eddies are shown in Figure 3.6. The average SST anomaly (not regarding the sign of the anomaly) of altimeter-derived strong eddies crossing 47°N ($|SST_s| = 2.8 \pm 1.0$°C) is four times colder/warmer than that of regular eddies ($|SST_r| = 0.7 \pm 0.5$°C, Figure 3.6). The SST anomaly of strong eddies is even stronger related to the sense of rotation of the eddy than it is for regular eddies. For strong altimeter-derived eddies, 80% of the anticyclones are related to a warm SST anomaly, and 80% of cyclones are related to a cold SST anomaly. This behavior is again supported by the model simulations. The average SST anomaly of strong eddies in the ANHA4 simulation is $|SST_s| = 1.9 \pm 0.6$°C, compared to $|SST_r| = 0.6 \pm 0.5$°C for regular eddies. For the strong eddies in the ANHA4 simulation, 6 of the 8 anticyclones are related to a warm SST anomaly, and 2 out of 2 cyclones are related to a cold SST anomaly. In the ANHA4-SPG12 simulation strong eddies have an average SST anomaly of $|SST_s| = 3.0 \pm 1.0$°C, compared to $|SST_r| = 0.8 \pm 0.8$°C for regular eddies. Similar to the observations and the ANHA4 simulation, 6 out of 7 strong anticyclones are related to a warm SST anomaly, and 13 out of 13 strong cyclones are related to a cold SST anomaly.

All in all, a small number of strong eddies, which are associated with a larger SST anomaly than regular eddies, are responsible for about 25% of the absolute surface temperature flux by eddies across 47°N and therefore greatly contribute to the exchange of cold/warm water masses across 47°N. This result is consistent between the observations and the two model simulations with different horizontal resolutions.

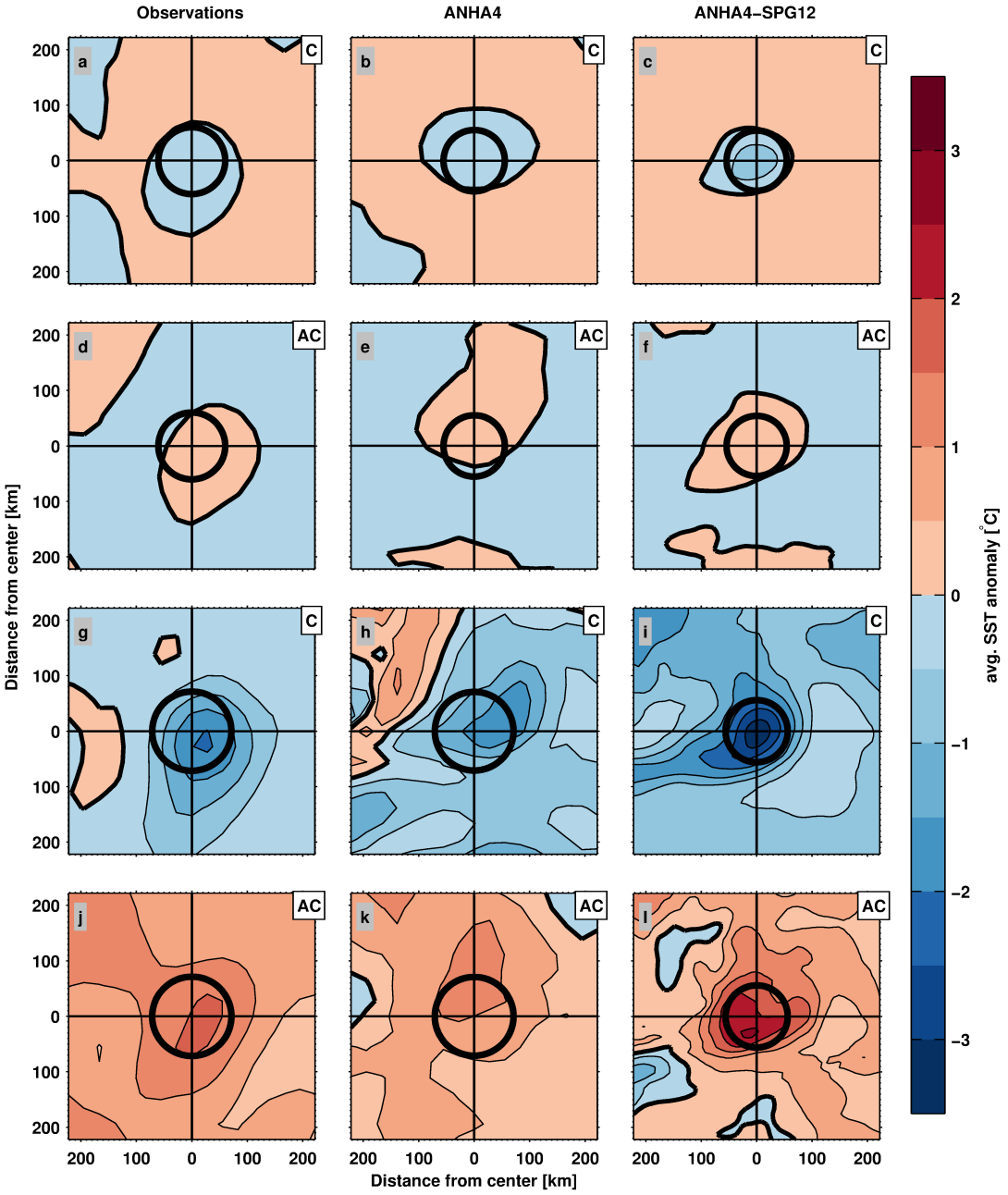

Figure 3.6: Composite of the average SST anomaly associated with eddies crossing 47°N in the observations (left column), 1/4°ANHA4 simulation (center column) and 1/12°ANHA4-SPG12 simulation (right column) for regular cyclonic (subplots a-c), regular anticyclonic (subplots d-f), strong cyclonic (subplots g-i) and strong anticyclonic (subplots j-l) eddies. The number of eddies used to calculate the respective composites differs for each case. The black circle indicates the average eddy radius with a 95% confidence interval.

3.5 Pathways of Eddies Across 47°N in Relation to the Top-To-Bottom Velocity Field

The surface temperature flux by eddies varies not only in time, it also shows considerable regional differences. The focus is now on the spatial distribution of eddies crossing 47°N to look at main pathways of eddies and areas of high eddy abundance. To relate the identified eddy abundance to major branches of the oceanic circulation in the region, the spatial distribution of eddies is compared to vertical sections of the meridional velocities derived from ship surveys and model simulations.

Averaging the LADCP measurements obtained on 11 research cruises between 2003 and 2014 yields a composite meridional velocity section along nominally 47°N (Figure 3.7a). The 12-year means of the meridional velocities from the model simulations are smoother than the composite field of the observations (Figure 3.7b/c). The differences can partly be explained by the different temporal (12-year mean of 5-daily model data vs. average of 11 snapshots) and vertical resolution (between 1 m at the surface and hundreds of meters in the deep ocean in the model vs. 10 m in the observations). Nevertheless, the main structures of the meridional velocity field are well reproduced in both model simulations and consistent with the observations (Figure 3.7). The eastern shelf region is visible in the observations (Figure 3.7a) but not in the model simulations (Figure 3.7b/c), because the ship tracks deviate from the 47°N latitude and are inclined northward towards the shelf (Figure 2.1a).

The western boundary region with the WBC, the NAC and the NBR, is characterized by the highest meridional velocities and strong horizontal shear in the observation and both model simulations (Figure 3.7). The structures in the velocity field in this region are surface intensified but extend down through the whole water column. This behavior and the average position of the three features is consistent between observations and both model simulations. The structure of the WBC is well reproduced in the ANHA4-SPG12 simulation, showing two distinct velocity cores at the continental slope and rise as in the observations (Mertens et al., 2014). In contrast, the WBC in the ANHA4 simulation consists of only one core and is generally weaker with lower velocities and smaller spatial extent. The flow reversal in the Flemish Pass at 47°N (the narrow channel between Flemish Cap and the Grand Banks, Figure 1.4), with a strong southward core in the west and a weaker northward flow at the western flank of the Flemish Cap is well reproduced in both model simulations. The regions over the MAR

and the eastern basin show less spatial variability in the model simulations than in the observations. Note that the eastern part of the section was only covered by 5 of the 11 cruises (Figure 2.1a and Tab. 2.1). The average of the LADCP measurements there is thus less robust than in the western part of the section.

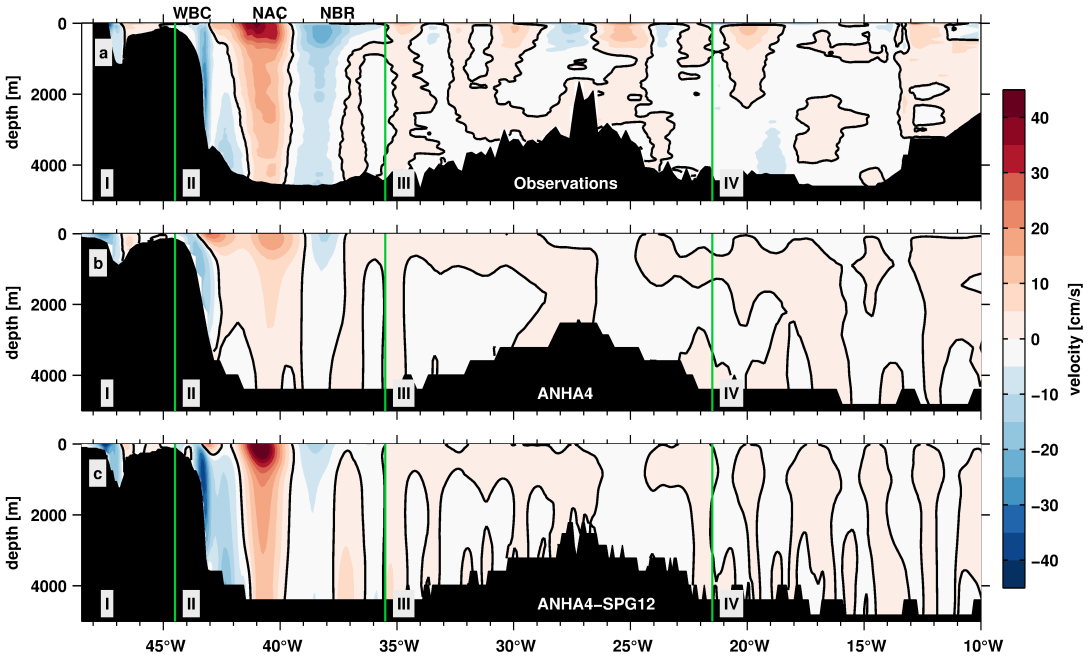

Figure 3.7: Meridional velocity field along 47°N in the observations (a), 1/4°ANHA4 simulation (b) and 1/12°ANHA4-SPG12 simulation (c). For the observations, snapshots from LADCP measurements obtained on 11 research cruises between 2003 and 2014 are averaged. For the model simulations, the mean velocity for the period January 2002 to December 2013 is shown. The position of the Western Boundary Current (WBC), the North Atlantic Current (NAC), and the Newfoundland Basin Recirculation (NBR) is indicated on top. The four subsections along 47°N (I, II, III, and IV) separated by green lines are also indicated in each panel.

For the analysis of the main eddy pathways the number of eddies crossing 47°N are binned into 1° intervals, each centered around one longitude (Figure 3.8). The respective surface temperature fluxes within each bin are summed up to a net (sum of all eddies), a net regular (sum of only regular eddies) and a net strong flux (sum of only strong eddies). In many cases the net regular flux is small, because the northward and southward flux of regular eddies within one bin cancel out each other (Figure 3.9). The direction of the net flux is therefore in most cases dominated by the net strong flux within the respective bin.

Because of the different length of data periods in observations and model, the focus lies on the relative contribution of strong eddies to the surface temperature flux of all eddies within each bin and not on the absolute numbers. For a direct

comparison, the numbers of each bin in Figure 3.8 and Figure 3.9 are normalized with the length of the time series.

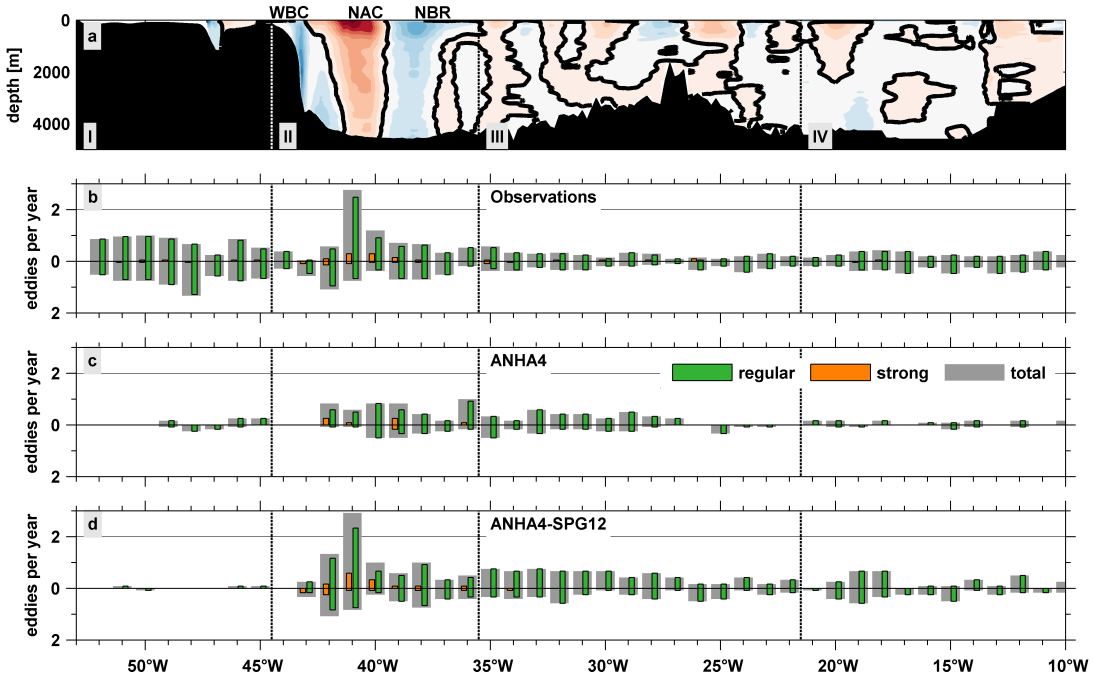

Figure 3.8: Meridional background velocity from the observations (a) and the number of northward and southward moving eddies per 1° bin crossing 47°N per year in the observations (January 1993 to April 2014, b), 1/4°ANHA4 simulation (January 2002 to December 2013, c) and 1/12°ANHA4-SPG12 simulation (January 2002 to December 2013, d). The total number of eddies in each direction (gray) is separated into regular (green) and strong (orange) eddies.

The main eddy pathways are related to the mean background velocity. The section along 47°N is therefore separated into four subsections characterized by different current regimes and different bathymetry (Figure 3.7) and the respective fluxes in these subsections are quantified. The westernmost subsection I comprises the Grand Banks of Newfoundland, the Flemish Pass and the Flemish Cap and stretches until 44.5°W. Subsection II starts from the eastern slope of the Flemish Cap (44.5°W), includes the WBC, the NAC and the NBR and ends at the eastern end of the NBR (35.5°W). The mid-section III spans from 35.5°W to 21.5°W comprising the MAR and its flanks with rough topography, while the eastern most subsection IV stretches from 21.5°W to the eastern end of the study region (10°W).

In the observations and both model simulations, the elevated number of eddies and their direction coincides with regions of high average flow velocity (Figure 3.8). The flow regimes and surface temperature fluxes by eddies in the different subsections are now discussed in more detail.

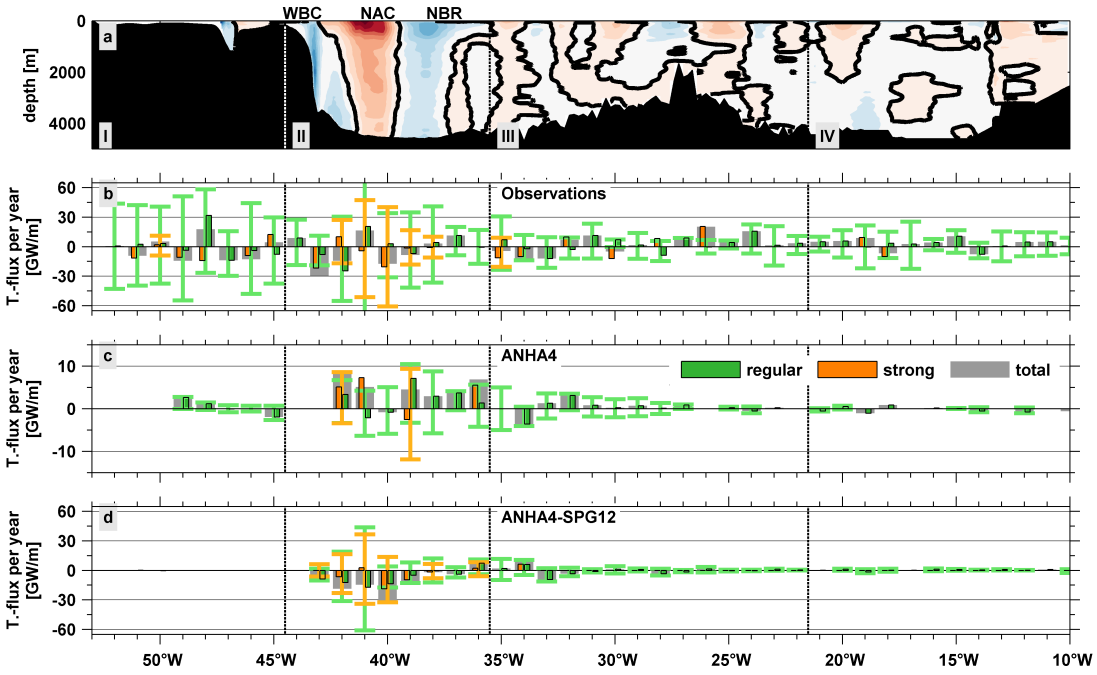

Figure 3.9: Meridional background velocity from the observations (a) and the sum of the surface temperature flux by eddies per 1° bin along 47°N (normalized by the number of years) in the observations (January 1993 to April 2014, b), 1/4°ANHA4 simulation (January 2002 to December 2013, c) and 1/12°ANHA4-SPG12 simulation (January 2002 to December 2013, d). The net flux (gray) is separated into fluxes carried by regular (green) and by strong (orange) eddies. Vertical bars show the sum of the surface temperature flux of regular (green) and strong (orange) eddies in either direction. The vertical whiskers represent the standard deviation of the respective flux in either direction.

3.5.1 Major Eddy Pathways and Associated Surface Temperature Fluxes

Most eddies, most strong eddies, and the highest variability of the surface temperature flux by eddies across 47°N are found in subsection II between 44.5°W and 35.5°W. A total of 261 eddies cross this subsection between 01/1993-04/2014 (Figure 3.8b). There is a narrow band with a large number of eddies moving northward with the NAC in this subsection, while the WBC region is dominated by southward moving eddies. The highest number of eddies (74, i.e. 9% of all eddies) is detected in the 1° bin centered at 41°W (Figure 3.8b).

The spatial pattern of eddy pathways is supported by the ANHA4-SPG12 simulation. Even though the narrow band of northward moving eddies seems slightly shifted westwards, the overall pattern of pathways is remarkably similar to that deduced from the from satellite observations (Figure 3.8c). In ANHA4

there are overall fewer eddies, and the high number of eddies moving northward with the NAC is not reproduced (Figure 3.8d).

The observed surface temperature flux by eddies in either direction is large (>75 GW m^{-1}), leading to a strong variability, while the mean net flux is practically zero (-2.5 [-60.7, 52.0] GW m^{-1}). 28 out of the 261 eddies crossing this subsection are strong eddies. More than 60% (28/46, Tab. 3.2) of all strong altimetry-derived eddies are detected in the Newfoundland Basin. These strong eddies in turn account for 34% of the absolute surface temperature flux of all 261 eddies crossing the subsection (31% of the northward, and 37% of the southward flux, Figure 3.9b). The importance of strong eddies in the western boundary region is supported by both model simulations. With only one exception at 34°W in the ANHA4-SPG12 simulation, strong eddies in the model simulations occur only in the Newfoundland Basin (Figure 3.8c/d).

In the satellite observations the two bins centered around 40°W and 43°W, respectively, show the two largest southward net surface temperature fluxes (Figure 3.9b). These are in turn dominated by the net flux of strong eddies, determining not only the direction but also the magnitude of the net flux. For the bin centered around 43°W, the net flux of strong eddies accounts for 73% of the net flux. In the bin centered around 40°W the southward flux of strong eddies is partially compensated by a northward net flux of regular eddies, and the net flux of strong eddies accounts for 117% of the net flux. This stresses again how important the few strong eddies are for the surface temperature flux carried across 47°N by individual eddies.

But even though these two intervals both show a southward surface temperature flux by eddies, the dynamics behind this transport are fundamentally different. The bin centered around 43°W lies within the WBC, and the southward flux is a result of strong warm eddies moving southward (Figure 3.8b). In the 1° bin centered around 40°W, the majority of eddies move northward with the NAC, but here I still find one of the strongest southward surface temperature flux signals of the whole section (Figure 3.9b). Responsible for this are strong cyclonic eddies carrying a cold SST anomaly northward across the section. The cold SST anomaly most likely stems from the WBC since it is the only source of subpolar water in the region and one of the main regions where eddies are first detected (Figure 3.1c and e.g., Bower et al., 2013).

This process is also found in the ANHA4-SPG12 simulation, where strong northward moving cold-core eddies lead to a southward flux between 39°W - 42°W (Figure 3.8/Figure 3.9d).

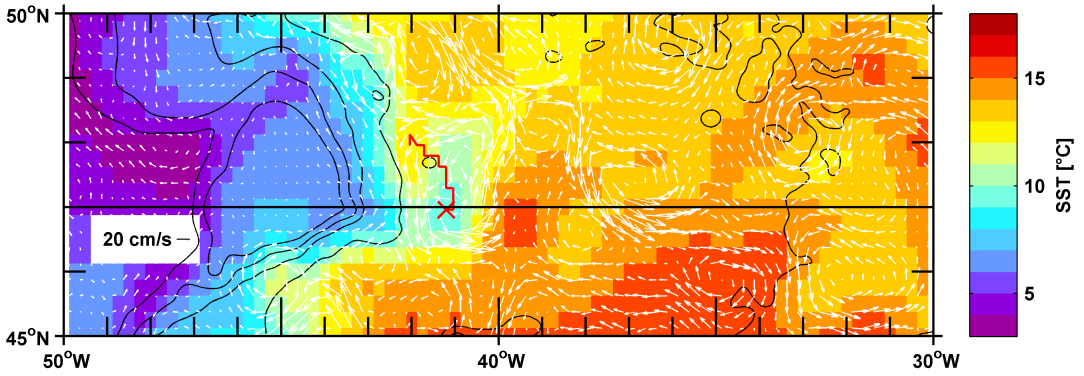

Figure 3.10: Trajectory of a cold cyclone crossing 47°N in June 2010. The eddy was first detected just south of 47°N on June 11, 2010 (**x**). The background color and the white arrows show the SST and the velocity vectors on that day.

One example of an observed northward moving cold cyclone is shown in Figure 3.10. The eddy was first detected one June 11, 2010, just south of 47°N. Analysis of previous snapshots of the velocity field show that its formation process started only a few days earlier close to the southeastern tip of Flemish Cap. The SST in the center of the eddy is more than 5°C colder than the surrounding NAC water. It was tracked until July 17, 2010, when it decayed after crossing over the sea mount located around 41.5°W and 47.8°N.

In the ANHA4 simulation 78 eddies cross the subsection between 01/2002-12/2013, 10 of which are strong eddies. These strong eddies account for 38% of the absolute surface temperature flux of all identified eddies crossing the subsection (41% of the northward, and 34% of the southward flux by eddies, Figure 3.9c). In the ANHA4 simulation there are no eddies in the WBC region around 43°W - 44°W. This lack of eddies coincides with the weak WBC in the ANHA4 simulation (weaker than in the observations and the ANHA4-SPG12 simulation) and stresses that the eddy pathways coincide with the most pronounced current branches.

In the ANHA4-SPG12 simulation 150 eddies cross the subsection. As for the observations, the highest number of eddies is detected in the 1° bin centered at 41°W. Of the 150 eddies, 15 are strong eddies. These in turn account for 44% of the absolute surface temperature flux of all identified eddies crossing the subsection (46% of the northward, and 43% of the southward flux). As in the observations, the WBC region shows a southward flux caused mainly by strong northward moving eddies with a cold temperature anomaly. The effect of cold-core eddies moving northward with the NAC and causing a negative surface temperature flux is even stronger in ANHA4-SPG12 than in the observations, because also the net flux of regular eddies is almost exclusively southward. This confirms the large

contribution of cold-core eddies for the overall surface temperature flux by eddies across 47°N. Both model simulations support the observed large variability in the western basin, with strong fluxes in both directions resulting in a small mean net flux close to zero (4.7 [-7.6, 19.6] GW m^{-1} in ANHA4 and -6.9 [-37.1, 19.1] GW m^{-1} in ANHA4-SPG12).

3.5.2 Minor Eddy Pathways and Associated Surface Temperature Fluxes

The other three subsections play a minor role for the surface temperature flux by eddies across 47°N. There are 258, 152 and 132 eddies found crossing subsections I, III and IV, respectively (Figure 3.8b). The fluxes in either direction in all three regions are lower than in subsection II. They range from 45 to 65 GW m^{-1}, but the resulting mean net surface temperature fluxes in each subsection are practically zero (Figure 3.9b). In the model simulations, the respective surface temperature fluxes in either direction are lower than the observed ones, but the mean net fluxes are also practically zero (Figure 3.9c/d).

One striking difference between observations and the model simulations is the shelf region of the Grand Banks. Unlike in the observations where 132 eddies are detected, there are only 15 eddies detected crossing subsection I in ANHA4 and only 4 eddies at isolated locations in the ANHA4-SPG12 simulation. This difference is due to the small Rossby radius on the shelf ($\sim$ 5 km, Figure 2.3c/d), because the water depth there is so shallow. There is simply no way the model can resolve eddies here (Figure 2.3e/f).

The other regions are better reproduced by the two model simulations. In the observations 68% of all detected eddies in the MAR subsection cross 47°N over the western flank of the MAR. This is backed up by the model simulations with even more eddies crossing the subsection over the western flank (91% in ANHA4 and 76% in ANHA4-SPG12). In all cases, more than half of the eddies move northward and these pathways coincide with surface intensified northward background velocities (Figure 3.7). In the easternmost subsection there are no clearly defined pathways.

Overall the surface temperature flux of eddies crossing 47°N shows high spatial as well as temporal variability (denoted by the whiskers in Figure 3.9b/c/d). The largest fluxes as well as the highest variability are observed in the western basin. These findings are coherent in observations and the two model simulations.

3.6 Discussion and Conclusion

Previous studies have focused on the strength and position of the WBC and NAC and their interaction using results from drifters and floats (e.g., Rossby, 1996; Kearns and Rossby, 1998; Carr and Rossby, 2001; Dutkiewicz et al., 2001; Bower et al., 2009) as well as direct current measurements and hydrographic observations (e.g., Pérez-Brunius et al., 2004; Kieke et al., 2009; Rhein et al., 2011; Mertens et al., 2014). The southward flow of the WBC, the northward flow of the NAC, and the strength of the anticyclonic recirculation cell east of the Grand Banks have been quantified by Mertens et al. (2014) using shipboard and moored current meters along 47°N and the high-resolution (1/20°) VIKING20 ocean model. They have shown that about 2/3 (80 Sv) of the total NAC transport crossing 47°N (110 Sv) are recirculated locally in the Newfoundland Basin, while only about 1/3 (30 Sv) of the northward flow makes it east to cross the MAR (Mertens et al., 2014; Roessler et al., 2015).

While major parts of the large-scale circulation in the interior North Atlantic can now increasingly be quantified, fluxes associated with small-scale features like eddies still need to be addressed. This chapter of my thesis illustrates the importance of individual strong eddies that are linked to a notably large SST anomaly for the surface temperature flux by eddies across 47°N. For the eddy detection and the calculation of the respective surface temperature fluxes, I use data from two completely independent observational data sets (gridded geostrophic velocities provided by AVISO and sea surface temperatures from satellite radiometry), and two model simulations with different resolution, which all show coherent patterns.

The eddy detection algorithm used in this thesis was designed to be a reliable tool for distinguishing between meanders and eddies (Nencioli et al., 2010). I am therefore confident that it is a particularly well suited method to detect actual eddies in the study region, where meandering of the NAC plays an important role for the dynamics in the region.

Using a combination of 21 years of geostrophic velocities from satellite altimetry, sea surface temperature data and ship-based velocity measurements, as well as two simulations with the NEMO ocean model with different resolutions spanning a period of 12 years, I have found:

- The highest numbers of eddies in the subpolar North Atlantic are detected along the pathway of the NAC and in the observations also on the shelf of the Grand Banks of Newfoundland (Figure 3.1).

- About 25% of the absolute surface temperature flux by eddies across 47°N stems from eddies with a notably large SST anomaly, so-called strong eddies (Figure 3.6 and Figure 3.9).
- The western part of the Newfoundland Basin with the fastest and most pronounced current branches is the major pathway for eddies and their associated surface temperature flux across 47°N (Figure 3.8 and Figure 3.9).
- Northward moving cold-core cyclones carrying subpolar water from the WBC make a considerable contribution to the overall surface temperature flux by eddies in the Newfoundland Basin (Figure 3.1c and Figure 3.9).
- The eastern basin of the North Atlantic at 47°N shows a small contribution to the surface temperature flux carried by eddies (Figure 3.9).
- While the number of detected eddies is lower in both model simulations, the key findings are consistent between observations and the two model configurations with 1/4° and 1/12° resolution, respectively (Figure 3.8 and Figure 3.9).

Relative to the respective model environment all features considered in this study (i.e. importance of strong eddies, size of eddies, mean background velocity, major eddy pathways) are well reproduced in both the 1/4° and the 1/12° simulation. But there are also striking differences between the models and the observations. Most importantly, there are fewer eddies detected in both model simulations compared to the observations (56% of the observed eddies in ANHA4 and 72% in ANHA4-SPG12). The model simulations show promising results for quantifying eddies in the North Atlantic relative to the respective model environment. However, the results suggest that a higher resolution than 1/12° is needed in order to fully reproduce the observed amount of eddies. Despite the different resolutions and the different numbers of eddies, the radii of the detected eddies are remarkably similar. So it is not simply the case that smaller eddies exist in the observations that are not reproduced in the models. There are overall fewer eddies in the models than in the observations, but the eddies that are formed in the models on average still show similar properties as the eddies in the observations. Therefore, even though I did not study the processes leading to the actual formation of eddies in this thesis, it is likely that some of these processes (e.g. baroclinic instabilities) are not sufficiently resolved in the models.

Strong eddies occur most often in the Newfoundland Basin, where they account for about one third of the surface temperature flux by eddies. The number of both regular and strong eddies in the region and their respective direction of translation are clearly connected to the position and strength of the background velocity field. Dengler et al. (2004) found that the Deep Western Boundary Current (DWBC) in the South Atlantic breaks up into eddies around 8°S, while for a weak DWBC a stable, laminar flow seems possible. A similar behavior is observed in the ANHA4 simulation where a weak NAC and WBC coincide with lower numbers of eddies compared to the observations and ANHA4-SPG12, where the background flow is stronger (Figure 3.7/3.8). The resulting surface temperature fluxes on the other hand are linked mostly to the SST anomalies, and even though the strongest fluxes are found in the region with the highest velocities, the direction of the flux does not necessarily correspond to the direction of the mean velocity field.

In the western boundary region (subsection II), where the largest surface temperature fluxes are found (mean northward flux 76.0 GW m^{-1} and mean southward flux -76.9 GW m^{-1}), the mean flux is practically zero because the large northward flux (especially in the NAC region) is compensated by large southward fluxes in the NBR region around 40°W and in the WBC. This result is supported by Mertens et al. (2014) who found that the largest part of the NAC recirculates locally in the Newfoundland Basin and about half of the WBC recirculates into the NAC. The eddies from the present study, first detected in the region between WBC and NAC (Figure 3.1c), provide a means for the local exchange between the boundary and the interior of the North Atlantic described by Dutkiewicz et al. (2001), Bower et al. (2009) and Kieke et al. (2009). The eastern basin shows so few eddies crossing 47°N, because here the NAC runs mainly in a zonal direction northward of the section.

Several other studies have used satellite altimetry observations and automated eddy detection schemes to analyze mesoscale variability in the ocean. For example Chelton et al. (2011) applied a SSH-based detection algorithm to 16 years of global AVISO altimetry data (October 1992 - December 2008) with 1/4° horizontal resolution (interpolated from 1/3°) and a 7-day temporal resolution. Dong (2012) used the same algorithm as used in this thesis, but they applied it to a global set of geostrophic velocities from AVISO altimetry from January 1993 to December 2010 with 1/3° horizontal resolution and a 7-day temporal sampling. Despite the differences in method, temporal and spatial resolution and the different length of the time series, the spatial distributions of detected eddies in the subpolar North

Atlantic by Chelton et al. (2011) and Dong (2012) agree well with the distribution of eddies found in this study.

The comparison of the distribution of detected eddies with the mean EKE in the region has shown that the two do not necessarily coincide (Figure 3.1). This is supported by Rhein et al. (2011) who found in a model study that the strongest variability in the western basin is caused by meandering of the front between NAC and WBC rather than by actual eddies.

Rossby (1996) has already described how the mean pathway of the NAC closely follows the bathymetry of the Newfoundland Basin, forms relatively stable meanders with cyclonic features located on the western side of the NAC and anticyclonic features on the eastern side. This admittedly schematic pathway of the NAC is reflected in the distribution of eddies along the Grand Banks. The cyclonic features on the western side of the NAC in turn coincide with the strong cyclonic eddies found in the present study. These features trap anomalously cold water from the WBC that is then carried back northward with the NAC, crossing 47°N in a narrow band around 40°W.

The open question still remaining is: How much of the total meridional heat flux at 47°N (about 0.6 PW, (e.g., Ganachaud and Wunsch, 2000; Rhein et al., 2011)) is achieved by eddies? With the method used in this chapter I am not able to answer this question and can only assess the relative contribution of different types of eddies for the surface temperature flux by eddies. For a more complete understanding of the fluxes by eddies, data from the deep ocean is needed to infer the vertical structure of the eddy.

Other studies (e.g., Dong et al., 2014; Zhang et al., 2013, 2014) have shown first attempts of combining detected eddies with observed temperature and salinity profiles from Argo floats. While this method shows potential for extending the two dimensional surface fluxes in this study to volume fluxes with a vertical component, presently available Argo observations in the North Atlantic are still too scarce to directly combine each detected eddy with a respective temperature or salinity profile. A promising method to infer the vertical structure of eddies from their respective SLA signature is the Gravest Empirical Mode (GEM) technique (Chapter 4.2).

In the following chapter, I will use temperature and salinity data reconstructed from SLA using the GEM method to quantify volume fluxes by eddies. Unfortunately, it is not possible to calculate a GEM for the entire study region in the North Atlantic (Chapter 4.2, Fig. 4.3). There is no GEM data for the eastern part of the Easter Atlantic, as well as for the shallow Grand Banks. The reasons

for this are discussed in chapter 4.2. However, the results from the analysis of surface fluxes has shown that the major pathway of eddies crossing 47°N is in the Newfoundland Basin. Neglecting the fluxes from the eastern basin will therefore result in a lower estimate of the total fluxes, but will not affect the overall structure of observed fluxes by eddies.

The analysis of surface fluxes have shown that the 1/12° ANHA4-SPG12 configuration of the model shows more realistic results than the 1/4° configuration when it comes to the representation of eddies. Therefore, from here on only the 1/12° configuration will be used for the three dimensional analysis of eddy properties, and temperature and freshwater fluxes by individual eddies.

4 Volume Fluxes of Temperature and Freshwater related to Eddies

4.1 Example of an Eddy from Ship Observations

During RV Maria S. Merian cruise MSM43 in June 2015 a northward moving cold-cored cyclonic eddy crossing 47°N was observed using LADCP and temperature measurements from Conductivity Temperature Depth (CTD) casts (Figure 4.1a). The eddy is also clearly visible in the AVISO geostrophic velocity field available for the same time (Figure 4.1c).

Tracking the eddy with the algorithm described in chapter 2.4 shows that it was first detected on April 29, 2015 slowly moving northward and crossing 47°N on June 6, 2015. The eddy then intensified (increasing rotational speed), and was observed from the ship around June 16. The cruise track cuts through the southern part of the eddy, with CTD profile 72 located close to the center of the eddy and profiles 71 and 73 located in the eddy boundary where the rotational velocities are highest (>1 ms^{-1}). The regions of the highest velocities at the eastern and western eddy boundaries correspond to the strongest density gradients (Figure 4.1a) and to the outer shape of the eddy defined by the detection algorithm (Figure 4.1c). The surface temperature anomaly when comparing the temperatures of profile 72 inside the eddy to the surrounding profiles 71 and 73 is larger than -3.5°C. The maximum anomaly of almost -7°C is found at a depth of around 100 m. Below the depth of 500-600 m the temperature anomaly is much smaller than at the surface (Figure 4.1b), but the isotherms located at greater depth are still lifted by around 500 m. The observed surface temperature anomaly from CTD measurements fits well into the range of SST anomalies of strong eddies detected in the satellite observations in the previous chapter. Even though the eddy described here is only one example of an in-situ observed eddy, it shows the effect of strong cyclones in the NAC region and gives an idea about the vertical structure of eddies in the Newfoundland Basin.

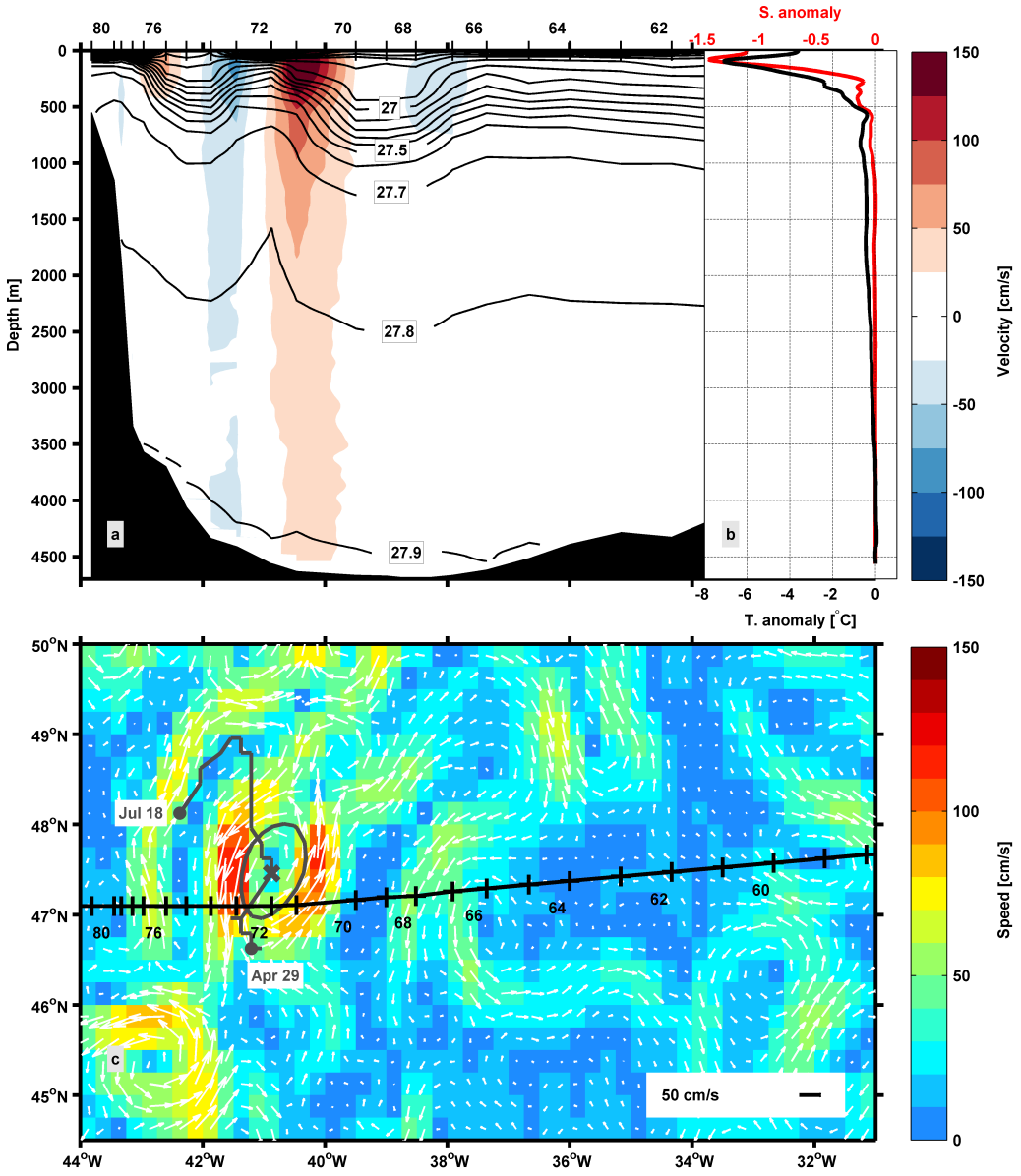

Figure 4.1: (a) Meridional velocities from LADCP measurements overlayed with potential density (σ_θ) from CTD measurements along 47°N. Measurements were carried out during RV Maria S. Merian cruise MSM43 between June 11 and June 18, 2015. (b) Temperature and salinity anomaly profiles (inside - outside eddy) related to the eddy (profile 72 - average of profiles 71 and 73). (c) shows a top view of the eddy with a snapshot of the speed and the velocity vectors from AVISO geostrophic velocities on June 16, 2015 (day of profile 72 inside the eddy). The gray line shows the trajectory of the eddy between April 29 and July 18. The 'x' marks the center of the eddy on June 16, 2016 and the outer shape on that day. The black line indicates the cruise track of the ship along 47°N. The positions of the individual stations are marked at the top of panel (a) and along the cruise track in panel (c).

In the following chapter I will use profiles of temperature and salinity reconstructed from SLA in order to analyze the vertical structure of eddies in the

subpolar North Atlantic and calculate the volume fluxes of temperature and freshwater associated with individual eddies crossing 47°N. In the following, I will omit the "volume" unless the context requires a direct comparison to surface fluxes.

4.2 3-D Fields of Temperature and Salinity from the Gravest Empirical Mode Method

Since the aim is to quantify fluxes by eddies (with a vertical component), data from the ocean interior is needed. Most promising would be temperature and salinity data from Argo floats, but they are still too scarce in the North Atlantic to directly relate every detected eddy to a vertical temperature and salinity profile. Also the time period covered by the Argo program is short (since 2000) compared to the AVISO satellite observations (since 1993).

I therefore use the high resolution (daily from January 1993 to December 2014, 1/4° horizontal resolution, 10 dbar vertical resolution) salinity and temperature fields introduced by Stendardo et al. (2016). The data sets are constructed from sea level data using the Gravest Empirical Mode (GEM) technique (e.g., Meinen and Watts, 2000; Meijers et al., 2011). The method exploits the relationship between T/S profiles from Argo observations and dynamic height in order to parametrize the hydrographic structure as a function of the dynamic height from satellite altimetry. This means the GEM is the first empirical mode of a hydrographic parameter in relation to the dynamic height. Even though temperature and salinity data constructed from SLA with the GEM method are not measured directly, I will use the term observations (in contrast to model results) to describe the fluxes derived from the GEM data in the following chapters.

Since the water properties change from region to region, the GEMs have to be calculated for different regions individually. Stendardo et al. (2016) use 7 different regions for the North Atlantic between 35°N and 55°N. One example of such a GEM is shown in Figure 4.2.

For each region the deseasonalized Argo data (i.e. seasonal cycle removed) is interpolated to a regular vertical grid with 10 dbar resolution. A cubic spline function between the dynamic height computed from Argo profiles referenced to 1900 dbar and temperature/salinity is then fitted to the data at each vertical interval. The resulting GEMs are look-up tables that assign a value of temperature and salinity at a certain depth to a certain dynamic height value (Figure 4.2).

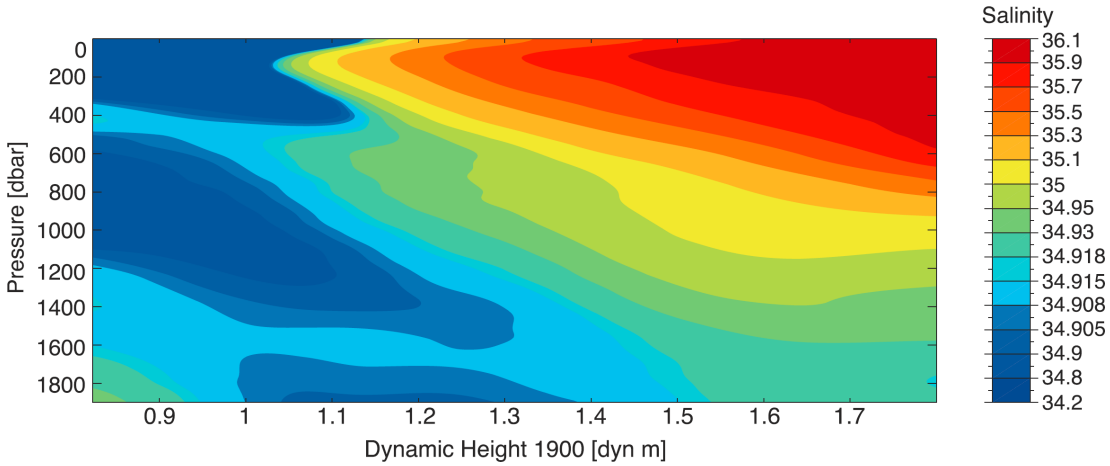

Figure 4.2: Example of a GEM for salinity in the "Newfoundland Basin west" region, relating a profile of salinity to each value of dynamic height (Stendardo et al., 2016, their Figure 2).

Since the absolute dynamic topography (ADT) fields from AVISO are defined for the whole water column, they cannot be used directly with the GEM look-up table. In order to have temperature and salinity profiles with the same temporal and spatial distribution as the AVISO product, a new ADT field referenced to 1900 dbar has to be constructed in order to use the GEM. For this, the mean dynamic height (MDT) referenced to 1900 dbar is derived from salinity and temperature climatologies from the World Ocean Atlas 2013 (WOA13, Locarini et al., 2013; Zweng et al., 2013) and then added to the SLA from satellite altimetry. The resulting ADT fields are referenced to 1900 dbar and span the whole time period considered in this thesis (January 1993 - December 2014). The GEM look-up table can now be used to link these ADT fields to the most likely temperature and salinity profiles.

A detailed description of the method as well as a evaluation of the different region has been done by Stendardo et al. (2016). Here, I will only mention the two main constraints that explain why we cannot simply use the GEM method everywhere in the Atlantic: (1) A relation between temperature and salinity is necessary. (2) The SLA needs to be dominated by the baroclinic signal of the water column. This can be checked for example by calculating the regression coefficients between SLA from satellite-altimetry and the steric height from Argo measurements in the region (Stendardo et al., 2016, their Figure 4). For the regions considered in this thesis the correlation between the two ranges from 0.87 to 0.91. The linear regression coefficients are applied to the SLA from AVISO before adding the MDT from the WOA13 in order to make the two products "compatible".

Due to the two limitations mentioned above, regions with low stratification such as the Labrador and Irminger seas or regions with ambiguous T/S relationships (such as the eastern Eastern Atlantic where warm and salty water from the Mediterranean Sea flows into the Atlantic) are not suited for the construction of T/S profiles with the GEM method (Stendardo et al., 2016).

For the analysis here, three fields from Stendardo et al. (2016) were merged. (1) Newfoundland Basin west (NFLw, extended slightly to the west in order to better capture the WBC), (2) Newfoundland Basin east (NFLe) and (3) Rockall Through (RT). In the overlapping areas between the regions, the values from both fields are linearly interpolated. The interpolation weight from the western region is decreasing linearly eastward from 1 to 0, and the weight from the eastern region is increasing accordingly (personal communication R. Steinfeldt, IUP Bremen, 2017).

The GEM lookup tables and the fields of ADT were constructed by Ilaria Stendardo. I was provided this data and the respective scripts to calculate the temperature and salinity fields for the different regions. I then used the interpolation suggested by Reiner Steinfeldt in order to obtain one merged field. The merged fields of temperature and salinity reach down to 1900 dbar and range from 44.625°W - 17.625°W and from 45.125°N - 49.875°N (Figure 4.3a). The water depth must be deep enough to reference the ADT to 1900 dbar and therefore no GEM data can be obtained in regions shallower than ∼2000 m (Figure 4.3b). The section at 47°N is therefore not fully covered by the temperature and salinity fields. The western part is too shallow, while the eastern part is not suited due to water masses from the Mediterranean Sea. Since the vertical grid of the data sets is in pressure coordinates, all fields first have to be interpolated to a depth grid in the vertical direction in order to calculate the fluxes by eddies.

Since Stendardo et al. (2016) have already provided a detailed evaluation of the individual regions, there will not be an evaluation of the merged field at this point. Stendardo et al. (2016) have analyzed the quality of the constructed profiles by comparing the mean differences and the root-mean-square error (RMS) between the GEM profiles and the Argo profiles used to construct the GEM, as well as the signal-to-noise ratio (SNR) for the GEM profiles. The SNR at a certain depth is defined as the ratio between the range of GEM values at that depth (signal) and the RMS at the respective depth (noise). For the regions of interest here, they have shown that the GEM method captures up to ∼90% of the variance in the upper 700 dbar of the water column (Stendardo et al., 2016, their Figure 6). The RMS values are below 0.2, and mean differences between GEM and Argo profiles

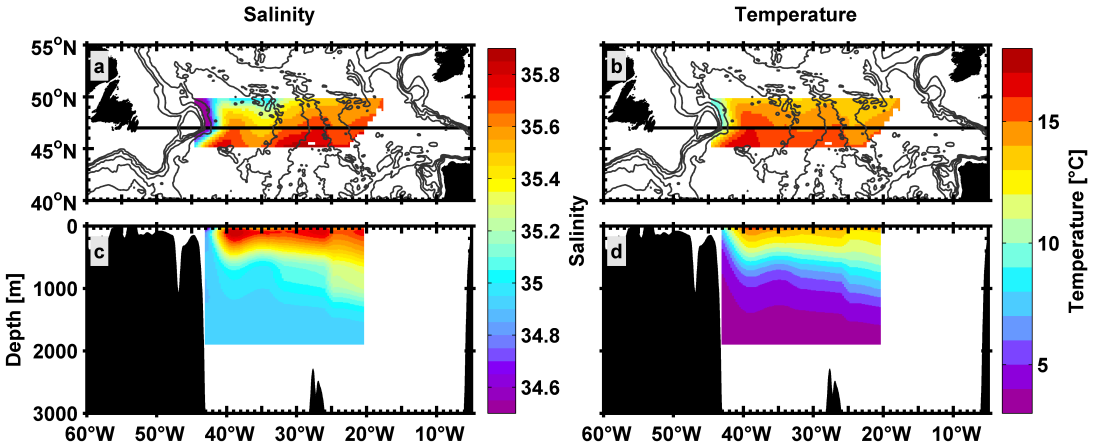

Figure 4.3: Average surface salinity (a) and temperature (b) of the GEM region for the period January 1993 to December 2014. The black line indicates the section at 47°N. The reconstructed average salinity and temperature along the section at 47°N is shown in (c) and (d). Isobaths are given every 1000 m using bathymetry derived from the ETOPO1 data set (Amante and Eakins, 2009). The bathymetry is lowpass-filtered to highlight general features.

have a similar range. Below 700 m the changes in salinity are much smaller than close to the surface, and the GEM fields only capture a smaller amount of the variance. Nevertheless, Stendardo et al. (2016) have shown that the SNR is still high (>10) for the deep part of the profiles below 700 m.

They also showed that historic salinity sections measured with CTD casts during hydrographic cruises can be reproduced using the salinity fields produced with the GEM method (Stendardo et al., 2016, their Figure 7). Other studies have successfully used the GEM method to investigate the subsurface structure of the temperature and salinity field in the Southern Ocean (e.g., Swart et al., 2010; Meijers et al., 2011).

In the following I will demonstrate how the salinity and temperature profiles constructed from the GEM method are used to infer temperature and freshwater fluxes by individual eddies. Even though Stendardo et al. (2016) have shown that the fields constructed with the GEM method are not as robust below 700 m as they are for the upper part of the water column, I will use the full profiles to a depth of 1900 dbar. At this point in time there is simply no alternative data for assigning a temperature and salinity profile to each eddy. Fortunately, the variability of temperature and salinity in the deep ocean is much lower than at the surface and the differences between profiles inside and outside eddies are very small and approaching zero with increasing depth (Figure 4.4d).

4.3 Calculation of Temperature and Freshwater Fluxes related to Eddies

The temperature and salinity fields derived from the GEM method are used to calculate temperature and freshwater fluxes associated with individual eddies observed from satellite altimetry. For the model simulation, the full model fields are used for the calculation. Freshwater is defined with respect to a reference salinity; $FW = \frac{S_{ref}-S}{S_{ref}}$, where $S_{ref} = 34.8$, a typical reference value for the North Atlantic. Freshwater therefore is not an absolute quantity. The freshwater value is positive if the water is less saline than the reference and negative if the water is more saline than the reference.

There is one important methodical difference for the calculation of the fluxes associated with eddies between surface fluxes and volume fluxes. The anomalies for the volume fluxes are calculated *spatially* with respect to the local surrounding, while those for the surface temperature fluxes are calculated *temporally* with respect to the mean annual cycle (see chapter 3.1 for details). This is done for several reasons: (1) It allows to compare the two methods and thus makes the results more robust if both methods show the same results. (2) Due to the drift in the model, there would always be an artificial trend in the freshwater fluxes caused solely by the salinity drift. This is avoided by calculating the anomaly with respect to the surrounding. (3) On a purely practical note, it would be almost 5000 times more expensive to calculate the anomalies for every depth level of the GEM fields (191 depth levels) and the ANHA4-SPG12 model simulation (50 depth levels) than calculating only the surface anomalies for the surface fluxes.

A schematic of an anticyclonic eddy and typical temperature profiles from the GEM method are shown in Figure 4.4. All profiles located inside the eddy (Figure 4.4a, blue area) and outside the eddy (Figure 4.4a, red area) are averaged. The outside area is defined as a ring around the eddy with a radius of $2 \times R_E$. The anomalies caused by individual eddies ($\overline{T'}$, and $\overline{FW'}$) are then calculated relative to the surrounding temperature/freshwater (inside eddy - outside eddy).

Since individual eddies are linked to an anomaly, this anomaly can be used to calculate the vertical extent of the respective eddy (H_{eddy}). I used the temperature anomaly profile $\overline{T'} = \overline{T_{in}} - \overline{T_{out}}$ (Figure 4.4d) to identify the vertical extent. H_{eddy} is defined as the depth where the maximum temperature anomaly associated with the eddy has dropped by a factor of 10 ($\overline{T'} = \frac{1}{10}\, T'_{max}$, where T'_{max} is the maximum anomaly of the temperature profile). If no vertical extent can be defined by this criterion (because the critical value is not reached), $\frac{1}{n}\, T'_{max}$, with $n = 9, 8, 7$,etc.

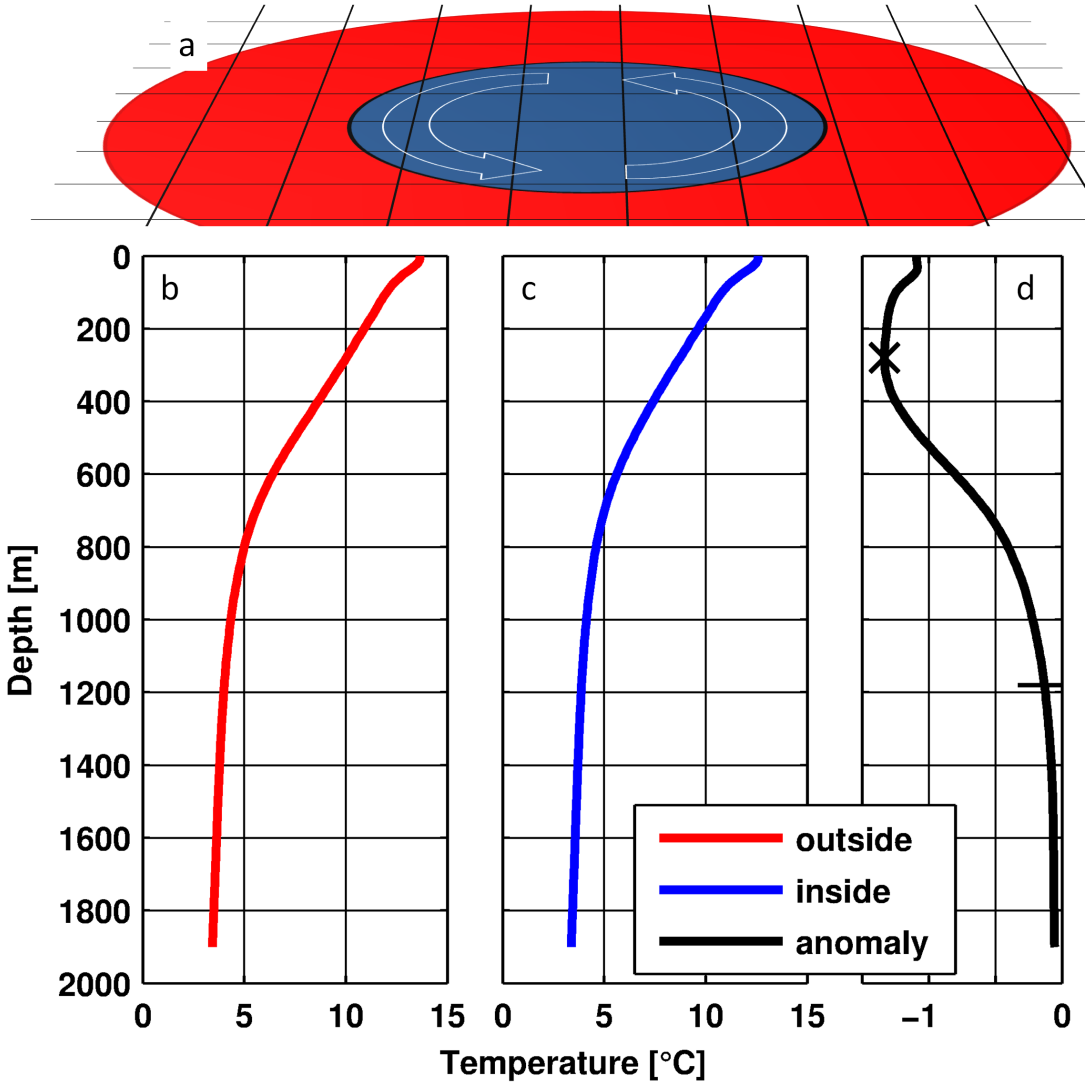

Figure 4.4: Area outside (red) and inside (blue) of a cyclonic eddy (a) with the corresponding averaged temperature profiles outside (b) and inside (c) of the eddy and the respective temperature anomaly (inside - outside) profile (d). The maximum temperature anomaly (mark at 280m) is used to calculate the vertical extent (horizontal line at 1180m).

is used as critical values instead. If the critical value gets larger than $\frac{1}{5}\ T'_{max}$, the vertical extent calculation is considered as failed.

The temperature flux $\mathbf{F_T}$ is then calculated as:

$$\mathbf{F_T} = \mathbf{u}_E\ 2R_E\ c_{p_0} \int_{H_{eddy}}^{0} \left[\overline{\rho}\,(z)\ \ \overline{T'}\,(z)\right] dz \tag{4.1}$$

where $\mathbf{u}_E$ is the eddy's translation velocity, R_E is the radius of the individual eddy, $c_{p_0} = 4200$ J kg^{-1} K^{-1} an average specific heat capacity for sea water, $\overline{\rho}\,(z)$

is the average density profile calculated from the respective temperature and salinity profiles inside the eddy, and $\overline{T'}(z)$ is the average temperature anomaly profile within the area ($A = \pi R_E^2$) of the eddy. The unit of temperature flux caused by eddies is Watt.

Similar to the temperature flux, the freshwater flux $\mathbf{F_{FW}}$ is calculated as:

$$\mathbf{F_{FW}} = \mathbf{u}_E \; 2R_E \int_{H_{eddy}}^{0} \left[\overline{FW'}(z)\right] dz \tag{4.2}$$

where $\overline{FW'}(z)$ is the average freshwater anomaly profile within the area ($A = \pi R_E^2$) of the eddy. The unit of the freshwater flux is $\mathrm{m^3 s^{-1}}$ or mSv ($1\mathrm{mSv} = 10^{-3}\mathrm{Sv} = 10^3 \mathrm{m^3 s^{-1}}$).

One might wonder why the temperature flux is not called heat flux, since it is the transport of heat by individual eddies. In physical oceanography, the term heat flux usually implies (1) that the calculated heat flux flows into (or out of) a closed volume, and (2) that the net mass flux through this closed volume is zero. With these assumptions it is possible to directly calculate the heating or cooling of the considered volume from the fluxes on its boundaries.

While the definition of the fluxes by eddies (equation 4.1) implies that there is no mass flux by eddies relative to the (unknown) background state, it is not possible to derive unique GEM fields for the whole Atlantic. I can therefore not consider a closed zonal section and the heat flux by eddies is not an absolute quantity. The flux cannot be used to directly quantify the heating or cooling in the region north of 47°N, since it might be compensated by an unknown southward flux in the eastern part of the section (and also by fluxes through Bering Strait). Using the term temperature flux instead should therefore avoid false assumptions about the nature of the fluxes across 47°N analyzed here.

4.4 Evaluation of the GEM Method in the Presence of Eddies

Stendardo et al. (2016) have provided an evaluation of the GEM method for the different regions introduced in their paper. In the following I will show that the GEM method is also useful for assigning temperature and freshwater anomalies to individual eddies.

For the evaluation only those eddies with at least one Argo profile inside and outside of the eddy were used. For this, every detected eddy was taken into account (and not just the ones tracked for at least one week). In the period

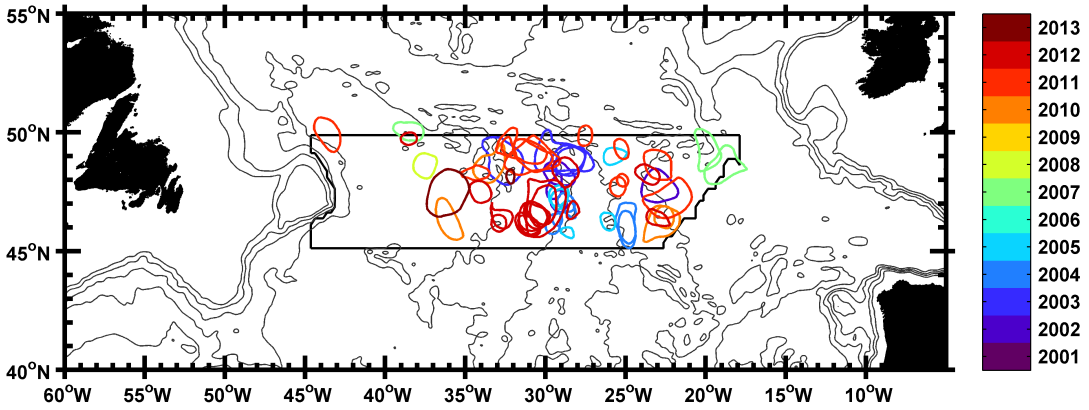

Figure 4.5: Contours of the 65 eddies in the GEM region with at least one Argo profile inside and outside of the eddy. Eddies from different years are indicated with different colors

between January 1993 and December 2014, there were 16 cyclonic and 49 anticyclonic eddies in the GEM region that met the aforementioned conditions (Figure 4.5). Almost no eddies in the western basin, where most eddies cross 47°N, are sampled by Argo profiles. The best coverage of eddies sampled with Argo profiles is after the year 2010. The mean profiles of temperature and salinity anomalies (inside eddy - outside eddy) from Argo floats are reproduced reasonably by the GEM profiles (Figure 4.6).

The temperature and salinity differences between GEM and Argo are largest between the surface and around 500 m depth, but all differences are lower than 1°C and below 0.1 for salinity. The maximum RMS is between 1.3 and 1.5 for the temperature profiles and around 0.25 for salinity (Figure 4.7). Overall, the results for both RMS and SNR are similar to the ones found by Stendardo et al. (2016). The SNR is obviously lower when only taking into account the profiles that are related to eddies instead of all profiles on a 1/4°×1/4° grid. For the 16 cyclonic eddies, the SNR is 3.6 ± 0.5 for temperature and 3.5 ± 0.5 for salinity. For the 49 anticyclonic eddies, the SNR is 5.4 ± 0.7 for temperature and 5.1 ± 0.9 for salinity.

For the Argo floats, there is an asymmetry between cyclonic and anticyclonic eddies when regarding the depth of the maximum anomaly of the average temperature and salinity profiles. The maximum temperature anomaly for the averaged Argo profiles lies at 380 m for cyclonic and at 600 m for anticyclonic eddies (Figure 4.6a). This asymmetry is not well reproduced when looking at the average of the corresponding GEM profiles (500 m for cyclonic and 540 m for anticyclonic eddies). The same holds for the salinity profiles. For anticyclonic eddies, the

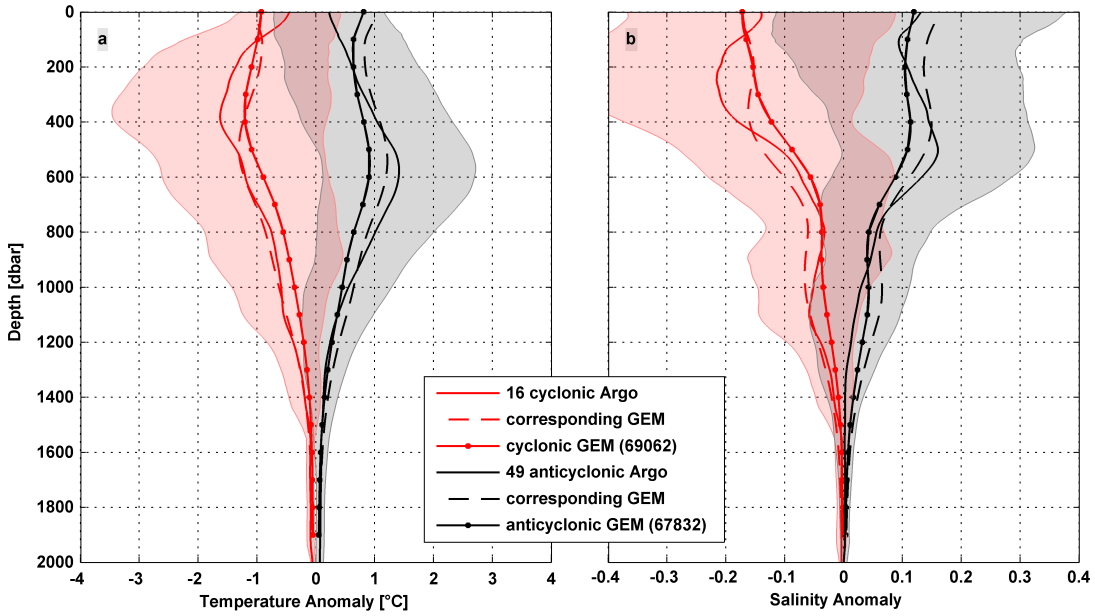

Figure 4.6: Mean temperature (a) and salinity (b) anomaly profiles (inside - outside eddy) for cyclonic (red) and anticyclonic (black) eddies from Argo (solid lines), derived from the respective GEM profiles (dashed lines) and from all GEM profiles (69062 in cyclonic eddies and 67832 profiles in anticyclonic eddies) in the region (line with markers). The shaded area represents one standard deviation of the Argo profiles. The profiles are smoothed with a 100 dbar running mean (±50 dbar).

maximum salinity anomaly of the average profile is more than twice as deep (500 m) than for cyclonic eddies (210 m). The asymmetry is not reproduced by the average GEM profiles, where the maximum anomaly is located at the surface.

Using all GEM profiles (69062 profiles in cyclonic eddies, 67832 profiles in anticyclonic eddies) instead of only the ones with corresponding Argo profiles, leads to more realistic results. Again, every detected eddy (and not just the ones tracked for at least one week) was taken into account. The maximum temperature anomaly for the average of all cyclonic eddies is located at 360 m depth and the one for anticyclonic eddies at 550 m depth. The picture for salinity is not as clear, and the salinity maxima of the averaged GEM profiles are located at the surface. However, the average salinity profile for anticyclonic eddies shows a local salinity maximum at 420 m depth. And while there is no local maximum for cyclonic eddies, there is a saddle point in the average salinity profile for cyclonic eddies at 210 m. This behavior fits well to the observed Argo profiles and to the asymmetric behavior of cyclonic and anticyclonic eddies found in earlier studies (e.g., Dong et al., 2014, their Figure 2).

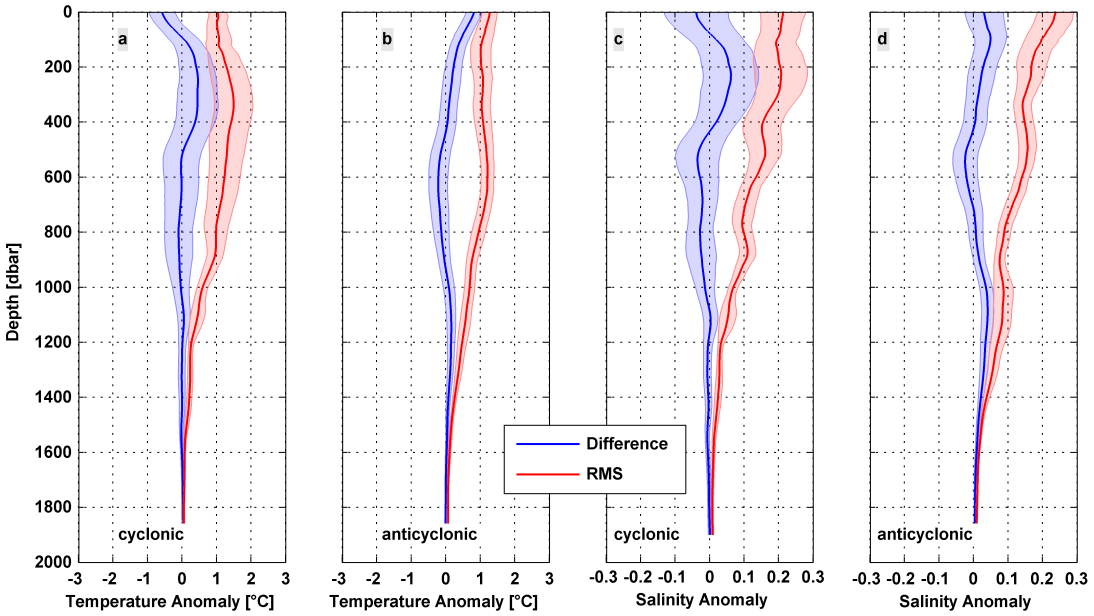

Figure 4.7: Mean temperature (a,b) and salinity (c,d) differences (red) and root-mean-squares (RMS, blue) between the profiles constructed from the GEM method and the corresponding profiles from Argo floats. Cyclonic (a,c) and anticyclonic (b,d) eddies are regarded separately. The profiles are smoothed with a 100 dbar running mean (±50 dbar). The shaded areas represent the 90% confidence intervals of the mean differences and RMS, respectively. They were computed by bootstrapping the mean difference and the RMS at each depth level with 1000 iterations.

The different depths of the maximum anomaly for cyclonic and anticyclonic eddies can be explained by the eddies' effect on the underlying isopycnals. Cyclonic eddies lift the isopycnals while anticyclonic eddies depress them. The cyclonic eddy observed during cruise MSM43 described in chapter 4.1 lifted the isopycnals by roughly 500 m (Figure 4.1a).

4.5 Vertical Eddy Characteristics in Observations and ANHA4-SPG12 Model

In the following I will analyze in more detail the characteristics of detected eddies focusing on the vertical extent and the vertical structure. As described in chapter 4.3 the vertical extent (H_{eddy}) is defined as the depth where the temperature anomaly related to the eddy has decreased to 1/10 of the maximum anomaly.

For the model simulation it would theoretically be possible to calculate the vertical extent using the eddy-detection algorithm on every depth level of the

model and checking up to which depth the eddy can be detected. This leads in many cases to underestimated vertical extent, because the rotational velocities in depth are weaker than at the surface. This is also visible in the observed eddy shown in Figure 4.1. The algorithm then tends to "lose" the eddy before reaching the actual vertical extent. To avoid this false calculation of the vertical extent and to keep the definition consistent between observations and model, the vertical extent is defined exactly the same way for observations and model using the temperature anomaly profiles.

The mean temperature and salinity profiles from the ANHA4-SPG12 simulation in comparison to the average profiles constructed with the GEM method are shown in Figure 4.8. The anomalies in the model simulation are in general somewhat smaller than the GEM anomalies, but always within one standard deviation of the GEM profiles.

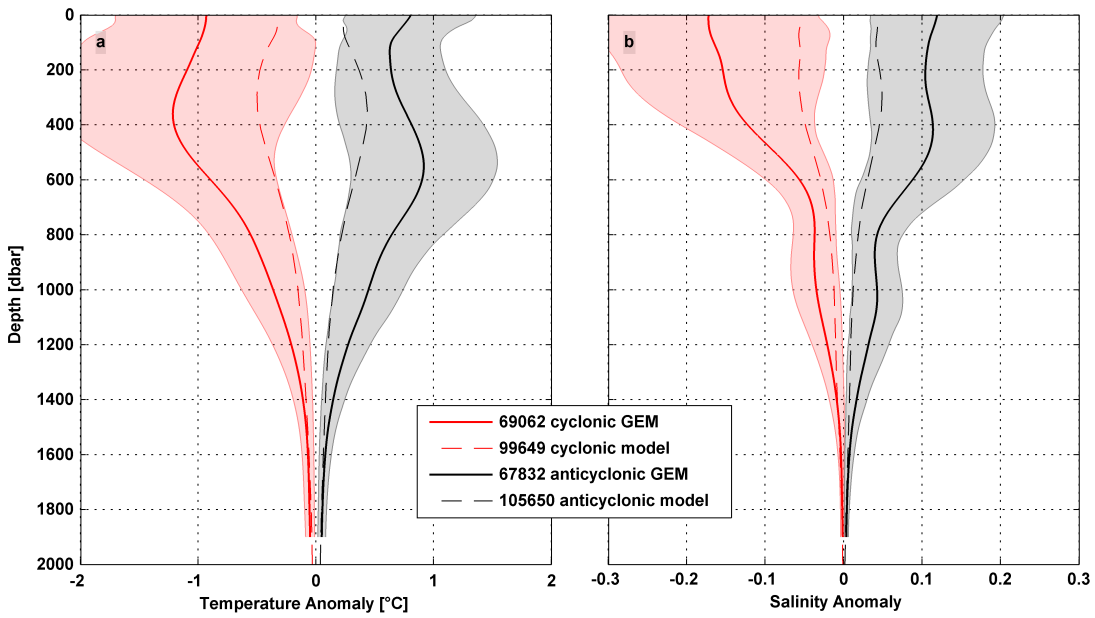

Figure 4.8: Mean temperature (a) and salinity (b) anomaly profiles (inside - outside eddy) for cyclonic (red) and anticyclonic (black) eddies from all GEM profiles (69062 in cyclonic eddies and 67832 profiles in anticyclonic eddies) and all profiles from the ANHA4-SPG12 simulation (99649 cyclonic and 105650 anticyclonic eddies). The shaded area represents one standard deviation of the GEM profiles. The GEM profiles are smoothed with a 100 dbar running mean (±50 dbar). Note that the GEM region is smaller than the model domain.

4.5.1 Vertical Extent of Eddies in Observations and Model

For the observed eddies with temperature profiles from the GEM method, the average (median) vertical extent is 1400 m. The distribution of vertical extents is shown in Figure 4.9a. Only very few eddies (less than 1%) extend to less than 600 m. Due to the depth limitation of the GEM profiles, the maximum vertical extent of observed eddies is 1900 m. However, there is a sharp drop of the distribution before reaching the maximum depth and only less than 1% of the eddies extend to more than 1800 m (Figure 4.9a). This indicates that only very few eddies are actually cut off by the limited depth of the GEM profiles. Most striking is the peak between 1400 m and 1500 m for anticyclonic eddies. Anticyclonic eddies reach on average 200 m deeper (median vertical extent 1460 m, inner quartile: 1290 m - 1600 m) than cyclonic eddies (median vertical extent 1250 m, inner quartile: 1040 m - 1510 m). So not only the depth of the maximum anomaly differs between cyclones and anticyclones (as described in the previous chapter), but also the total vertical extent (Figure 4.9a).

The vertical extent of the eddies detected in the ANHA4-SPG12 model generally show a wider distribution than the observed eddies and there is practically no difference between cyclonic and anticyclonic eddies (Figure 4.9b). On average the eddies in the model are somewhat shallower than in the observations with a median vertical extent of 1250 m (inner quartile: 760 m - 1700 m). There are more shallow eddies as well as more deep reaching eddies than in the observations. More than 10% of the eddies in the model are shallower than 600 m (compared to less than 1% in the observations) and around 16% of all simulated eddies extend deeper than 2000 m (Figure 4.9b). However, the uncertainty of the vertical extent for deep reaching simulated eddies is large (200 m - 300 m) because there are only 5 depth levels between 1800 m and 3000 m in the model.

4.5.2 Composites of Temperature and Freshwater Anomalies associated with Eddies

Since the eddy's vertical shape is usually not simply a cylinder, Dong et al. (2012) separated the eddies they analyzed based on model output of the Southern California Bight into bowl-shaped (largest size at the surface), cone-shaped (largest size at 400 m depth) and lens-shaped (largest size in the stratification layer) eddies. Dong et al. (2014) have therefore introduced a constant coefficient s in order to account for the vertical shape of the eddy when calculating the temperature and salinity fluxes in equation 4.1 and equation 4.2. They chose s=0.5, as it

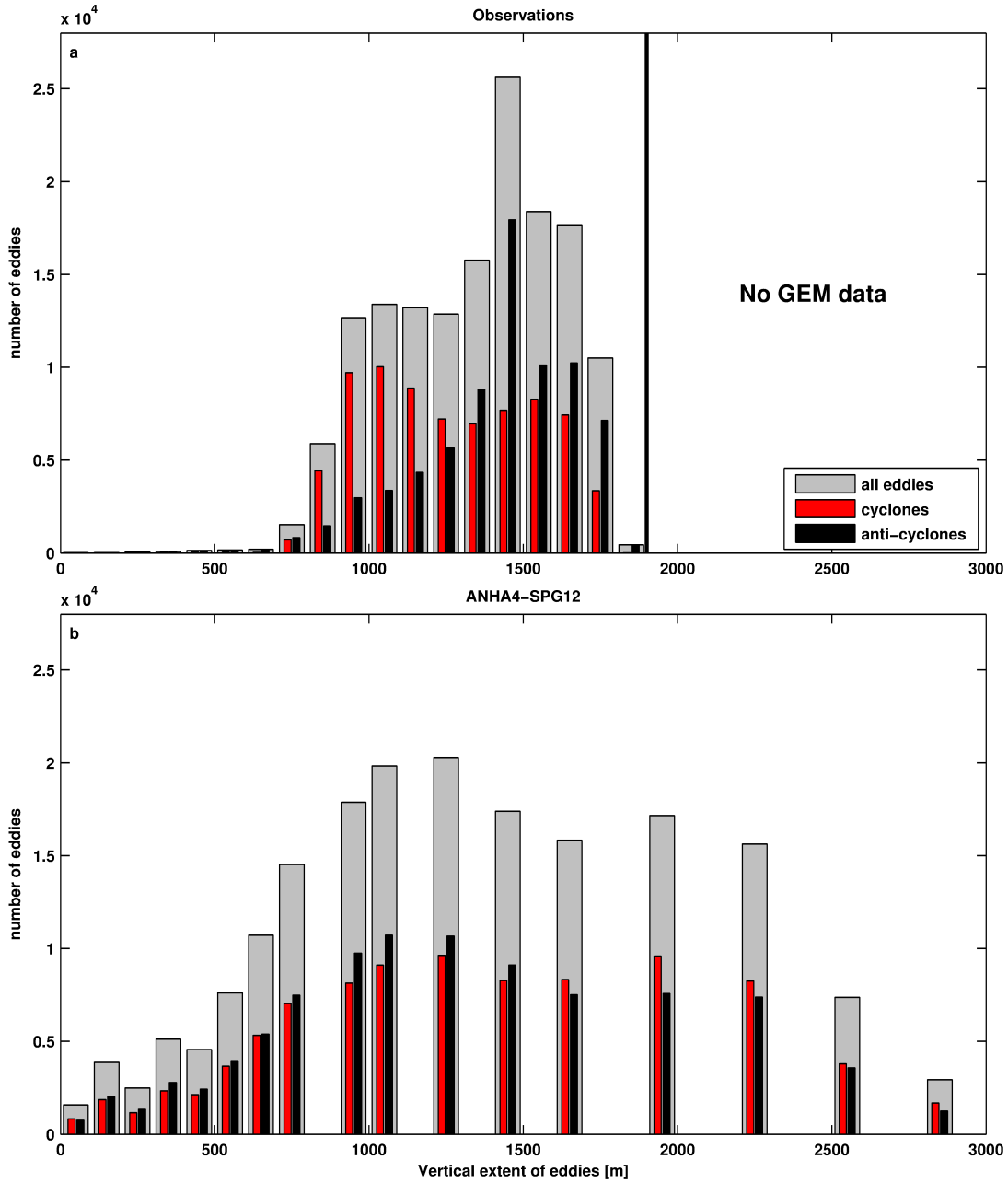

Figure 4.9: Distribution of the vertical extent of detected eddies from satellite observations (a) and the 1/12°ANHA4-SPG12 model simulation (b). The distance between the bars increases for the model simulation due to the decreasing vertical resolution with depth (see chapter 2.3 for more detail).

represents "a conservative choice of the vertical shape effect on eddy flux" (Dong et al., 2014).

In order to get an idea about the vertical shape of the eddies detected in the Subpolar North Atlantic, the composite temperature and freshwater anomalies of all cyclonic/anticyclonic eddies with a lifetime longer than one week are inferred and analyzed (observations: 38465 cyclonic/36372 anticyclonic, model: 66359 cy-

clonic/63088 anticyclonic). The composite sections are constructed as follows: For every eddy, the zonal section (x-z plane) through the eddies' center is taken. The dimensions in x-direction are transformed into multiples of the eddy's radius by normalizing the distance from the eddy center with the respective eddy's radius (with a horizontal resolution of 1/2 R). In order to isolate the eddy signal, the mean stratification is subtracted from each individual section to obtain anomalies of temperature and freshwater. The respective anomalies for cyclonic and anticyclonic eddies are averaged to obtain a composite for each sense of rotation. The composite anomalies for cyclonic/anticyclonic eddies are shown in Figure 4.10.

The most striking difference between observations and model simulation is the magnitude of the maximum anomaly. For the observed fields the mean maximum temperature anomaly for all eddies (without regard for the opposite sign for cyclones and anticyclones) is |2.1°C| and |9×10−3| for the respective freshwater fields. With |0.7°C| and $|3 \times 10^{-3}|$, respectively, the maximum anomalies in the model simulation are by a factor of 3 smaller than the observed ones (Figure 4.10).

The similarities between the composite fields in observations and model simulation are best visible when normalizing each composite field by it's maximum anomaly (Figure 4.11). The previously described difference between cyclonic and anticyclonic eddies regarding the depth of the maximum anomaly as well as the full vertical extent is also reflected when analyzing the composite sections of temperature and freshwater. Apart from opposite signs and the difference in vertical extent, cyclonic and anticyclonic eddies show a similar vertical shape for both temperature and freshwater in the observations as well as the model simulation (Figure 4.11). Using the same terminology as Dong et al. (2012), the form of the temperature composites found here can be described as lens-shaped in both observations and model. They show a clear maximum below the surface, and the size is largest somewhere between 500 m and 1000 m. The composites for freshwater on the other hand are bowl-shaped. The size is largest at the surface and decreasing with increasing depth (Figure 4.11).

Neither of the forms suggests the use of a coefficient to correct the flux with regard to the vertical shape of the eddy as introduced by Dong et al. (2014). Since using a correction coefficient would only decrease the respective fluxes by a constant factor and not change the temporal variability, I refrained from using such a coefficient. Actually, the anomalies for temperature and freshwater exceed the eddy radius calculated from the detection algorithm in all cases (Figure 4.11,

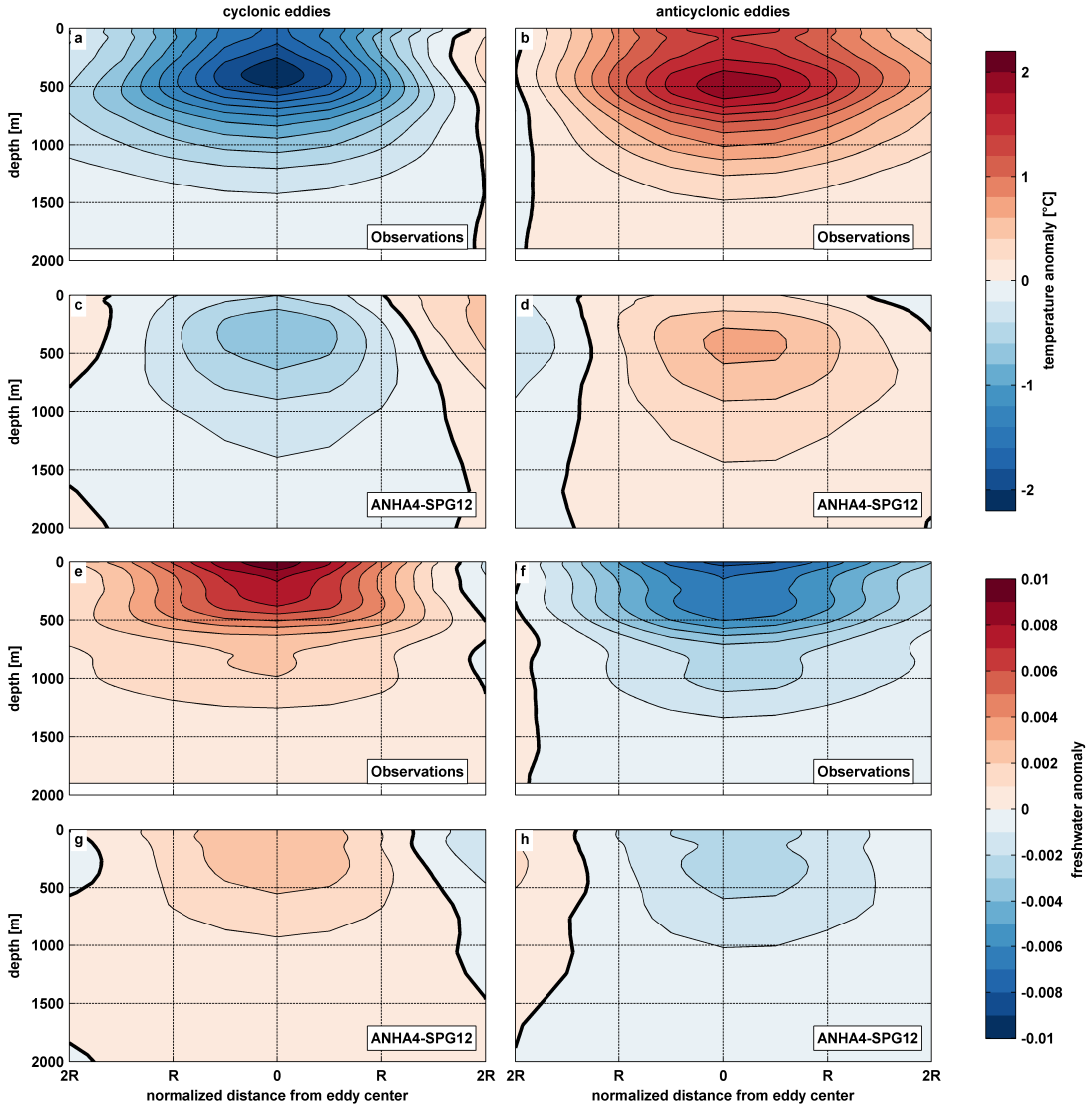

Figure 4.10: Composites of the temperature (a-d) and freshwater anomalies (e-h) associated with eddies from observations (a/b/e/f, 38465 cyclonic/36372 anticyclonic) and the 1/12°ANHA4-SPG12 model simulation (c/d/g/h, 66359 cyclonic/63088 anticyclonic). The x-axis is given in multiples of eddy-radii. The thick black line indicates the zero-line. Negative freshwater values indicate that the water is more saline than the average reference salinity (34.8).

thick black lines). Assuming a cylindrical shape with one eddy radius down to the vertical extent of the eddy will therefore still result in a rather conservative estimate for the fluxes associated with the eddies.

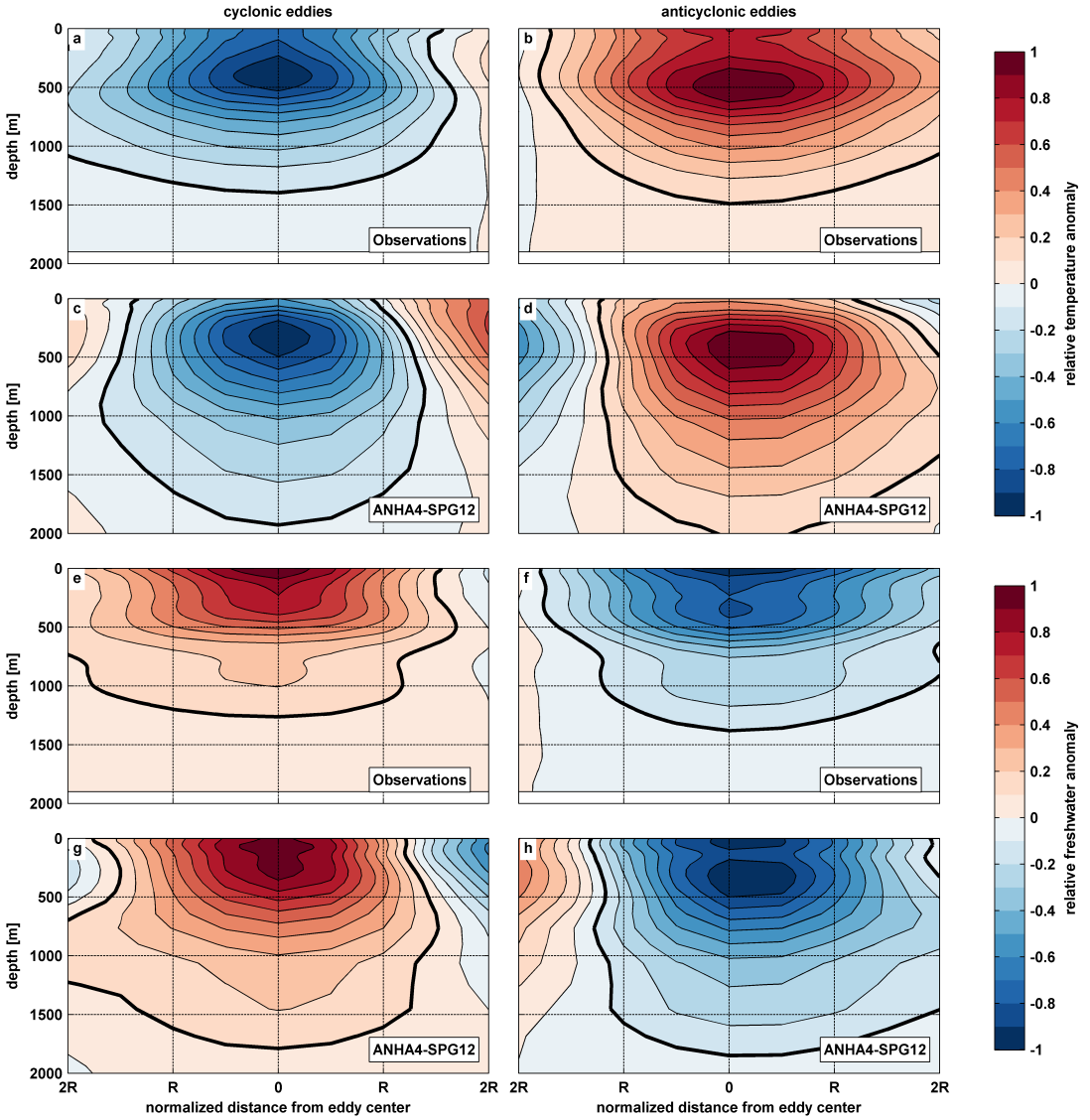

Figure 4.11: Normalized composites of the temperature (a-d) and freshwater anomalies (e-h) associated with eddies from observations (a/b/e/f, 38465 cyclonic/36372 anticyclonic) and the 1/12°ANHA4-SPG12 model simulation (c/d/g/h, 66359 cyclonic/63088 anticyclonic). The composite fields are normalized with their respective maximum value. The x-axis is given in multiples of eddy-radii. The thick black line indicates the -0.1/0.1 contour (i.e. the line that is used for the calculation of the vertical extent). Negative freshwater values indicate that the water is more saline than the average reference salinity (34.8).

4.6 Temperature and Freshwater Fluxes carried by Eddies across 47°N

The focus in chapter 3 was on the surface temperature fluxes by eddies crossing 47°N and the pathways that eddies take when crossing the section. Using temperature and freshwater data constructed with the GEM method allows for the

first time to assign temperature and freshwater profiles to each individual eddy and to analyze the respective fluxes (F_T and F_{FW}) across 47°N.

Obviously, also this method has its limitations; the temperature and salinity fields from the GEM method are only reconstructed from SLA and not directly observed. They are also limited in space, because not every region is suited to construct a unique GEM (only part of the 47°N section is covered, Figure 4.3). The surface fluxes from satellite observations in chapter 3 on the other hand give no information about the vertical extent of eddies, and the model simulations are only a model of reality and have a drift for salinity as well as low vertical resolution in depth. However, combining the results from the different methods (2D, 3D, and model) can provide a robust picture of the temperature and freshwater fluxes by individual eddies in the subpolar North Atlantic.

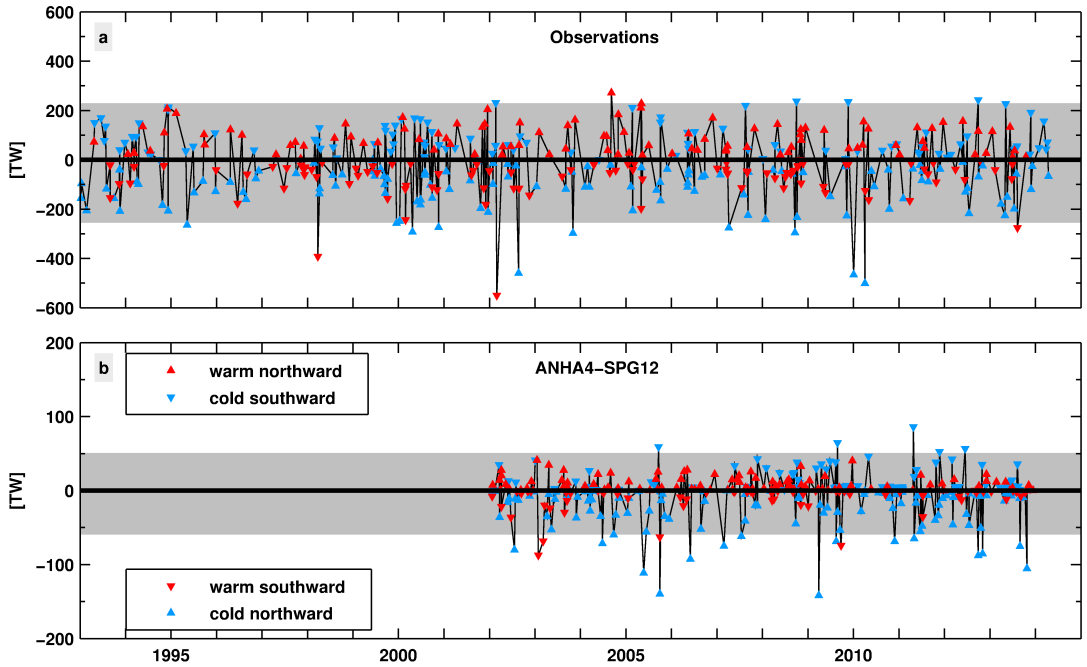

Figure 4.12: Time series of the meridional temperature flux by eddies across the zonal section at 47°N in the observations (a, only part of the section is covered) and 1/12°ANHA4-SPG12 simulation (b), 1 TW = 10^{12} W. Red (blue) triangles indicate eddies with a warm (cold) temperature anomaly. The direction of the triangle indicates the direction of meridional eddy movement across 47°N (northward/southward). A positive (northward) temperature flux can be achieved by northward moving warm eddies as well as southward moving cold eddies (and vice versa for a negative temperature flux, see text for details). The gray areas indicate two times the standard deviation of each time series. Note that the panels have different scales.

Just as for the surface temperature fluxes, eddies are again separated into "regular" and "strong eddies", depending on the associated temperature flux.

Strong eddies are defined as all those eddies with a temperature flux that exceeds the mean flux plus two times the standard deviation in either direction ($\overline{F_T} \pm 2 \times \sigma(F_T)$, where the overbar denotes the mean, and σ is the standard deviation, Figure 4.12). All other eddies are defined as regular eddies. In order to account for the extreme values while calculating the standard deviations, the calculation is repeated 10000 times with random subsamples of the time series, each with 1/3 of the length of the original time series, and then averaged. I use the temperature flux to keep the method consistent with the definition of strong eddies in chapter 3.4, but using the freshwater flux instead would not make a difference (Figure 4.13). As for the previous chapters all numbers displayed here are given as a mean value, and the variability is represented by the inner quartile range (i.e. 50% of the values). The numbers are summarized in table 4.1.

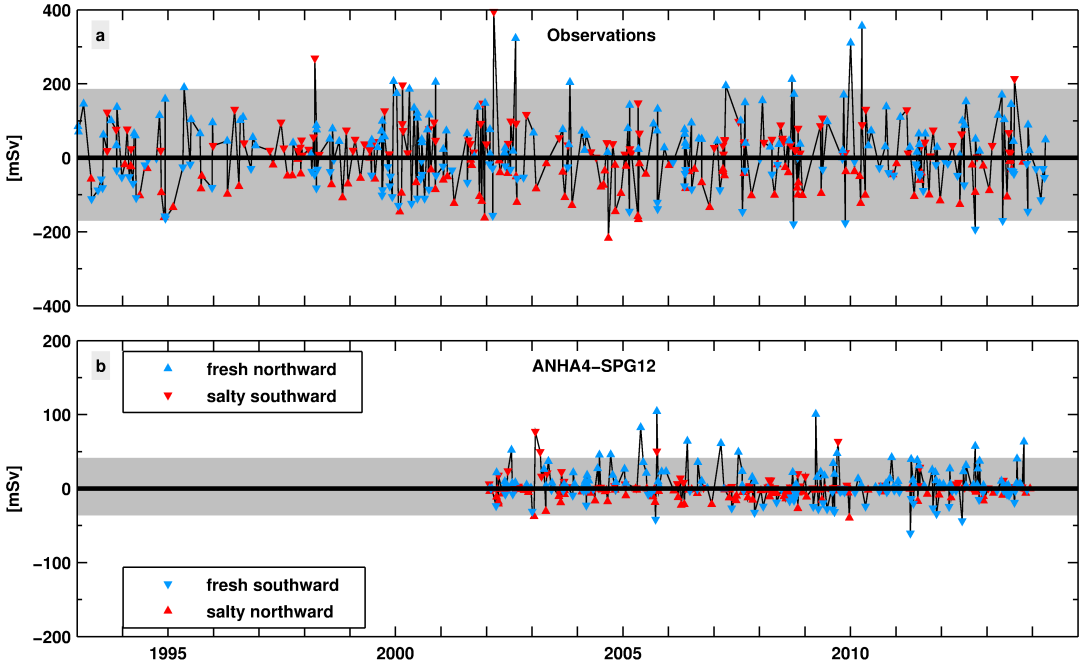

Figure 4.13: Time series of the meridional freshwater flux by eddies across the zonal section at 47°N in the observations (a, only part of the section is covered) and 1/12°ANHA4-SPG12 simulation (b), 1 mSv = $10^3 m^3/s$. Blue (red) triangles indicate eddies with a fresh (salty) freshwater anomaly. The direction of the triangle indicates the direction of meridional eddy movement across 47°N (northward/southward). A positive (northward) freshwater flux can be achieved by northward moving fresh eddies as well as southward moving salty eddies (and vice versa for a negative freshwater flux). The gray areas indicate two times the standard deviation of each time series. Note that the panels have different scales.

In the observations between January 1993 and April 2014, a total of 415 eddies with a lifetime of more than 7 days and radius larger than $R_{min} = 20 \times cos(\phi)$ were detected crossing 47°N in the region covered by the GEM field (Figure

4.12a). This means that half of the eddies detected at the surface (408 out of 823) are outside of the GEM region. Contrary to the surface fluxes, the mean net temperature flux across 47°N $\overline{F_T}$ is significantly different from zero and directed southward (-12.8 [-80.2 62.5] TW). 18 (i.e. 4.3%) of the 415 eddies crossing 47°N are strong eddies, making up for 15% of the absolute temperature flux (i.e. $\sum \left|F_{T\,strong}\right| / \sum |F_{T\,all}|$) and even 21% of the southward temperature flux. 98% of all eddies crossing 47°N are either cold and fresh cyclones or warm and salty anticyclones. Therefore, freshwater fluxes are directed opposite of the temperature fluxes. The mean net freshwater flux is also significant and directed northward (8.2 [-43.8 53.8] mSv). The influence of strong eddies is the same as for the temperature flux, with 15% of the absolute and 20% of the northward freshwater flux carried by strong eddies. On average, a strong eddy ($\overline{|F_{strong}|}$) accounts for nearly 4 times of the temperature and freshwater flux of regular eddies ($\overline{|F_{regular}|}$).

Table 4.1: Number of eddies crossing 47°N and the respective temperature and freshwater fluxes. The variability shown in brackets represents the inner quartile range (i.e. the range of 50% of the values). The standard error of the mean value within a 90% confidence interval (given in parentheses) was calculated from bootstrapping the mean value with 1000 iterations. See text for the definition of strong eddies.

	Observations		**Model (ANHA4-SPG12)**	
period	Jan 1993 to Apr 2014	Jan 2002 to Dec 2013	Jan 2002 to Dec 2013	Jan 2002 to Dec 2013
zonal extent	43°W - 20.5°W	43°W - 20.5°W	43°W - 20.5°W	53°W - 10°W
total number of eddies	415	237	283	357
strong eddies	18 (4.3%)	13 (5.5%)	25 (8.8%)	25 (7.0%)
regular eddies	397	224	258	332
F_T North [TW]	86.6, [39.1 127.5], (5.5)	84.5, [35.5 125.9], (8.2)	15.5, [4.2 23.8], (1.7)	12.7, [2.2 18.8], (1.4)
% by strong eddies	7%	13%	15%	14%
F_T South [TW]	-100.8, [-132.2 -40.8], (7.6)	-99.3, [-123.8 -38.0], (11.2)	-25.6, [-35.8 -5.0], (3.0)	-20.6, [-30.0 -2.0], (2.5)
% by strong eddies	21%	25%	46%	45%
$\overline{F_T}$ [TW]	-12.8, [-80.2 62.5], (7.5)	-12.5, [-69.0 56.6], (10.3)	-5.2, [-12.9 10.7], (2.3)	-4.1, [-9.1 6.2], (1.9)
% by strong eddies[1]	15%	20%	34%	34%
F_{FW} North [mSv]	73.8, [31.4 98.5], (5.6)	72.7, [28.9 95.5], (8.0)	17.8, [3.8 23.4], (2.2)	14.3, [1.5 21.6], (1.9)
% by strong eddies	20%	24%	46%	45%
F_{FW} South [mSv]	-64.9, [-98.6 -28.9], (4.1)	-64.4, [-99.8 -25.6], (6.1)	-11.2, [-16.8 -2.8], (1.2)	-9.2, [-13.5 -1.8], (1.0)
% by strong eddies	7%	13%	13%	13%
$\overline{F_{FW}}$ [mSv]	8.3, [-48.0 61.4], (5.7)	7.9, [-43.2 51.4], (7.5)	3.4, [-7.3 9.6], (1.6)	2.6, [-4.6 6.0], (1.3)
% by strong eddies[2]	15%	19%	34%	33%

[1] $\sum \left|F_{T\,strong}\right| / \sum \left|F_{T\,all}\right|$, [2] $\sum \left|F_{FW\,strong}\right| / \sum \left|F_{FW\,all}\right|$

The eddies detected in the ANHA4-SPG12 model simulation show a similar behavior as the observed eddies, but strong eddies play an even more important role for the total fluxes. There are a total of 357 eddies crossing 47°N from January 2002 to December 2013. For 3 of the 360 eddies in chapter 3.4 the depth calculation from the temperature anomaly profile failed and therefore no flux could be calculated either. The three eddies are excluded and not further considered for the analysis. As for the observations, 99% of the eddies in the model simulation are either cold and fresh cyclones or warm and salty anticyclones. The mean net temperature flux is southward (-4.1, [-9.1 6.2] TW) and the mean net freshwater flux northward (2.6, [-4.6 6.0] mSv). 25 (i.e. 7%) of the 357 eddies are strong eddies, accounting for 34% of the absolute temperature and 33% of the absolute freshwater fluxes.

For the direct comparison of model and observations I will focus on the zonal extent and the time period that are covered by both GEM field and ANHA4-SPG12 simulation (43°W - 20.5°W, limited by the GEM region, and January 2002 - December 2013, limited by the model run). In this case there are actually more eddies in the 1/12° simulation (283) than in the observations (237). Both temperature and freshwater flux have the same signs as the observed fluxes and are significantly different from zero. The mean net fluxes in the model are by a factor of 2.4 (temperature) and 2.3 (freshwater) smaller than the observed fluxes. The fluxes in either direction are even 4-5 times smaller than the observed fluxes. The effect of strong eddies on the northward temperature flux (15%) as well as on the southward freshwater flux (13%) is very similar to the observations (13% for both). However, due to strong northward moving cold/fresh eddies the effect of strong eddies on the southward temperature flux (46%) and the northward freshwater flux (46%) is higher than in the observations (25% and 19%, respectively). Overall, an average strong eddy in the model accounts for more than 5 times of the temperature and freshwater flux of an average regular eddy. The numbers for the direct comparison (same zonal extent for observations and model as well as same time period) as well as full extent and full time period are all listed in Table 4.1 and Table 4.2.

4.7 Characteristics of Eddies crossing 47°N

In chapter 3.4 I have already analyzed the cause for the large difference between regular and strong eddies with regard to surface temperature fluxes. For the surface temperature fluxes neither the differences in translation speed ($\mathbf{u}_E$), nor

the differences in eddy radius (R_E) are large enough to explain the anomalously high surface temperature flux of strong eddies. In the following, I will repeat the analysis for the volume flux by eddies in order to answer the following questions: Why is the flux of strong eddies about 4-5 times higher than the flux of regular eddies, and why is the flux of observed eddies in either direction about 4-5 times higher than the flux of simulated eddies?

Table 4.2: Number of eddies crossing 47°N and the respective properties. The variance shown in brackets represents the inner quartile range (i.e. the range of 50% of the values). The uncertainty of radius, translation speed are given as one standard deviation. The standard error of the mean value within a 90% confidence interval (given in parentheses) was calculated from bootstrapping the mean value with 1000 iterations. See text for the definition of strong eddies.

	Observations		**Model (ANHA4-SPG12)**	
period	Jan 1993 to Apr 2014	Jan 2002 to Dec 2013	Jan 2002 to Dec 2013	Jan 2002 to Dec 2013
zonal extent	43°W - 20.5°W	43°W - 20.5°W	43°W - 20.5°W	53°W - 10°W
total number of eddies	415	237	283	357
strong eddies	18 (4.3%)	13 (5.5%)	25 (8.8%)	25 (7.0%)
regular eddies	297	224	258	332
eddy radius [km]				
regular eddies	44.5 ± 11.1	44.7 ± 11.7	38.4 ± 9.4	37.7 ± 9.1
strong eddies	70.2 ± 13.4	71.1 ± 14.5	48.1 ± 12.8	48.1 ± 12.8
transl. speed [cm s^{-1}]				
regular eddies	20.4 ± 3.6	20.0 ± 4.2	5.2 ± 2.8	4.8 ± 2.8
strong eddies	21.4 ± 0.0	21.4 ± 0.0	10.1 ± 2.6	10.1 ± 2.6
vertical extent* [m]				
regular eddies	1330	1400	1150	1150
strong eddies	1180	1190	980	980
$\lvert HC\rvert$** [10^6Jm^{-3}]				
regular eddies $\lvert HC_r\rvert$	3.6, [1.8 5.2], (0.1)	3.3, [1.7 4.5], (0.2)	3.4, [1.2 4.5], (0.2)	2.8, [0.7 3.9], (0.2)
strong eddies $\lvert HC_s\rvert$	9.0, [6.7 11.3], (0.7)	9.2, [6.5 11.5], (0.9)	9.3, [6.9 11.7], (0.7)	9.3, [6.9 11.7], (0.7)
$\lvert FWC\rvert$** [10^{-3}m^{-3}]				
regular eddies $\lvert FWC_r\rvert$	2.6, [1.4 3.7], (0.1)	2.4, [1.3 3.3], (0.1)	2.4, [0.9 3.3], (0.2)	1.9, [0.5 2.9], (0.1)
strong eddies $\lvert FWC_s\rvert$	6.5, [5.3 8.1], (0.5)	6.6, [5.0 8.2], (0.6)	6.3, [4.9 7.7], (0.5)	6.3, [4.9 7.7], (0.5)

* median vertical extent, ** Heat content of eddies ($A\ c_p \int \rho T' dz$) and freshwater content of eddies ($A \int FW' dz$) are divided by the respective eddy's area A and vertical extent H_E in order to separate between geometrical and thermohaline properties

Composites of the temperature and freshwater fields related to strong and regular eddies crossing 47°N are shown in Figure 4.14 and Figure 4.15. The composites are constructed as described in chapter 4.5.2. The vertical structure of most types of eddies crossing 47°N is similar between observations and model simulation. All composites, except strong anticyclonic eddies, show an asymmetric behavior with more cold and fresh water in the western part of the composite sections. This is especially prominent for cyclonic eddies (Figure 4.14a/c/e/g, and Figure 4.15a/c/e/g). The composites for strong anticyclonic eddies on the other hand are much more symmetric. The warm and salty anomalies are sur-

rounded by a cold and fresh anomaly for both observations and ANHA4-SPG12 simulation (Figure 4.14b/d, and Figure 4.15b/d). The warm and salty anomalies related to observed eddies extend all the way to around 2000 m, while the anomalies of simulated eddies are confined to the upper 750 m. However, the anomaly of the observed composite below 1000 m is small ($\sim$0.5°C/$\sim -2.5^{-3}$) compared to the maximum anomaly at around 500 m depth ($\sim$3.5°C/$< -1^{-2}$). The vertical extent of the composite eddy (1/10 of the maximum temperature anomaly) therefore only reaches down to about 1200 m, which is again close to the vertical extent of the composite eddy from the model simulation ($\sim$750 m).

In addition to the eddy translation speed ($\mathbf{u}_E$) and radius (R_E), the respective vertical extent (H_E), the heat content ($HC = A\ c_p\ \int \rho T' dz$), and freshwater content ($FWC = A\ \int FW' dz$) of the eddies have been added to the list of parameters to be analyzed (Table 4.2). HC and FWC are divided by the respective eddy's area A and vertical extent H_E in order to separate between geometrical and thermohaline properties.

In the following the average values for all potential parameters are discussed with respect to their contribution to the difference between regular and strong eddies in both observations and the ANHA4-SPG12 simulation.

1. Heat and freshwater content (HC/FWC): The most striking observation when comparing the properties of regular and strong eddies from observations and the model simulation is the remarkable similarity for the thermohaline properties of the eddies. For the overlapping period HC ranges from 3.3×10^6Jm^{-3} to 3.4×10^6Jm^{-3} for regular and from 9.2×10^6Jm^{-3} to 9.3×10^6Jm^{-3} for strong eddies. Similarly, FWC is 2.4×10^{-3}m^{-3} for regular and between 6.3×10^{-3}m^{-3} and 6.6×10^{-3}m^{-3} for strong eddies (Table 4.2). In both cases, the ratio between strong and regular eddies ($\frac{HC_r}{HC_s}$ and $\frac{FWC_r}{FWC_s}$) is between 2.6 and 2.8. This agreement between observations and model results is remarkable and somewhat surprising. For both observations and model, the thermohaline properties are the main reason for the differences between strong and regular eddies.

2. Translation speed ($\mathbf{u}_E$): The translation speed of regular and strong eddies in the observations is practically the same and therefore definitely does not explain the large flux of strong eddies. In the model, strong eddies are almost twice as fast as regular eddies, which is the second largest contribution to the large flux by strong eddies in the model simulation.

Different translation speeds are also the main reason for the different magnitude of the fluxes between observations and model. On average eddies move 3.6 times faster in the observations than in the model simulation.

3. Eddy radius (R_E): The radius of strong eddies is larger than that of regular eddies for both observations (ratio 1.6) and model simulation (ratio 1.3), which explains a fraction of the large differences between regular and strong eddies. As expected, this result is very similar to the surface analysis in chapter 3.4.

   The difference in size also explains a fraction of the difference between observed and simulated eddies. On average, eddies in the observations are 1.2 times larger than eddies in the model simulation.

4. Eddy vertical extent (H_E): The vertical extent is actually shallower for strong eddies than for regular eddies in both observations and model simulation and therefore does not explain the large fluxes by strong eddies.

   Eddies are on average 1.2 times deeper in the observations than in the model, explaining a small fraction of the difference between observations and model simulation.

Overall it can be summed up that the thermohaline properties (i.e. the actual heat and freshwater content of the respective eddies) are the main reason for the large temperature and freshwater fluxes associated with strong eddies. This agrees well with the result for the surface fluxes that strong eddies are associated with a larger SST anomaly than regular eddies (chapter 3.4). The differences between the fluxes by eddies in the observations and the model simulation are linked primarily to the different translation speeds.

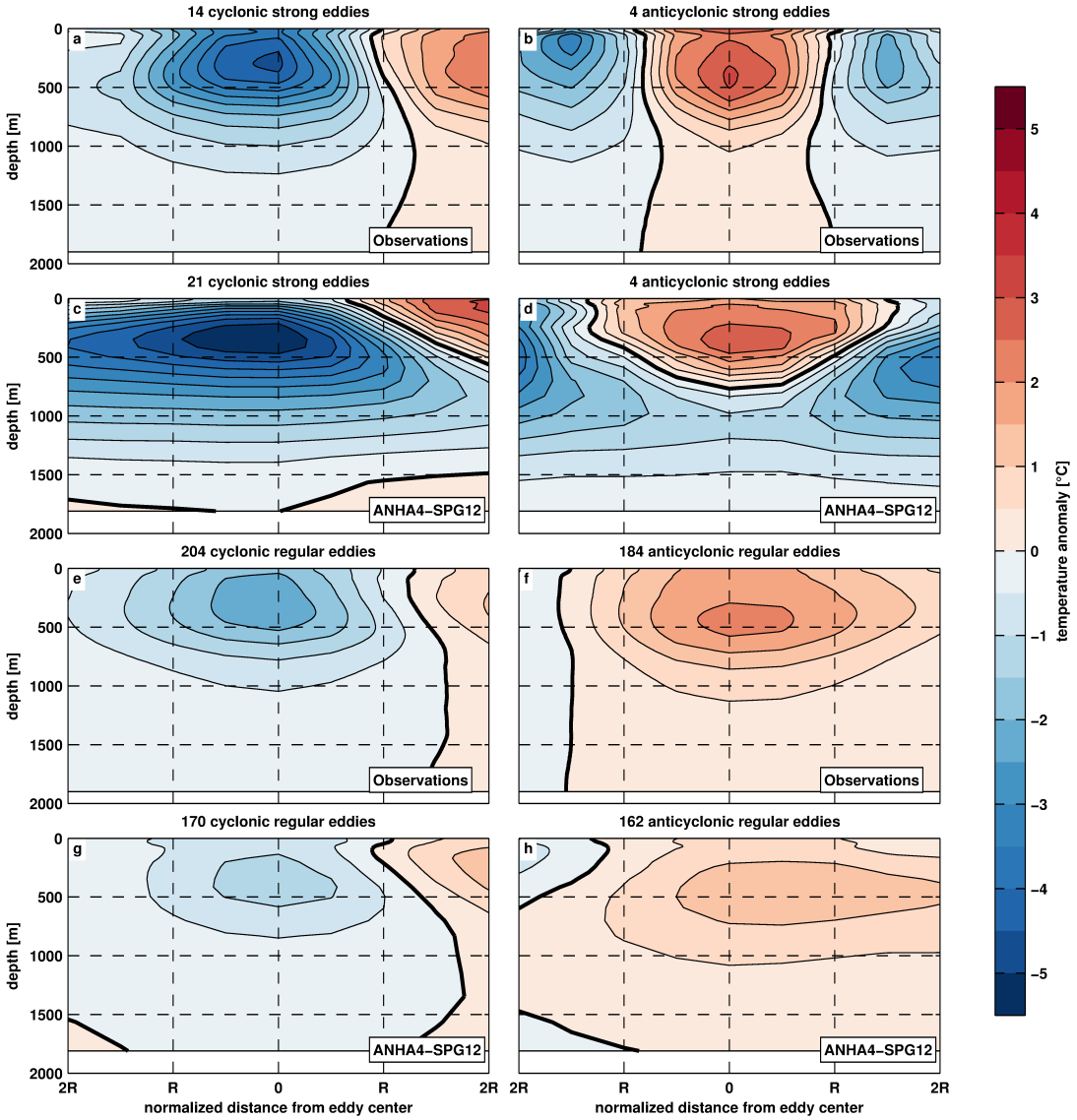

Figure 4.14: Composites of the temperature anomalies associated with eddies crossing 47°N in the observations (January 1993 to April 2014, a/b/e/f) and the 1/12° ANHA4-SPG12 simulation (January 2002 to December 2013, c/c/g/h). The x-axis is given in multiples of eddy-radii. The thick black line indicates the zero-line.

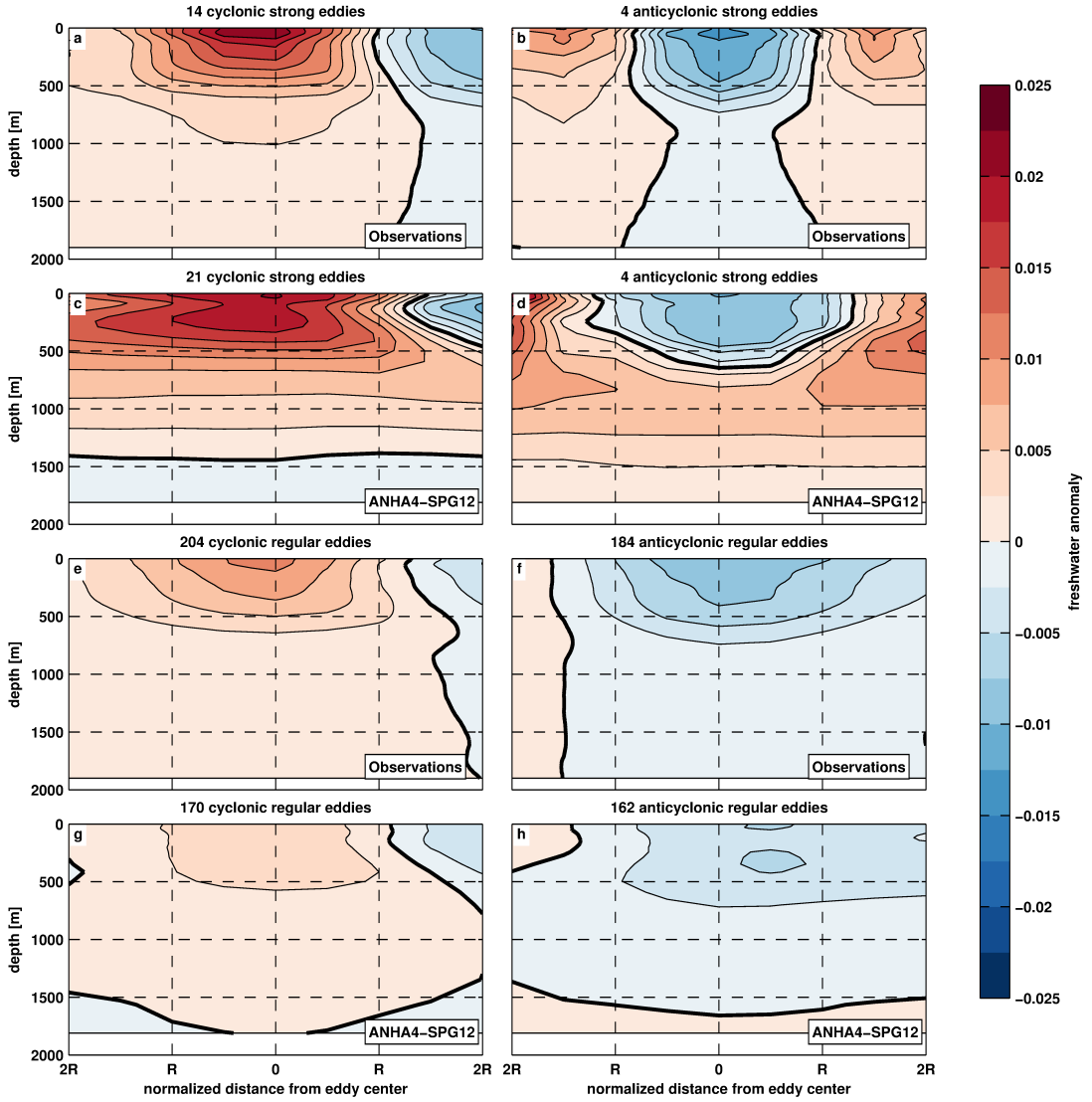

Figure 4.15: Composites of the freshwater anomalies associated with eddies crossing 47°N in the observations (January 1993 to April 2014, a/b/e/f) and the 1/12° ANHA4-SPG12 simulation (January 2002 to December 2013, c/d/g/h). The x-axis is given in multiples of eddy-radii. The thick black line indicates the zero-line.

4.8 Spatial Variability of Temperature and Freshwater Fluxes related to Eddies crossing 47°N

In chapter 3 the focus was on the surface temperature flux by eddies crossing 47°N and the pathways that eddies take when crossing the section. The analysis now will be similar, but focused on the volume fluxes across 47°N using temperature and freshwater data from the GEM method. Since I am analyzing the same

eddies as in chapter 3, I will not repeat the detailed analysis of the numbers of eddies in the different parts of the 47°N section (Figure 4.16b and Figure 4.17b). As in chapter 3, temperature and freshwater fluxes across the 47°N section are summed up in bins of 1° longitude to get a better view on the spatial distribution of the fluxes by eddies (Figure 4.16c/d and Figure 4.17c/d). The terminology is the same as for the surface fluxes: net flux (sum of all eddies), net regular flux (sum of only regular eddies) and a net strong flux (sum of only strong eddies). As before, the number of eddies and the flux are normalized with the length of the respective time series (21 years for the observations, 12 years for the model), to ensure comparability.

There were almost no eddies detected on the Grand Banks in the ANHA4-SPG12 simulation and there is no GEM data for regions shallower than 2000 m. The section analyzed here is therefore reduced to the deep part of the ocean, spanning from Flemish Cap (around 44.5°W) to 10°W. The eastern part of the East Atlantic is not covered by the GEM field, but there are eddies in the model simulation, so it is included in the section. The separation into subsections remains the same as in chapter 3, with one subsection in the western boundary region, one around the Mid-Atlantic Ridge (MAR), and one for the eastern basin.

Overall, observations and the ANHA4-SPG12 model simulation show very similar results for the pathways of eddies across the 47°N and the related fluxes of temperature and freshwater (Figure 4.16c/d and Figure 4.17c/d). Both show high fluxes in the western basin and very low values compared to that for the remaining section. Of course here I can only make statements about the part of the 47°N section covered by the GEM region, but since the surface temperature fluxes in the eastern basin were almost negligibly small, I am confident that the volume fluxes are too.

To compare the spatial distribution of eddies along 47°N and their respective fluxes across 47°N, the correlation of the binned values (number of eddies, temperature and freshwater fluxes) along the section is calculated between observations and model. The correlation for the numbers of eddies crossing the section is 0.9 (Here the number of eddies in one bin is simply the number of northward moving eddies minus the number of southward moving eddies). The correlation of the binned fluxes is a little lower with 0.8 for the net temperature fluxes and 0.7 for the net freshwater fluxes. These values show again how well the 1/12° model simulation reproduces the observed features along 47°N, even on scales as small as 1°.

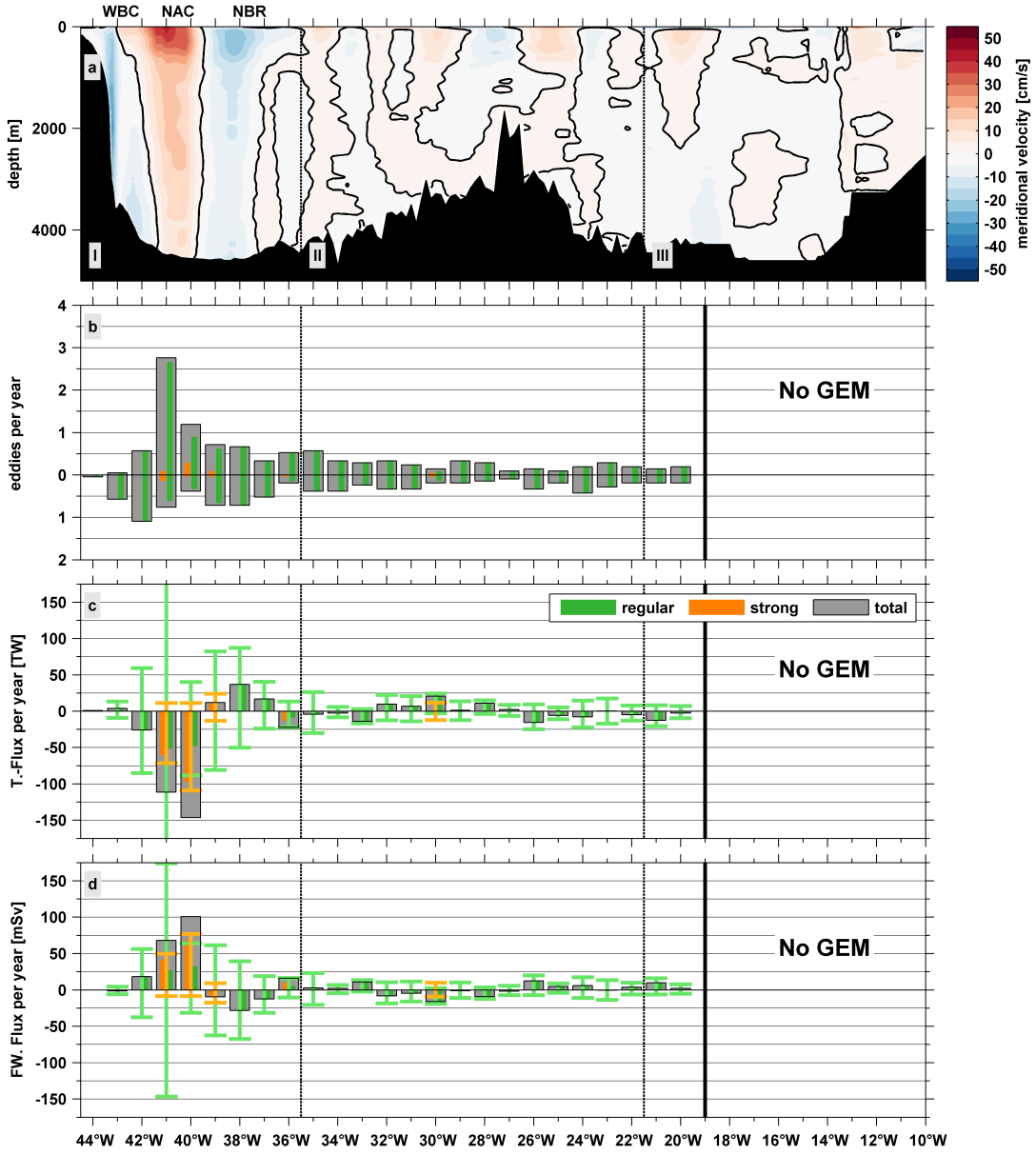

Figure 4.16: Meridional background velocity from shipboard observations (a), the number of northward and southward moving eddies from satellite observations (January 1993 to April 2014) per 1° bin crossing 47°N per year (b), and respectively the sum of the temperature (c) and freshwater fluxes (d) by eddies per 1° bin along 47°N (normalized by the number of years). Vertical bars show the sum of the fluxes of regular (green) and strong (orange) eddies in either direction. The vertical whiskers represent the standard deviation of the respective flux in either direction.

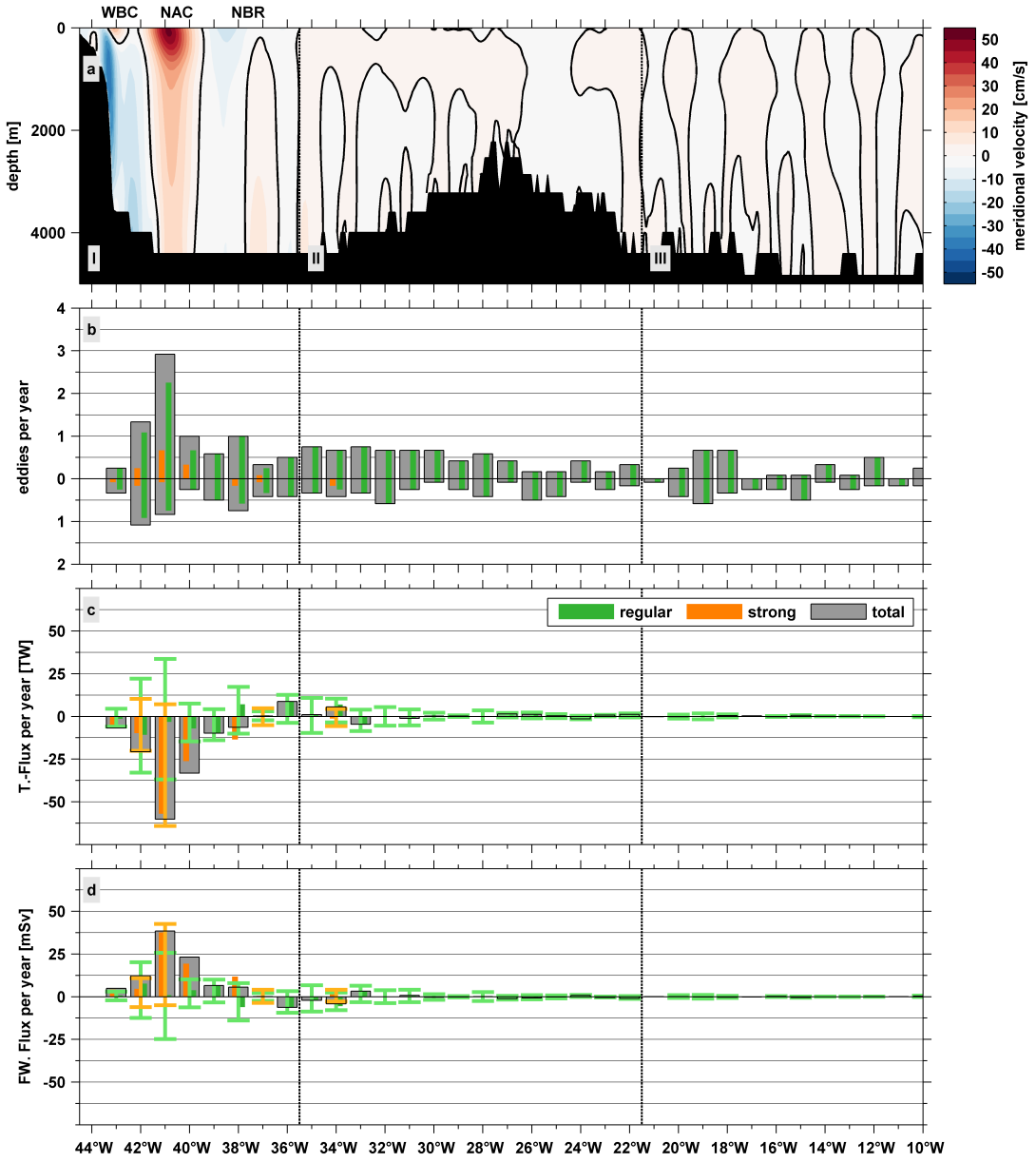

Figure 4.17: Meridional background velocity from the 1/12° ANHA4-SPG12 model simulation (a), the number of northward and southward moving eddies from the model (January 2002 to December 2013) per 1° bin crossing 47°N per year (b), and respectively the sum of the temperature (c) and freshwater fluxes (d) by eddies per 1° bin along 47°N (normalized by the number of years). Vertical bars show the sum of the fluxes of regular (green) and strong (orange) eddies in either direction. The vertical whiskers represent the standard deviation of the respective flux in either direction.

The volume fluxes in observations and model confirm the initial results from analyzing the surface fluxes that the western basin is the most important region when it comes to fluxes by individual eddies crossing 47°N. The western boundary subsection shows the most eddies, most strong eddies, and the highest variability of temperature and freshwater flux (Figure 4.16c/d and Figure 4.17c/d). The directions of the mean (averaged over the entire section) temperature flux (southward: -12.8 TW, -4.1 in the model) and mean freshwater flux (northward: 8.3 mSv, 2.6 mSv in the model) are determined here. In both observations and model simulation, strong eddies are mostly confined to the NAC with around 90% of all strong eddies crossing 47°N in this region.

Most striking are the three bins between 42°W and 40°W comprising the NAC. Most of the strong eddies found in the western boundary section actually cross 47°N in this small subsection. The small subsection of only 230 km extent (i.e. less than 1/10 of the full section) accounts for roughly half (48-50% in the observations and 53-56% in the model simulation) of the absolute temperature and freshwater flux across 47°N ($\sum_i |F_{Ti}|$ and $\sum_i |F_{FWi}|$, respectively). These large fluxes are also accompanied by the highest variability along the section, as expressed by the whiskers in Figure 4.16c/d and Figure 4.17c/d. As for the surface temperature flux, the extremely large fluxes (largest temperature and freshwater fluxes of the whole 47°N section) are caused by cold and fresh eddies moving northward with the NAC. One might assume that - apart from the sheer number of eddies in the western basin - the high background velocity in the NAC is a cause for the large fluxes, since the eddies move northward with the NAC. However, this is not the case. On average the eddies in the western boundary region move just as fast as anywhere else along the section.

The other bins of the western boundary section show much lower fluxes than the three discussed above in observations and model simulation. The net flux in the WBC is very small compared to the analysis of surface temperature fluxes, which could be partially due to the fact that the GEM region ends where the water depth is shallower than 2000 m. In the three bins to the east of the NAC, in the Newfoundland Basin Recirculation (NBR), the fluxes by eddies observed from satellite observations reverse the sign compared to the NAC region (Figure 4.16c/d). The strongest northward temperature flux (and southward freshwater flux) coincide with the location of the core of southward velocity of the NBR (Figure 4.16a). This finding is confined to the observations though and not backed by the model results. In the model, the NBR is generally weaker and the core is located exactly between two 1° bins (Figure 4.16a). While there is no net

northward temperature flux (and southward freshwater flux) in the model related to the NBR, the bin at 38°W does show a higher variability than the adjacent bins (Figure 4.16c/d).

As for the surface temperature fluxes by eddies described in chapter 3.5, the other subsections play only a minor role for the temperature and freshwater fluxes by eddies across 47°N. In both observations and the ANHA4-SPG12 simulation, the net fluxes and also the variability are much lower there than in the western boundary region (Figure 4.16c/d and Figure 4.17c/d). The mid section, comprising the MAR, accounts for 21-24% of the respective absolute temperature and freshwater fluxes by eddies.

The eastern basin is not covered by the GEM field, but it has the least contribution to the flux across 47°N in the model simulation. While around 21% of all eddies detected in the model simulation cross 47°N in the eastern basin, these eddies carry almost no temperature/freshwater flux. The eastern subsection accounts for only around 2% of the absolute fluxes of temperature and freshwater. It is therefore safe to assume, that there is no substantial loss to the overall flux across 47°N by not including the eastern basin and that the results from the GEM method are representative for the whole 47°N section.

4.9 Fluxes by Individual Eddies Compared to the Turbulent Component of the Flow Field

One of the questions raised in the introduction was: How much of the total heat and freshwater flux across 47°N can actually be explained by anomalies carried by eddies? And how much of the high frequency (i.e. "eddy component") of the flux can be explained by said anomalies?

The calculation of the heat and freshwater fluxes across 47°N is straight forward in the model environment. The meridional heat flux is simply

$$F_T = c_{p_0}\ \rho_0 \int\int v\ T dx dz,$$

and the freshwater flux

$$F_{FW} = \int\int v\ FW dx dz,$$

where $c_{p_0} = 4200$ J kg^{-1} K^{-1} an average specific temperature capacity for sea water, $\rho_0 = 1025$ kg m^{-3} an average sea water density, v is the meridional velocity. The full fluxes F_T and F_{FW} are then separated into a "mean component" and

a "high frequency component" (in the form $x = \overline{x} + x'$). For the analysis here, I define the mean component as everything related to the mean annual cycle. This is consistent with the definition of the surface temperature fluxes by eddies in chapter 3.1. The mean components of the fluxes are $\overline{F_T} = c_{p_0}\ \rho\ \int \overline{v}\ \overline{T} dxdz$, and $\overline{F_{FW}} = \int \overline{v}\ \overline{FW} dxdz$, where $\overline{v}$, $\overline{T}$, and $\overline{FW}$ are the mean annual cycle of the meridional velocity, the temperature and the freshwater field, respectively. The high frequency components are then simply $F'_T = F_T - \overline{F_T}$, and $F'_{FW} = F_{FW} - \overline{F_{FW}}$ (Figure 4.18). This means that the high frequency component of the fluxes include not only eddies, but all variability on intraseasonal scales, like meandering of the major currents, shifts of the temperature front in the Newfoundland Basin, major cooling or warming, and especially the Ekman layer transport. The high frequency component of the respective fluxes will therefore always be larger than the fluxes by individual eddies.

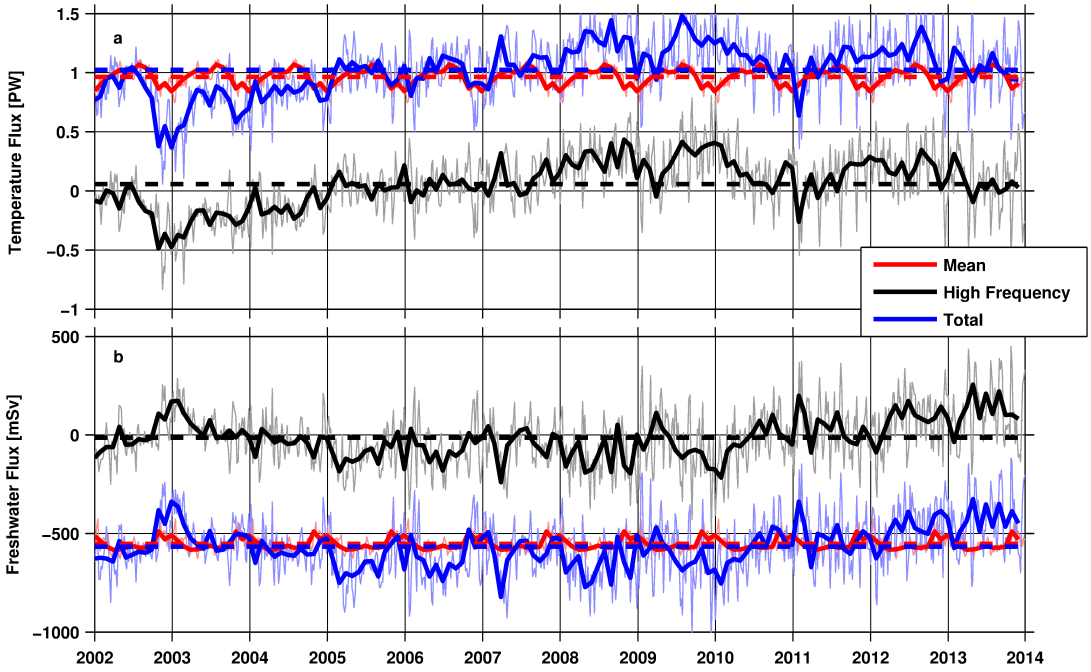

Figure 4.18: Basin wide meridional heat fluxes (a) and freshwater fluxes (b) across 47°N in the 1/12° ANHA4-SPG12 model simulation between January 2002 and December 2013. For both fluxes the monthly mean values (thick lines) and the 5-day model output (thin lines) of the total flux (blue), the mean flux (red) and the high frequency flux (black) are shown. The respective average values are indicated by dashed lines.

The average heat flux across 47°N in the ANHA4-SPG12 model is 1.0 ± 0.26 (one standard deviation) PW, which is high compared to previous observations. The high frequency component of that flux is 0.06 ± 0.25 PW. For the freshwater flux, the picture is similar with an average flux of -570 ± 150 mSv of which

-10 ± 140 can be explained by the high frequency component. For both cases the high frequency component dominates the variability of the flux, while the strength of the flux is defined by the mean component (Figure 4.18).

The mean temperature and freshwater fluxes carried by individual eddies (Table 4.1) are directed in the opposite direction of the average fluxes shown in Figure 4.18, but they are negligibly small compared to the average fluxes. The mean temperature flux by individual eddies in the model is -4.1 TW (i.e. -0.004 PW) and the respective mean freshwater flux 2.6 mSv (Table 4.1). The fluxes carried by individual eddies thus range in the order of only $\mathcal{O}(1/200)$ of the average fluxes. However, the variability of the fluxes by individual eddies is higher ($\pm$0.03 PW and $\pm$19 mSv), explaining 10%-13% of the overall variability.

While the effect on the average flux is very small, individual eddies do have an effect on the high frequency components and reduce them since the fluxes by individual eddies are directed opposite to the high frequency fluxes. The high frequency temperature flux is reduced by 7% through temperature fluxes by individual eddies and the high frequency component of the freshwater flux is reduced by even 19%.

For the observations this analysis is not possible since there is not enough data available for the calculation of heat flux time series. I therefore have to refer to numbers provided by other studies. Ganachaud and Wunsch (2003, observational study) and Rhein et al. (2011, model study) have quantified the heat flux at 47°N to about 0.6 PW with a standard deviation in the order of 0.1 - 0.2 PW. Rhein et al. (2011) showed that - at least in their model - the high frequency component makes up around 60% of the variability ($\sim$ 0.1 PW) while the mean high frequency flux is negligible (0.01 PW). The observed fluxes by individual eddies fall very well into this range. The mean temperature flux by eddies is negative (-0.01 PW) but negligibly small compared to the mean flux. The standard deviation ($\pm$0.1 PW) is the same as in the study by Rhein et al. (2011), explaining most of the observed variability.

Unlike for example Agulhas Rings or NBC Rings, fluxes by individual eddies crossing 47°N are negligible compared to the average fluxes across 47°N and even small compared to the high frequency component of the respective fluxes. They do however have a notable influence on the variability of the average fluxes. Fluxes of individual eddies account for around 60% of the overall variability in the observation and around 10%-15% in the ANHA4-SPG12 model simulation.

4.10 Summary

Other studies have focused on the properties and fluxes caused by eddies using data from Argo floats (e.g., Dong et al., 2014; Zhang et al., 2014; Sun et al., 2017), but their approach only allows the analysis of the composite of eddies within 5°×5° boxes. As shown in chapter 4.4, there are only a total of 65 eddies (16 cyclones and 49 anticyclones) in the GEM region, which are sampled by Argo profiles both inside the eddy and in the immediate surroundings of the eddy. It is therefore not (yet) possible to assign temperature and freshwater fluxes to individual eddies using only data from Argo floats.

Using a combination of 21 years of geostrophic velocities from satellite altimetry, temperature and salinity data constructed from surface parameters using the Gravest Empirical Mode (GEM) method, ship-based velocity measurements, as well as a high resolution (1/12°) simulation with the NEMO ocean model spanning a period of 12 years I have found:

- Despite the limitations at 47°N, the GEM method is a suitable technique to infer temperature and freshwater fluxes by individual eddies from sea surface height (Figure 4.6 and Figure 4.7).
- In both observations and ANHA4-SPG12 model simulation so-called strong eddies have an almost 3 times higher heat content and freshwater content than so-called regular eddies (Figure 4.14, Figure 4.15 and Table 4.2).
- About 15% - 20% of the observed absolute temperature and freshwater fluxes by eddies across 47°N stem from strong eddies. In the ANHA4-SPG12 model around one third of the respective fluxes stem from strong eddies (Figure 4.12 and Table 4.1).
- The western part of the Newfoundland Basin with the fastest and most pronounced current branches (WBC, NAC, and NBR) is the major pathway for eddies and their associated temperature and freshwater fluxes across 47°N (Figure 4.16 and 4.17).
- Northward moving cold and fresh cyclones carrying subpolar water from the WBC make a considerable contribution to the overall temperature and freshwater fluxes by eddies (Figure 5.1).
- The eastern basin of the North Atlantic at 47°N has only a small contribution to the meridional temperature and freshwater fluxes carried by eddies (Figure 4.12 and Table 4.1).

- The spatial patterns of the number of eddies crossing 47°N, as well as the patterns of the temperature and the freshwater fluxes carried by those eddies across 47°N are consistent between the observations and the ANHA4-SPG12 model simulation (correlations between 0.7 and 0.9, Figure 4.16 and Figure 4.17).

- The contribution of eddies to the average temperature and freshwater fluxes across 47°N is negligible ($F_{T\,eddy} << F_T$,$F_{T\,eddy} << \overline{F_T}$,$F_{T\,Eddy} < F'_T$). However eddies account for a large part of the temporal variability of the fluxes.

In the following chapter I will discuss the results in relation with the surface fluxes from chapter 3 and with other studies.

5 Discussion and Outlook

Overall, the results from the analysis of the volume fluxes by eddies crossing 47°N are in agreement with the results from the surface fluxes in chapter 3. The following table gives an overview of the different analyses carried out in chapter 3 and chapter 4 and the respective main results.

Table 5.1: Overview of the results of the different methods used in this thesis. The ✓ indicates that the result is confirmed by the respective method, the X indicates that the result is not confirmed.

Result	**Surface**			**Volume**	
	Observations (1/4°)	ANHA4 (1/4°)	ANHA4-SPG12 (1/12°)	GEM (1/4°)	ANHA4-SPG12 (1/12°)
large fraction of absolute fluxes by strong eddies	✓	✓	✓	✓	✓
difference between regular and strong due to thermohaline properties	✓	✓	✓	✓	✓
pathways of eddies related to main current branches	✓	✓	✓	✓	✓
large contribution by cold/fresh cyclones	✓	X	✓	✓	✓
southward temperature flux in the NAC region	✓	X	✓	✓	✓
northward freshwater flux in the NAC region	N/A	N/A	N/A	✓	✓
overall net southward temperature flux	X	X	✓	✓	✓
overall northward freshwater flux	N/A	N/A	N/A	✓	✓
fluxes in eastern basin negligible	✓	✓	✓	N/A	✓

One result found in every analysis, no matter if observed or simulated eddies, is the considerable effect of so-called strong eddies. Strong eddies were defined as all eddies whose temperature flux exceeds two times the standard deviation of the flux of all eddies (Chapter 3.4). One might argue that this definition is self fulfilling, i.e. a strong eddy is defined as having a large temperature flux, hence

it is obvious that the flux by strong eddies is anomalously large. While this is of course true, it does not explain the magnitude of the flux by strong eddies. I will therefore consider a simple Gaussian distributed data set with zero mean (which is practically the case for the fluxes by eddies across 47°N). Around 5% of this distribution exceed two times of its standard deviation, i.e. will be defined as strong values. These strong values would account for around 14% of the total flux. However, in the analysis of the fluxes by eddies, the 5% strong eddies carry around 25% of the surface temperature flux, 15%-20% of the observed volume fluxes, and around 34% of the simulated volume fluxes. This means that the distribution of the fluxes by eddies is not simply Gaussian shaped. The extreme values on the tails of the distribution play a considerable role for the overall averaged fluxes by eddies, which is why I used the inner quartile approach instead of a simple standard deviation in order to represent the temporal variability.

Despite these similarities, there are also some striking differences between the time series of the surface fluxes and the volume fluxes (Figure 3.4 and Figure 4.12). While some eddies can be clearly distinguished in both time series, the magnitudes of the respective fluxes differ substantially in most cases. For example the cold southward moving eddy in the winter of 2009/10 shows the largest surface temperature flux of the whole period (Figure 3.4), but the respective volume flux barely exceeds two standard deviations of the time series (Figure 4.12).

I have shown in chapter 3.4 and chapter 4.7 that strong eddies are a result of the thermohaline properties of the respective eddies (SST for surface fluxes, heat content and freshwater content for volume fluxes). However, the large anomalies related to strong eddies might simply be an artifact caused by a major warming or cooling, or a displacement of the temperature front in the Newfoundland Basin. The different approaches for calculating the anomalies used to compute the surface fluxes (relative to the mean annual cycle) and volume fluxes (relative to the surrounding water) show that this is not the case. The fact that the results are so similar - despite using different methods - proves that strong eddies are not simply an artifact caused by the choice of the background state. They are in fact caused almost solely by their thermohaline properties. Strong eddies occur almost exclusively in the western basin, because here the temperature and freshwater gradients between WBC and NAC are strong. An eddy formed in the WBC and then dragged into the NAC will therefore have a large temperature/freshwater anomaly, no matter if this anomaly is calculated with respect to the mean annual cycle of the NAC water or with respect to the properties of the water surrounding the eddy.

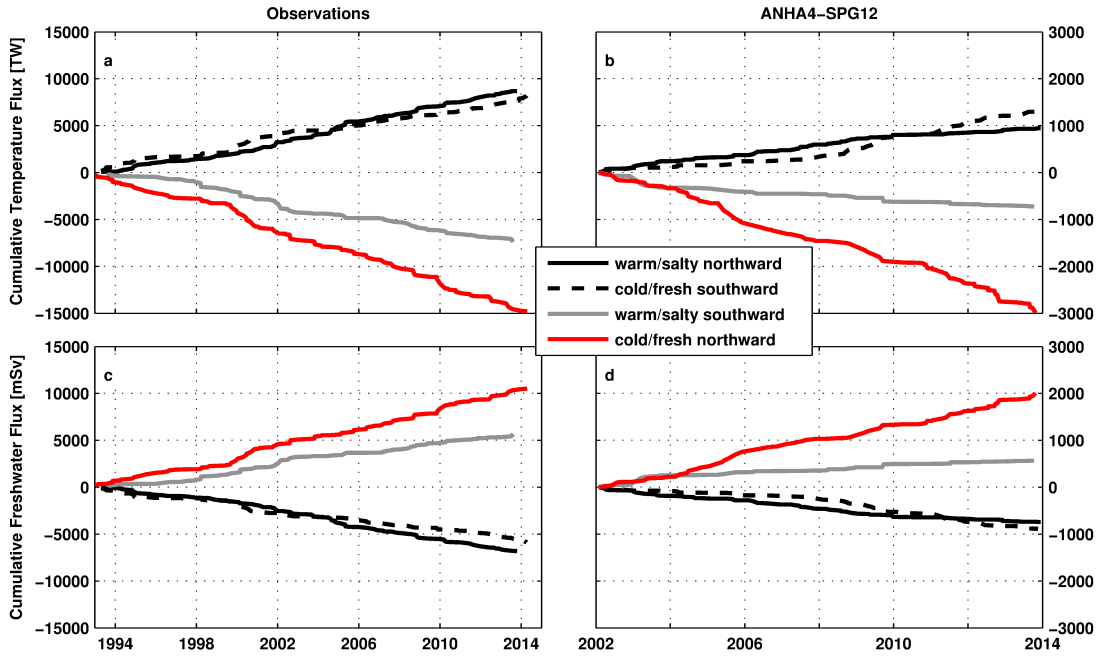

Figure 5.1: Cumulative sum of the temperature (a/b) and freshwater (c/d) fluxes by eddies for the four major types of eddies for the observations (left) and the 1/12°ANHA4-SPG12 model simulation (right). The four major eddy types make up 98% of all eddies in the observations and 99% of all eddies in the model simulation. Note the different length of the time series for observations and model as well as the different scales on the Y-axis.

One major finding, in both chapter 3 and chapter 4, is the considerable contribution of northward moving cold and fresh cyclones to the overall flux by eddies. Two types of eddies account for a northward temperature and a southward freshwater flux (warm and salty northward, and cold and fresh southward), and two types of eddies account for a southward temperature and a northward freshwater flux (cold and fresh northward, and warm and salty southward). The exceptional role of northward moving cold and fresh eddies becomes obvious when comparing the cumulative sums of the four major different types (Figure 5.1). For both observations and ANHA4-SPG12 model simulation, the cumulative flux of these eddies stands out and exceeds all other types (red lines in Figure 5.1). The other three types are associated with fluxes of approximately the same magnitude (apart from opposing signs of course). Comparing the slopes of the lines shows that the cumulative flux of observed cold and fresh eddies is between 1.4 and 2.0 (average: 1.7) times higher than that of other eddies. For the ANHA4-SPG12 model simulation the effect is even stronger and the cumulative flux of cold and fresh eddies is between 2.1 and 4.5 (average: 3.0) times higher than that of other eddies. This has two reasons: (1) There are simply more northward moving cold and fresh ed-

dies than other eddies. Between 30% (observations) and 32% (ANHA4-SPG12) of all eddies are northward moving cold and fresh eddies. (2) Northward moving cold and fresh eddies have a 1.3 (observations) to 1.5 (ANHA4-SPG12) larger cold anomaly and higher freshwater content than southward moving cold and fresh eddies. For warm and salty eddies there is practically no difference between northward and southward moving eddies for heat and freshwater content.

Figure 5.1 also clearly shows the different magnitude of the fluxes in the observations and the ANHA4-SPG12 model simulation. The fluxes in the model simulation are lower than the observed fluxes. When taking into account only the overlap region (43°W - 20.5°W) and period (January 2002 - December 2013), the average absolute fluxes by eddies ($\overline{|F_T|}$ and $\overline{|F_{FW}|}$) are by a factor of 4.5 (temperature flux) and 4.8 (freshwater flux) smaller in the model than the observed fluxes (Table 4.1, middle columns).

This factor can be separated into the different components of the fluxes following equation 4.1 and equation 4.2, namely the eddy radius R_E, the eddy translation speed v_E, the vertical extent of the eddy H_E and the respective heat content HC and freshwater content FWC of the eddy.

Table 5.2: Different factors explaining the difference between temperature and freshwater fluxes by eddies in observations and ANHA4-SPG12 simulation.

radius	$\overline{R_{Eobs}}/\overline{R_{Emodel}}$	1.2
translation speed	$\overline{\|v_{Eobs}\|}/\overline{\|v_{Emodel}\|}$	3.6
vertical extent	$\overline{H_{Eobs}}/\overline{H_{Emodel}}$	1.1
heat content	$\overline{\|HC_{obs}\|}/\overline{\|HC_{model}\|}$ [1]	0.9
freshwater content	$\overline{\|FWC_{obs}\|}/\overline{\|FWC_{model}\|}$ [1]	1.0
temperature flux	$\overline{\|F_{Tobs}\|}/\overline{\|F_{Tmodel}\|}$	4.5
freshwater flux	$\overline{\|F_{FWobs}\|}/\overline{\|F_{FWmodel}\|}$	4.8

[1] The heat content ($A\ c_p \int \rho T' dz$) and freshwater content ($A \int FW' dz$) of the eddy are divided by the respective eddy's area A and depth H_E in order to separate between geometrical and thermohaline properties

The separation into different components shows that the differences in the magnitudes of the temperature and freshwater fluxes between observations and ANHA4-SPG12 model simulation are almost solely caused by the different translation speeds of the eddies crossing 47°N (Table 5.2).

The same can also be found for the surface temperature fluxes by eddies crossing 47°N. There are some minor differences between volume fluxes and surface fluxes, because part of the section along 47°N is not covered by the GEM region. However, the main finding is the same. For both ANHA4 and ANHA4-SPG12 simulation, the main reason for the difference in surface temperature flux between

observations and model is the different translation speeds of the eddies crossing 47°N (Table 5.3).

Table 5.3: Different factors explaining the difference between surface temperature fluxes by eddies in observations, ANHA4 simulation and ANHA4-SPG12 simulation.

		ANHA4	ANHA4-SPG12
radius	$\overline{R_{Eobs}}/\overline{R_{Emodel}}$	1.1	1.1
translation speed	$\overline{\lvert v_{Eobs}\rvert}/\overline{\lvert v_{Emodel}\rvert}$	3.7	3.9
SST	$\overline{\lvert SST_{obs}\rvert}/\overline{\lvert SST_{model}\rvert}$	1.2	0.8
temperature flux	$\overline{\lvert F_{Tobs}\rvert}/\overline{\lvert F_{Tmodel}\rvert}$	5.1	3.1

A likely explanation for this phenomenon is the different temporal and spatial resolution of the observation (1 day, 1/6° refined from 1/4°) and the output of the model (5 days, 1/12°). The temperature and freshwater fluxes across 47°N are calculated using the eddy translation speed at the instant of the eddy crossing the section. Due to the discrete spatial and temporal resolution, the minimum possible velocity of an observed eddy is 1/6° in 1 day, i.e. 21.4 cm/s. There are some exceptions due to the post-processing of the eddy tracks, described in chapter 2.4. This sometimes leads to longer gaps between the positions of eddies and therefore lower velocities (e.g. 1/6° in 3 days). However, this is only the case for $\sim 10\%$ of the observed eddies crossing 47°N, while $\sim 90\%$ travel exactly one grid cell in one day when crossing the section.

The minimum possible translation velocity in the ANHA4-SPG12 model simulation is 1/12° in 5 days, i.e. 2.1 cm/s, allowing for a much wider range of possible meridional velocities. This is reflected in the averages of the velocities of eddies crossing 47°N and their respective standard deviations (Table 4.2). The average meridional velocity (without regard of the sign) of observed eddies crossing the section is 20.5 ± 3.5 cm/s (one standard deviation). This is equivalent to a relative variability of only 17%. For the model simulation, the average is 5.1 ± 3.1 cm/s, i.e. a relative variability of 60%.

This suggests that the meridional eddy translation velocities are likely to be somewhat overestimated in the observations. At the same time, they might be somewhat underestimated in the model simulation, due to the "filtering" by using 5 daily outputs. Using a 5 day (± 2 day) moving average on the observed velocities reduces them to 5.0 ± 3.1 cm/s, which is remarkably similar to the velocities in the ANHA4-SPG12 model simulation. Nonetheless, this does not represent the actual observed movement of the eddy on the refined 1/6° grid. I therefore prefer

not to smooth the observed eddy translation velocities, but it is important to keep in mind that the given spatial and temporal resolution can lead to over- or underestimation of the respective eddy translation velocities. This problem has not been discussed in any of the previous studies using the same detection algorithm as this thesis and dealing with the properties of detected eddies and their respective fluxes (e.g., Liu et al., 2012; Dong et al., 2014; Zhang et al., 2014).

Another important point concerns the travel distance of eddies and the question whether the effects of temperature and freshwater fluxes by eddies across 47°N are mostly local or also notable on larger regional scales. In other regions of the world, large coherent eddies can carry water for very long distances (e.g. Agulhas Rings or North Brazil Current Rings), playing a crucial role for the large scale distribution of water masses. However, eddies crossing 47°N are smaller and the average travel distance of eddies after crossing 47°N is around 80 km, with about 1/3 of all eddies traveling further than 100 km and individual eddies traveling up to 300 km. The effect of temperature and freshwater fluxes by eddies crossing 47°N is therefore much more locally confined, than for example the freshwater flux by North Brazil Current Rings. Nonetheless, the local effects of eddies crossing 47°N are far from negligible. As already discussed in chapter 4.9, eddies play a considerable role for the local variability of the temperature and freshwater fluxes across 47°N.

Aside from that, eddies provide a means of transport between WBC and NAC. Pérez-Brunius et al. (2004) used historical hydrographic data in combination with float data from the area and found that the heat loss of the NAC in the western subpolar North Atlantic is caused mostly by horizontal cross-frontal exchange induced by the eddy field. They suggest that steep meanders of the NAC are the main reason for this exchange. The heat loss by horizontal exchange is ten times greater than the vertical heat loss to the atmosphere and the largest loss occurs around 47°N in the Newfoundland Basin (Pérez-Brunius et al., 2004, , their Figure 9).

Saenko (2015) found similar results using a 1/12° configuration of the NEMO model (Madec and the NEMO team, 2008). His results suggest that the convergence of heat brought into the Newfoundland Basin with the mean flow of the NAC is 2-3 times larger than the heat loss to the atmosphere. The excessive heat is compensated by a strong cooling effect due to lateral high frequency heat fluxes.

Bower et al. (2009) tracked RAFOS floats released in the WBC around 50°N and found that the majority of floats leave the WBC somewhere between Flemish

Cap at 47°N and the Tail of the Grand Banks around 42°N. Their main conclusion was that there are turbulent interior pathways transporting Labrador Sea Water from the north into the subtropics that might even be more important than the transport by the WBC (Bower et al., 2009). However, this hypothesis was later rejected by Rhein et al. (2015). At the same time, the results by Bower et al. (2009) show that cold water detaching with eddies from the WBC (suggested by the spiraling of the float trajectories) sometimes remains in the NAC pathway (Bower et al., 2009, , their Figure 1b and Figure 2b), which agrees well with the findings by Pérez-Brunius et al. (2004) and Saenko (2015).

The cold and fresh eddies that were detected in the western basin can give a possible explanation for both of these phenomena. Northward moving cold and fresh eddies explain why there is such a large heat loss in this area, while southward moving cold and fresh eddies feed into the interior southward pathway of subpolar water. On average there are 3 cold and fresh eddies per year moving northward with the NAC in the narrow band between 40°W and 42°W (Figure 4.16 and Figure 4.17). Their average temperature fluxes are -0.17 ± 0.10 PW for the observations and -0.06 ± 0.03 PW for the ANHA4-SPG12 model simulation. These cold and fresh eddies modify the warm and salty NAC water by mixing it with cold and fresh subpolar water when the eddies decay. The temperature flux by cold and fresh eddies agrees well with the heat loss -0.12 ± 0.05 PW observed by Pérez-Brunius et al. (2004) around Flemish Cap. However, I disagree with the statement by Pérez-Brunius et al. (2004) that the heat loss is mainly due to steep meanders of the NAC. Cold and fresh eddies detaching from the WBC act as an additional source for the cooling of the NAC around Flemish Cap. Also the increased atmosphere-ocean interaction over mesoscale eddies (e.g., Ma et al., 2016) is likely to play a role for the strong heat loss in the Newfoundland Basin.

However, there are not only cold and fresh eddies moving northward with the NAC, but also eddies that are formed in the WBC and then move southward across 47°N. In the western basin section between Flemish Cap (44°W) and the flank of the MAR (36°W), an average of 2.5 cold and fresh eddies per year were found carrying subpolar water southward across 47°N. Most of these eddies are found either in the western part of the section, moving southward along the boundary between WBC and NAC, or east of the NAC, moving southward with the Newfoundland Basin Recirculation (Figure 4.16 and Figure 4.17).

Bower et al. (2009) found that only around 20% of the observed RAFOS floats detach from the WBC north of 47°N, while up to 85% of the floats leave the WBC before reaching the Tail of the Grand Banks at 42°N. Bower et al. (2013) tracked

three cold and fresh eddies that were formed in the WBC at the southern tip of the Grand Banks. However, these southward moving eddies will never cross 47°N and are therefore not captured by my analysis. This means that the 2.5 cold and fresh eddies per year moving southward across 47°N are only a small fraction of all eddies detaching from the WBC and feeding the southward interior pathways of subpolar water towards the subtropics.

In my analysis, more than 50 eddies per year are first detected along the slope of the Grand Banks (Figure 3.1c). Since eddies are sometimes lost by the algorithm and then detected again, this number must be higher than the actual number of eddies formed. Assuming that around half of the eddies move southward (which is the case for eddies crossing 47°N, chapter 3.4), a reasonable estimate for the number of cold and fresh eddies detaching from the WBC and feeding the southward pathway is in the order of 10 per year. This agrees well with the findings by Bower et al. (2009) that the number of floats leaving the WBC between 47°N and the southern tip of the Grand Banks is 4 times higher than the number of floats detaching from the WBC north of 47°N.

Also the recent study by Mertens et al. (2014) on the local circulation and transport in the Newfoundland Basin supports the findings of this thesis. Mertens et al. (2014) showed that around 2/3 (80 Sv) of the total NAC transport crossing 47°N (110 Sv) are recirculated locally in the Newfoundland Basin. At the same time about 1/2 (15 Sv) of the deep southward WBC transport ($\sigma_\Theta > 27.68$ kg m^{-3}) detach from the boundary current, partially contributing to the deep part of the northward NAC transport, and partially leaving the Newfoundland Basin through other pathways.

As mentioned in chapter 3.6, the eddy detection algorithm used in this thesis was designed to be a reliable tool for distinguishing between meanders and eddies (Nencioli et al., 2010). However, the trajectories of eddies, especially in the Newfoundland Basin, are rather short. The new *Mesoscale Eddy Trajectory Atlas product* from AVISO (short: META, SSALTO/Duacs, 2017) allows to compare the detected eddy trajectories with an independent data set. This data set of eddy trajectories was developed and validated in collaboration with D. Chelton and M. Schlax at Oregon State University (Chelton et al., 2011; Schlax and Chelton, 2016). The eddies are detected from satellite altimetry using an algorithm that is based on finding extrema of the sea level anomaly field (Schlax and Chelton, 2016). At this time META is an experimental product, but it could turn out to become a new standard data set for eddies detected from satellite altimetry.

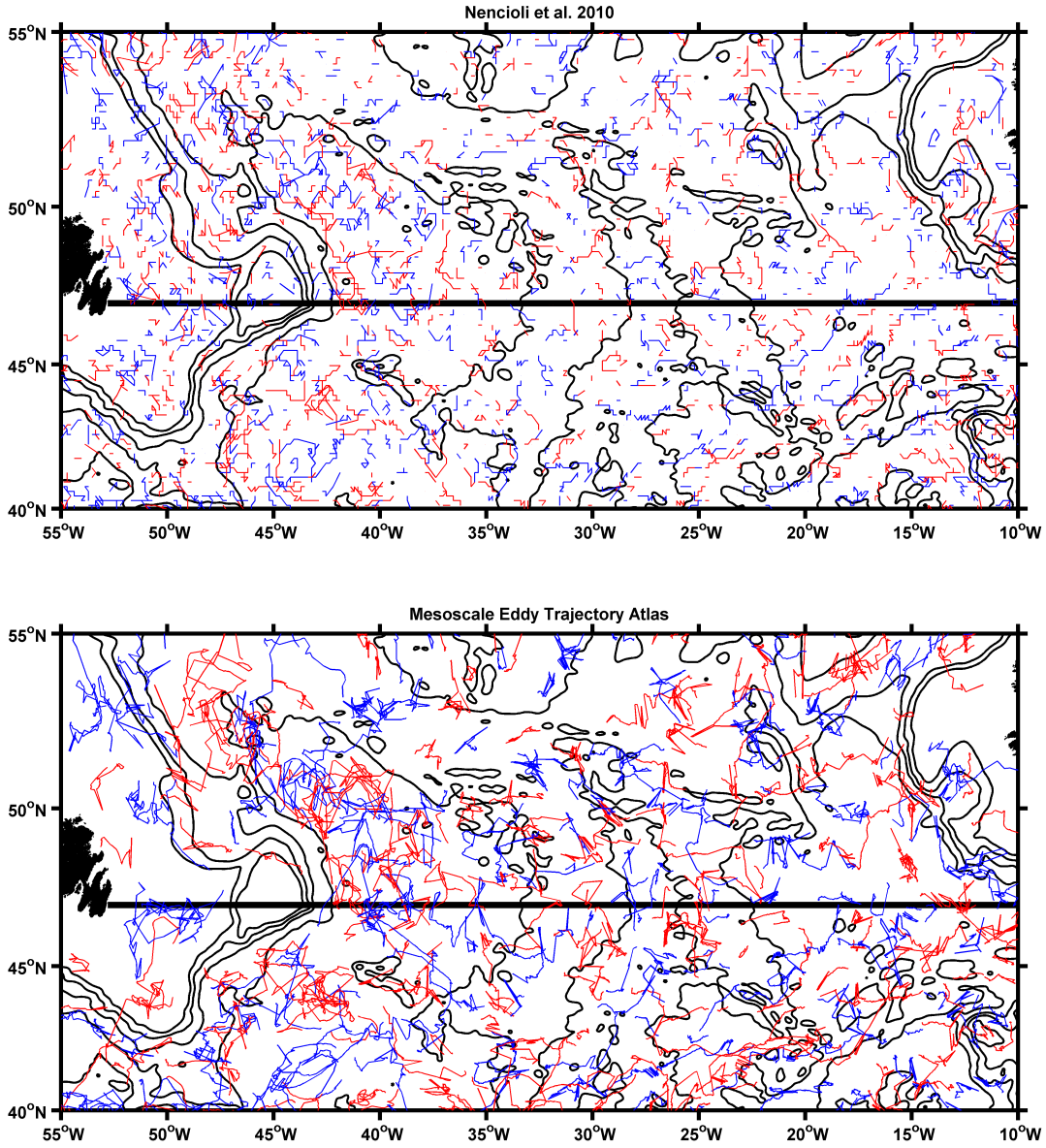

Figure 5.2: Example of eddy trajectories for the year 2000 from the vector geometry based algorithm by Nencioli et al. (2010) (a) and from the *Mesoscale Eddy Trajectory Atlas product* (Schlax and Chelton, 2016) (b). Cyclonic eddies are indicated with red lines, anticyclonic eddies with blue lines.

For the period between January 1993 and December 2014, there are around 8000 eddy trajectories in the study region (55°W - 10°W and 40°N - 55°N). In general the eddies are tracked for longer periods than the eddies detected with the vector geometry based algorithm used in this thesis. Both the average eddy travel distance ($\overline{d}$=550 km) and average lifetime ($\overline{\tau}$=90 days) are longer than those of eddies detected in this thesis ($\overline{d}$=73 km, $\overline{\tau}$=23 days). A comparison of the trajectories of detected eddies for the year 2000 is shown in Figure 5.2. The eddy trajectories detected with the algorithm by Nencioli et al. (2010) seem

to be somewhat fragmented when comparing with the trajectories of the META product. Despite this striking difference, the META trajectories agree with the main results from this thesis. The main pathway of eddies across 47°N is in the western basin with the main current branches. There is also a number of cyclonic eddies originating from the WBC (Figure 5.2,a). Despite the overall longer continuous trajectories for the *Mesoscale Eddy Trajectory Atlas product*, the eddy trajectories terminate not long after crossing 47°N, confirming that the effect of fluxes by eddies crossing 47°N is regionally confined.

Nevertheless, the large differences in the length of eddy trajectories raises the question whether the vector geometry based method by Nencioli et al. (2010) really is the ideal algorithm for the study region. The method that is less strict with regard to the geometry of the eddies (META) reveals longer connected trajectories, while the geometry based algorithm reveals many short lived eddies. The question remaining is: Which method is the more reliable?

Visual analysis of snapshots of the velocity field in the Newfoundland Basin (Figure 5.3) shows that small eddies are better detected by the vector geometry based algorithm than the META algorithm. The two small cyclonic eddies forming between Jan. 25 and Feb. 10 for example are not detected at all by the META algorithm. In some cases theses small eddies are deformed, interact with other eddies and often turn into more open shapes rather than closed rings, or merge into one larger eddy (e.g., Feb. 10 - Feb. 18). In this case the SLA based algorithm used to identify the META trajectories shows rather unrealistic, sometimes very large features (e.g., Feb. 20). However, once the larger merged eddy is established, it is represented continuously in the META data set (albeit sometimes too large). The vector geometry based algorithm on the other hand tends to "lose" eddies sometimes (e.g., Mar. 8 - Mar. 14) and the respective trajectory will be identified as terminated.

If the focus of a study is generally on "turbulent features" in the ocean, the META data set seems to be a reliable source. Potential outliers for the eddy radius will have to be treated with care. In the case of this thesis, the question was explicitly for coherent vortices and the temperature and freshwater fluxes related to these eddies. Despite the somewhat short eddy trajectories, the algorithm by Nencioli et al. (2010) is therefore a suitable method. It is able to differentiate between different small features and shows consistent outer boundaries for the detected eddies. The detected eddies seem a little small when compared to the velocity field, which could be a source for a systematic underestimation of the fluxes by eddies. A study comparing different eddy detection algorithms also

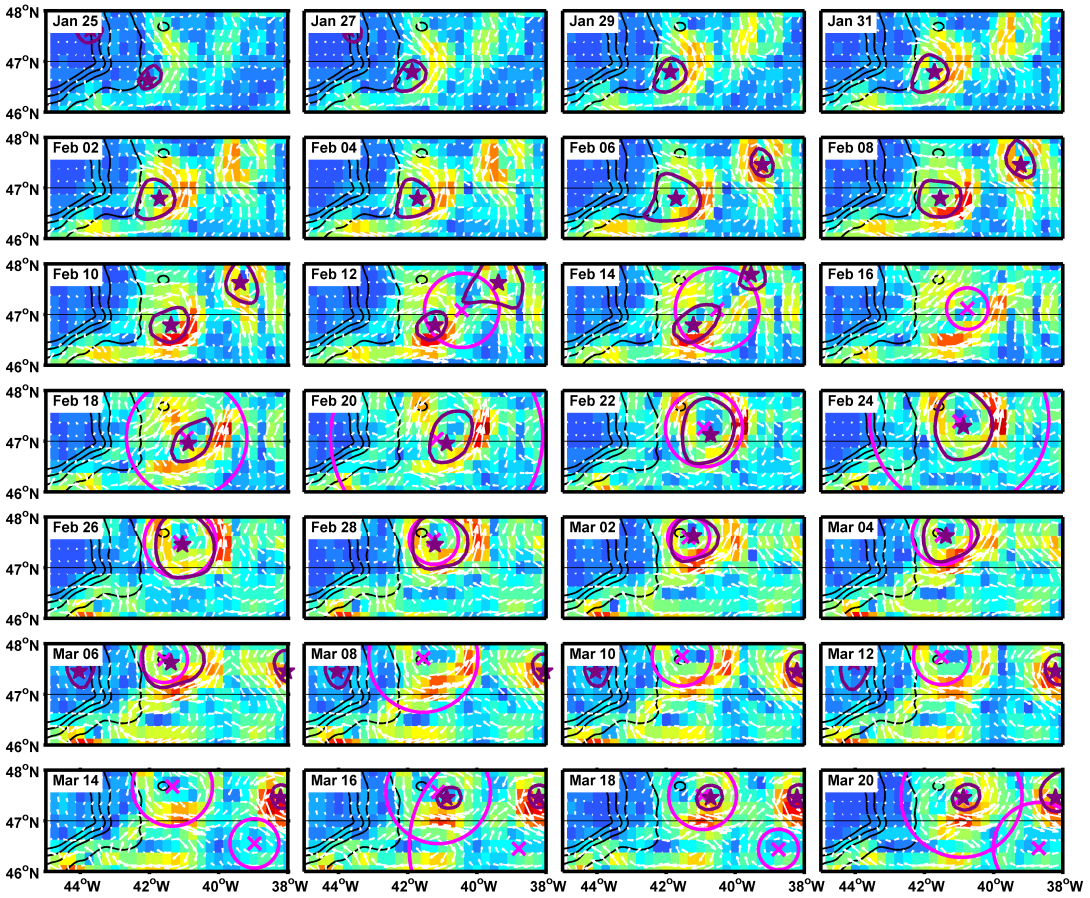

Figure 5.3: Example of eddies detected in the Newfoundland Basin in the spring of 1993 from the vector geometry based algorithm (purple, centers marked with ★ Nencioli et al., 2010) and from the *Mesoscale Eddy Trajectory Atlas product* (magenta, centers marked with **x**, Schlax and Chelton, 2016) . The background colors indicate current speed. Velocity vectors are shown with white arrows. Only snapshots form every second day are shown.

showed that the eddies detected with the vector geometry based algorithm are in general somewhat smaller than the eddies detected with other methods (Escudier et al., 2016).

The GEM technique chosen here to calculate the fluxes by individual eddies has its limitations. The method does not work everywhere in the North Atlantic, it is limited to the upper 1900 dbar of the water column, and only eddies with a surface signature can be detected. However, I have shown that it is a suitable technique to infer temperature and freshwater fluxes by individual eddies from sea surface height.

While the GEM method is based on statistical connections between surface properties and the interior, Wang et al. (2013) and Liu et al. (2017) introduced a dynamical approach to infer hydrographic data in depth from surface properties.

The so-called interior+surface Quasi-Geostrophic (isQG) method makes use of the connection between surface observations of SSH and sea surface density (SSD) and the underlying velocity and density fields. For that, the flow is assumed to be in quasi-geostrophic balance $\left(\text{i.e. } \nabla^2\psi + \frac{\partial}{\partial z}\left(\frac{f_0^2}{N^2}\frac{\partial\psi}{\partial z}\right) = Q \text{ and } f_0\frac{\partial\psi}{\partial z} = b\right)$, where ψ is the streamfunction, f_0 is the Coriolis frequency, N is the Brunt-Väisälä frequency, Q is the anomaly from the large-scale planetary potential vorticity and $b = -g\rho/\rho_0$ is the buoyancy. The streamfunction ψ is split into a surface component ψ_s and a component for the interior ocean ψ_i by inverting the equation and using the respective boundary conditions for Q and b (Lapeyre and Klein, 2006). While this works well for the surface, several additional assumptions have to be made for the interior ocean to infer the barotropic and the first baroclinic modes (Wang et al., 2013; Liu et al., 2017).

However, further improving methods such as the GEM or isQG technique could provide subsurface data that will help better understanding mesoscale as well as large scale dynamics.

Improving the existing eddy detection and tracking methods is also a necessary step to improve and advance the research on mesoscale eddies. As mentioned in chapter 2.4, all algorithms have their strengths and weaknesses. Many of the methods depend on a - somewhat arbitrary - choice of parameters (e.g., Chelton et al., 2007; Nencioli et al., 2010). A new algorithm is the parameter-free method by Faghmous et al. (2015), but it remains to be seen where exactly the upsides of this rather new method lie, and whether it is an improvement over existing algorithms. Also the new *Mesoscale Eddy Trajectory Atlas product* based on the detection algorithm by Schlax and Chelton (2016) is a promising product, but as of now it is still in an experimental stage.

Another follow-up to the work presented in this thesis is the question of how eddies influence the local biology. Cold and fresh eddies detaching from the WBC will not only change the thermohaline properties of the NAC water, they will also carry oxygen and nutrients from the boundary current into the warm water of the NAC. By providing nutrients, eddies can influence or even induce phytoplankton blooms, and can have a direct (e.g. by changing the temperature) and indirect (e.g. by inducing more primary production) influence on the habitats of larger animals such as fish. In the Gulf Stream region eddies can influence the distribution of chlorophyl by lateral advection and Ekman upwelling of nutrients (Gaube and McGillicuddy, 2017). By collocating the trajectories of sea turtles with the tracks of mesoscale eddies Gaube et al. (2017) have also shown that sea turtles are significantly more likely to be found in anticyclonic eddies. The connection

between eddies and nutrient distribution and fluxes in a model environment could be investigated using an ocean model configuration in combination with a biogeochemical model. First attempts to couple the "Biogeochemical with Light, Iron, and Nutrient limitation and Gases" model (BLING, Galbraith et al., 2010) to the NEMO model are done in the Numerical Modeling Group at the University of Alberta.

Last but not least, another open question is - as almost always in oceanography: "What happens on even smaller scales?". The mesoscale eddies analyzed in this thesis are only the rather large coherent structures in the region. On submesoscales, there are even smaller eddies and filaments that lead to the actual mixing, stirring and dissipation of water masses. Very high resolution model simulations (e.g. 1/60°) could prove to be of great benefit for understanding local small scale processes especially in regions where the Rossby radius is even smaller than in the study region of this thesis (e.g. in the Labrador Sea). A comparison of high resolution simulations with existing methods can also help to understand which processes are still underrepresented and how much of the small scale variability is missed with the current methods. However, these kind of simulations are very expensive and bring a number of new problems (e.g. numerical stability, parametrizations, coupling with existing lower resolution models). On the side of observations, more and more Argo floats will greatly help to understand mesoscale and submesoscale processes. But in order to get an overall large scale picture, high resolution satellite observations, such as the Surface Water & Ocean Topography (SWOT, `swot.jpl.nasa.gov`) mission, might be the only real option. This new mission is planned to launch in April 2021 and will measure ocean features with 10 times the resolution of current technologies.

6 Concluding Remarks

This thesis adds one "piece of the puzzle" to the big question of how heat and freshwater are distributed in the ocean. The results presented here focus on a region that is of great relevance for the climate system and provide a better understanding of the contribution of eddies to the fluxes of heat and freshwater. Even though the focus of my thesis was not on long term changes, understanding the fluxes and their variability due to eddies will help to better understand present and future changes to the climate system. Getting a better grasp on the drivers of the variability will also help to separate between the different factors that influence the changing climate (e.g. natural variability vs. anthropogenic climate change). Furthermore, the results from this thesis will complement the results from other observational studies focusing on the section along 47°N, and help to better understand the observed variability in the region.

The comparison of observations with model results provides two benefits. On the one hand, my work is the first evaluation of the model with regard to the representation of temperature and freshwater fluxes by individual eddies. I have shown that a horizontal resolution of 1/4° is not high enough to allow for a representation of fluxes by individual eddies that is comparable to the fluxes derived from 1/4° satellite observations. In the subpolar North Atlantic, a horizontal resolution of at least 1/12° is necessary in order to get reasonable fluxes by individual eddies. Keep in mind however, that the AVISO satellite observations also do not resolve all small scale processes.

On the other hand, after showing that the model gives reasonable results for the temperature and freshwater fluxes across 47°N, it can be used to analyze fluxes by eddies in regions where there are only few or no observational data available. This could be for example the eastern part of the East Atlantic, where it is not possible to construct unique GEM fields.

Overall, the results presented in this thesis are relevant for both the observational oceanography community and the ocean modeling community.

Bibliography

Abraham, E. R. and Bowen, M. M. Chaotic stirring by a mesoscale surface-ocean flow. *Chaos: An Interdisciplinary Journal of Nonlinear Science*, 12(2):373–381, 2002. doi: 10.1063/1.1481615.

Amante, C. and Eakins, B. ETOPO1 1 Arc-Minute Global Relief Model: Procedures, Data Sources and Analysis, 2009. ISSN 1680-7375. URL `http://www.ngdc.noaa.gov/mgg/global/global.html`.

Arakawa, A. and Lamb, V. R. Computational design of the basic dynamical processes of the ucla general circulation model. *Methods in computational physics*, 17:173–265, 1977.

Beal, L. M., De Ruijter, W. P. M., Biastoch, A., and Zahn, R. On the role of the Agulhas system in ocean circulation and climate. *Nature*, 472(7344):429–36, 2011. doi: 10.1038/nature09983.

Bernard, B., Madec, G., Penduff, T., Molines, J. M., Treguier, A. M., Le Sommer, J., Beckmann, A., Biastoch, A., Böning, C., Dengg, J., Derval, C., Durand, E., Gulev, S., Remy, E., Talandier, C., Theetten, S., Maltrud, M., McClean, J., and De Cuevas, B. Impact of partial steps and momentum advection schemes in a global ocean circulation model at eddy-permitting resolution. *Ocean Dynamics*, 56(5-6):543–567, 2006. doi: 10.1007/s10236-006-0082-1.

Biastoch, A., Böning, C. W., and Lutjeharms, J. R. E. Agulhas leakage dynamics affects decadal variability in Atlantic overturning circulation. *Nature*, 456 (7221):489–492, 2008. doi: 10.1038/nature07426.

Böning, C. W., Behrens, E., Biastoch, A., Getzlaff, K., and Bamber, J. L. Emerging impact of Greenland meltwater on deepwater formation in the North Atlantic Ocean. *Nature Geoscience*, 9(7):523–527, 2016. doi: 10.1038/ngeo2740.

Bougeault, P. and Lacarrere, P. Parameterization of Orography-Induced Turbulence in a Mesobeta–Scale Model. *Monthly Weather Review*, 117(8):1872–1890, 1989. doi: 10.1175/1520-0493(1989)117<1872:POOITI>2.0.CO;2.

Bower, A., Lozier, S., and Gary, S. Export of Labrador Sea Water from the subpolar North Atlantic: A Lagrangian perspective. *Deep-Sea Research Part II: Topical Studies in Oceanography*, 58(17-18):1798–1818, 2011. doi: 10.1016/j.dsr2.2010.10.060.

Bower, A. S. and von Appen, W.-J. Interannual Variability in the Pathways of the North Atlantic Current over the Mid-Atlantic Ridge and the Impact of Topography. *Journal of Physical Oceanography*, 38(1):104–120, 2008. doi: 10.1175/2007JPO3686.1.

Bower, A. S., Lozier, M. S., Gary, S. F., and Böning, C. W. Interior pathways of the North Atlantic meridional overturning circulation. *Nature*, 459(7244): 243–247, 2009. doi: 10.1038/nature07979.

Bower, A. S., Hendry, R. M., Amrhein, D. E., and Lilly, J. M. Direct observations of formation and propagation of subpolar eddies into the Subtropical North Atlantic. *Deep-Sea Research Part II: Topical Studies in Oceanography*, 85: 15–41, 2013. doi: 10.1016/j.dsr2.2012.07.029.

Bryan, K. A numerical method for the study of the circulation of the world ocean. *Journal of Computational Physics*, 4(3):347–376, 1969. doi: 10.1016/0021-9991(69)90004-7.

Bryden, H. L. and Imawaki, S. Chapter 6.1 ocean heat transport. *International Geophysics*, 77:455 – 474, 2001. doi: 10.1016/S0074-6142(01)80134-0. Ocean Circulation and Climate.

Carr, M.-E. and Rossby, H. T. Pathways of the North Atlantic Current from surface drifters and subsurface floats. *Journal of Geophysical Research: Oceans*, 106(C3):4405–4419, 2001. doi: 10.1029/2000JC900106.

Chaigneau, A., Gizolme, A., and Grados, C. Mesoscale eddies off Peru in altimeter records: Identification algorithms and eddy spatio-temporal patterns. *Progress in Oceanography*, 79(2-4):106–119, 2008. doi: 10.1016/j.pocean.2008.10.013.

Chelton, D. B. and Schlax, M. G. Global Observations of Oceanic Rossby Waves. *Science*, 272(5259):234–238, 1996. doi: 10.1126/science.272.5259.234.

Chelton, D. B. and Schlax, M. G. The accuracies of smoothed sea surface height fields constructed from tandem satellite altimeter datasets. *Journal of Atmospheric and Oceanic Technology*, 20(9):1276–1302, 2003. doi: 10.1175/1520-0426(2003)020<1276:TAOSSS>2.0.CO;2.

Chelton, D. B., DeSzoeke, R. a., Schlax, M. G., El Naggar, K., and Siwertz, N. Geographical Variability of the First Baroclinic Rossby Radius of Deformation. *Journal of Physical Oceanography*, 28(3):433–460, 1998. doi: 10.1175/1520-0485(1998)028<0433:GVOTFB>2.0.CO;2.

Chelton, D. B., Schlax, M. G., Samelson, R. M., and de Szoeke, R. A. Global observations of large oceanic eddies. *Geophysical Research Letters*, 34(15): L15606, 2007. doi: 10.1029/2007GL030812.

Chelton, D. B., Schlax, M. G., and Samelson, R. M. Global observations of nonlinear mesoscale eddies. *Progress in Oceanography*, 91(2):167–216, 2011. doi: 10.1016/j.pocean.2011.01.002.

Cheney, R. E., Marsh, J. G., and Beckely, B. D. Global mesoscale variability from collinear tracks of SEASAT altimeter data. *Journal of Geophysical Research*, 88(C7):4343–4354, 1983. doi: 10.1029/JC088iC07p04343.

Courant, R., Friedrichs, K., and Lewy, H. Über die partiellen Differenzengleichungen der mathematischen Physik. *Mathematische Annalen*, 100(1):32–74, 1928. doi: 10.1007/BF01448839.

Dai, A., Qian, T., Trenberth, K. E., and Milliman, J. D. Changes in continental freshwater discharge from 1948 to 2004. *Journal of Climate*, 22(10):2773–2792, 2009. doi: 10.1175/2008JCLI2592.1.

Danabasoglu, G. and McWilliams, J. C. Sensitivity of the global ocean circulation to parameterizations of mesoscale tracer transports. *Journal of Climate*, 8(12): 2967–2987, 1995. doi: 10.1175/1520-0442(1995)0082.0.CO;2.

Debreu, L., Vouland, C., and Blayo, E. AGRIF: Adaptive grid refinement in Fortran. *Computers and Geosciences*, 34(1):8–13, 2008. doi: 10.1016/j.cageo.2007.01.009.

Dengler, M., Schott, F. a., Eden, C., Brandt, P., Fischer, J., and Zantopp, R. J. Break-up of the Atlantic deep western boundary current into eddies at 8 degrees S. *Nature*, 432(7020):1018–1020, 2004. doi: 10.1038/nature03134.

Doblar, R. A. and Cheney, R. E. Observed Formation of a Gulf Stream Cold Core Ring. *Journal of Physical Oceanography*, 7(6):944–946, 1977. doi: 10.1175/1520-0485(1977)007<0944:OFOAGS>2.0.CO;2.

Doglioli, A. M., Blanke, B., Speich, S., and Lapeyre, G. Tracking coherent structures in a regional ocean model with wavelet analysis: Application to Cape Basin eddies. *Journal of Geophysical Research: Oceans*, 112(5):C05043, 2007. doi: 10.1029/2006JC003952.

Dong, C. Global eddy data set: people.atmos.ucla.edu/cdong/Global_Eddy_Data_SSHA/, 2012. URL `people.atmos.ucla.edu/cdong/Global_Eddy_Data_SSHA/`.

Dong, C., Lin, X., Liu, Y., Nencioli, F., Chao, Y., Guan, Y., Chen, D., Dickey, T., and McWilliams, J. C. Three-dimensional oceanic eddy analysis in the Southern California Bight from a numerical product. *Journal of Geophysical Research: Oceans*, 117(1):1–17, 2012. doi: 10.1029/2011JC007354.

Dong, C., McWilliams, J. C., Liu, Y., and Chen, D. Global heat and salt transports by eddy movement. *Nature communications*, 5:3294, 2014. doi: 10.1038/ncomms4294.

Ducet, N., Le Traon, P. Y., and Reverdin, G. Global high-resolution mapping of ocean circulation from TOPEX/Poseidon and ERS-1 and -2. *Journal of Geophysical Research*, 105498(15):477–19, 2000. doi: 10.1029/2000JC900063.

Dukhovskoy, D. S., Myers, P. G., Platov, G., Timmermans, M. L., Curry, B., Proshutinsky, A., Bamber, J. L., Chassignet, E., Hu, X., Lee, C. M., and Somavilla, R. Greenland freshwater pathways in the sub-Arctic Seas from model experiments with passive tracers. *Journal of Geophysical Research: Oceans*, 121(1):877–907, 2016. doi: 10.1002/2015JC011290.

Dutkiewicz, S., Rothstein, L., and Rossby, T. Pathways of cross-frontal exchange in the North Atlantic Current. *Journal of Geophysical Research: Oceans*, 106 (C11):26917–26928, 2001. doi: 10.1029/1999JC000089.

Eady, E. T. Long Waves and Cyclone Waves. *Tellus A*, 1(3):33–52, 1949. doi: 10.3402/tellusa.v1i3.8507.

Egbert, G. D. and Erofeeva, S. Y. Efficient inverse modeling of barotropic ocean tides. *Journal of Atmospheric and Oceanic Technology*, 19(2):183–204, 2002. doi: 10.1175/1520-0426(2002)019<0183:EIMOBO>2.0.CO;2.

Escudier, R., Renault, L., Pascual, A., Brasseur, P., Chelton, D., and Beuvier, J. Eddy properties in the Western Mediterranean Sea from satellite altimetry

and a numerical simulation. *Journal of Geophysical Research: Oceans*, 121(6): 3990–4006, 2016. doi: 10.1002/2015JC011371.

Faghmous, J. H., Frenger, I., Yao, Y., Warmka, R., Lindell, A., and Kumar, V. A daily global mesoscale ocean eddy dataset from satellite altimetry. *Scientific Data*, 2:150028, 2015. doi: 10.1038/sdata.2015.28.

Ferry, N., Parent, L., Garric, G., Barnier, B., and Jourdain, N. C. Mercator global Eddy permitting ocean reanalysis GLORYS1V1: Description and results. *Mercator-Ocean Quarterly Newsletter*, 34:15–27, 2010.

Fichefet, T. and Maqueda, M. A. Sensitivity of a global sea ice model to the treatment of ice thermodynamics and dynamics. *Journal of Geophysical Research: Oceans*, 102(C6):12609–12646, 1997. doi: 10.1029/97JC00480.

Font, J., Lagerloef, G. S., Le Vine, D. M., Camps, A., and Zanifé, O. Z. The determination of surface salinity with the European SMOS space mission. *IEEE Transactions on Geoscience and Remote Sensing*, 42(10):2196–2205, 2004. doi: 10.1109/TGRS.2004.834649.

Fratantoni, D. M. North Atlantic surface circulation during the 1990's observed with satellite-tracked drifters. *Journal of Geophysical Research: Oceans*, 106 (C10):22067–22093, 2001. doi: 10.1029/2000JC000730.

Fratantoni, D. M. and Glickson, D. a. North Brazil Current Ring Generation and Evolution Observed with SeaWiFS. *Journal of Physical Oceanography*, 32(3): 1058–1074, 2002. doi: 10.1175/1520-0485(2002)032<1058:NBCRGA>2.0.CO; 2.

Fu, L.-L., Chelton, D. B., and Zlotnicki, V. Satellite altimetry: Observing ocean variability from space. *Oceanography*, 1(2):4–58, 1988.

Fu, L.-L., Christensen, E. J., Yamarone, C. A., Lefebvre, M., Ménard, Y., Dorrer, M., and Escudier, P. TOPEX/POSEIDON mission overview. *Journal of Geophysical Research*, 99(C12):24369, 1994. doi: 10.1029/94JC01761.

Fuglister, F. C. Cyclonic rings formed by the Gulf Stream 1965-66. In Gordon, A. L., editor, *Studies in Physical Oceanography*, pages 137–168. Gordon and Breach, New York, first edition, 1972.

Galbraith, E. D., Gnanadesikan, A., Dunne, J. P., and Hiscock, M. R. Regional impacts of iron-light colimitation in a global biogeochemical model. *Biogeosciences*, 7(3):1043–1064, 2010. doi: 10.5194/bgd-6-7517-2009.

Ganachaud, A. and Wunsch, C. Improved estimates of global ocean circulation, heat transport and mixing from hydrographic data. *Nature*, 408(6811):453–457, 2000. doi: 10.1038/35044048.

Ganachaud, A. and Wunsch, C. Large-scale ocean heat and freshwater transports during the world ocean circulation experiment. *Journal of Climate*, 16(4):696–705, 2003. doi: 10.1175/1520-0442(2003)016<0696:LSOHAF>2.0.CO;2.

Gaube, P. and McGillicuddy, D. J. The influence of Gulf Stream eddies and meanders on near-surface chlorophyll. *Deep Sea Research Part I: Oceanographic Research Papers*, 122:1–16, 2017. doi: 10.1016/j.dsr.2017.02.006.

Gaube, P., Barceló, C., McGillicuddy, D. J., Domingo, A., Miller, P., Giffoni, B., Marcovaldi, N., and Swimmer, Y. The use of mesoscale eddies by juvenile loggerhead sea turtles (Caretta caretta) in the southwestern Atlantic. *PLoS ONE*, 12(3), 2017. doi: 10.1371/journal.pone.0172839.

Gent, P. R. and Mcwilliams, J. C. Isopycnal Mixing in Ocean Circulation Models. *Journal of Physical Oceanography*, 20(1):150–155, 1990. doi: 10.1175/1520-0485(1990)020<0150:IMIOCM>2.0.CO;2.

Gill, A. E., Green, J. S. A., and Simmons, A. J. Energy partition in the large-scale ocean circulation and the production of mid-ocean eddies. *Deep-Sea Research and Oceanographic Abstracts*, 21(7):499–528, 1974. doi: 10.1016/0011-7471(74)90010-2.

Goni, G. J. and Malanotte-Rizzoli, P., editors. *Interhemispheric Water Exchange in the Atlantic Ocean*, volume 68. Elsevier B.V., Amsterdam, first edition, 2003. ISBN 9780444512673. doi: 10.1016/S0422-9894(03)80147-2.

Gordon, A. L. and Giulivi, C. F. Ocean eddy freshwater flux convergence into the North Atlantic subtropics. *Journal of Geophysical Research: Oceans*, 119(6):3327–3335, 2014. doi: 10.1002/2013JC009596.

Griffies, S. M., Gnanadesikan, A., Pacanowski, R. C., Larichev, V. D., Dukowicz, J. K., Smith, R. D., Griffies, S. M., Gnanadesikan, A., Pacanowski, R. C., Larichev, V. D., Dukowicz, J. K., and Smith, R. D. Isoneutral Diffusion in a z-Coordinate Ocean Model. *Journal of Physical Oceanography*, 28(5):805–830, 1998. doi: 10.1175/1520-0485(1998)028<0805:IDIAZC>2.0.CO;2.

Holdsworth, A. M. and Myers, P. G. The influence of high-frequency atmospheric forcing on the circulation and deep convection of the Labrador Sea. *Journal of Climate*, 28(12):4980–4996, 2015. doi: 10.1175/JCLI-D-14-00564.1.

Hunke, E. C. and Dukowicz, J. K. An Elastic - Viscous - Plastic Model for Sea Ice Dynamics. *J. Phys. Oceanogr*, 27(9):1849–1867, 1997. doi: 10.1175/1520-0485.

Iselin, C. O. *A study of the circulation of the western North Atlantic*, volume 2. Massachusetts Institute of Technology and Woods Hole Oceanographic Institution, Cambridge, MA, 1936. doi: 10.1575/1912/1087.

Isern-Fontanet, J., García-Ladona, E., and Font, J. Identification marine eddies from altimetric maps. *Journal of Atmospheric and Oceanic Technology*, 20(5): 772–778, 2003. doi: 10.1175/1520-0426(2003)20<772:IOMEFA>2.0.CO;2.

Jeong, J. and Hussain, F. On the identification of a vortex. *Journal of Fluid Mechanics*, 285(February):69–94, 1995. doi: doi:10.1017/S0022112095000462.

Johns, W. E., Baringer, M. O., Beal, L. M., Cunningham, S. A., Kanzow, T., Bryden, H. L., Hirschi, J. J. M., Marotzke, J., Meinen, C. S., Shaw, B., and Curry, R. Continuous, Array-Based Estimates of Atlantic Ocean Heat Transport at 26.5°N. *Journal of Climate*, 24(10):2429–2449, 2011. doi: 10.1175/2010JCLI3997.1.

Katsman, C. A., Spall, M. A., and Pickart, R. S. Boundary Current Eddies and Their Role in the Restratification of the Labrador Sea. *Journal of Physical Oceanography*, 34(9):1967–1983, 2004. doi: 10.1175/1520-0485(2004)034<1967:BCEATR>2.0.CO;2.

Kearns, E. J. and Rossby, H. T. Historical position of the North Atlantic Current. *Journal of Geophysical Research: Oceans*, 103(C8):15509–15524, 1998. doi: 10.1029/98JC00370.

Kieke, D. and Yashayaev, I. Studies of Labrador Sea Water formation and variability in the subpolar North Atlantic in the light of international partnership and collaboration. *Progress in Oceanography*, 132:220–232, 2015. doi: 10.1016/j.pocean.2014.12.010.

Kieke, D., Klein, B., Stramma, L., Rhein, M., and Koltermann, K. P. Variability and propagation of Labrador Sea Water in the southern subpolar North Atlantic. *Deep-Sea Research Part I: Oceanographic Research Papers*, 56(10): 1656–1674, 2009. doi: 10.1016/j.dsr.2009.05.010.

Köhler, J., Sena Martins, M., Serra, N., and Stammer, D. Quality assessment of spaceborne sea surface salinity observations over the northern North Atlantic. *Journal of Geophysical Research: Oceans*, 120(1):94–112, 2015. doi: 10.1002/2014JC010067.

Kuhlbrodt, T., Griesel, A., Montoya, M., Levermann, A., Hofmann, M., and Rahmstorf, S. On the driving processes of the Atlantic meridional overturning circulation. *Reviews of Geophysics*, 45(2):RG2001, 2007. doi: 10.1029/2004RG000166.

Lapeyre, G. and Klein, P. Dynamics of the Upper Oceanic Layers in Terms of Surface Quasigeostrophy Theory. *Journal of Physical Oceanography*, 36(2):165–176, 2006. doi: 10.1175/JPO2840.1.

Le Traon, P. Y., Nadal, F., and Ducet, N. An improved mapping method of multisatellite altimeter data. *Journal of Atmospheric and Oceanic Technology*, 15(2):522–534, 1998. doi: 10.1175/1520-0426(1998)015<0522:AIMMOM>2.0.CO;2.

Le Traon, P. Y., Faugère, Y., Hernandez, F., Dorandeu, J., Mertz, F., and Ablain, M. Can we merge GEOSAT follow-on with TOPEX/Poseidon and ERS-2 for an improved description of the ocean circulation? *Journal of Atmospheric and Oceanic Technology*, 20(6):889–895, 2003. doi: 10.1175/1520-0426(2003)020<0889:CWMGFW>2.0.CO;2.

Lilly, J. M., Rhines, P. B., Schott, F., Lavender, K., Lazier, J., Send, U., and D'Asaro, E. Observations of the Labrador Sea eddy field. *Progress in Oceanography*, 59(1):75–176, 2003. doi: 10.1016/j.pocean.2003.08.013.

Liu, L., Peng, S., and Huang, R. X. Reconstruction of ocean's interior from observed sea surface information. *Journal of Geophysical Research: Oceans*, 122(2):1042–1056, 2017. doi: 10.1002/2016JC011927.

Liu, Y., Dong, C., Guan, Y., Chen, D., McWilliams, J., and Nencioli, F. Eddy analysis in the subtropical zonal band of the North Pacific Ocean. *Deep-Sea Research Part I: Oceanographic Research Papers*, 68:54–67, 2012. doi: 10.1016/j.dsr.2012.06.001.

Locarini, R. A., Mishonov, A. V., Antonov, J. I., Boyer, T. P., Garcia, H. E., Baranova, O. K., Zweng, M. M., Paver, C. R., Reagan, J. R., Johnson, D. R., Hamilton, M., and Seidov, D. Temperature. In Levitus, S. and Mishonov,

A. V., editors, *World Ocean Atlas 2013*, volume 1, page 40 pp. NOAA Atlas NESDIS 74, 2013. URL `http://www.nodc.noaa.gov/OC5/indprod.html`.

Ma, X., Jing, Z., Chang, P., Liu, X., Montuoro, R., Small, R. J., Bryan, F. O., Greatbatch, R. J., Brandt, P., Wu, D., Lin, X., and Wu, L. Western boundary currents regulated by interaction between ocean eddies and the atmosphere. *Nature*, 535(7613):533–537, 2016. doi: 10.1038/nature18640.

Madec, G. and the NEMO team. *NEMO ocean engine*. Note du Pôle modélisation, 27, Institut Pierre-Simon, France, 2008.

Mann, C. The termination of the Gulf Stream and the beginning of the North Atlantic Current. *Deep Sea Research and Oceanographic Abstracts*, 14(3):337–359, 1967. doi: 10.1016/0011-7471(67)90077-0.

Marsh, R., de Cuevas, B. A., Coward, A. C., Jacquin, J., Hirschi, J. J., Aksenov, Y., Nurser, A. J., and Josey, S. A. Recent changes in the North Atlantic circulation simulated with eddy-permitting and eddy-resolving ocean models. *Ocean Modelling*, 28(4):226–239, 2009. doi: 10.1016/j.ocemod.2009.02.007.

Marshall, J., Kushnir, Y., Battisti, D., Chang, P., Czaja, A., Dickson, R., Hurrell, J., McCartney, M., Saravanan, R., and Visbeck, M. North Atlantic climate variability: Phenomena, impacts and mechanisms. *International Journal of Climatology*, 21(15):1863–1898, 2001. doi: 10.1002/joc.693.

McCarthy, G. D., Smeed, D. A., Johns, W. E., Frajka-Williams, E., Moat, B. I., Rayner, D., Baringer, M. O., Meinen, C. S., Collins, J., and Bryden, H. L. Measuring the Atlantic Meridional Overturning Circulation at 26°N. *Progress in Oceanography*, 130(January):91–111, 2015. doi: 10.1016/j.pocean.2014.10.006.

McManus, J. F., Francois, R., Gherardi, J.-M., Keigwin, L. D., and Brown-Leger, S. Collapse and rapid resumption of Atlantic meridional circulation linked to deglacial climate changes. *Nature*, 428(6985):834–837, 2004. doi: 10.1038/nature02494.

Meijers, A. J. S., Bindoff, N. L., and Rintoul, S. R. Estimating the four-dimensional structure of the southern ocean using satellite altimetry. *Journal of Atmospheric and Oceanic Technology*, 28(4):548–568, 2011. doi: 10.1175/2010JTECHO790.1.

Meinen, C. S. and Watts, D. R. Vertical structure and transport on a transect across the North Atlantic Current near 42°N: Time series and mean. *Journal of Geophysical Research: Oceans*, 105(C9):21869–21891, 2000. doi: 10.1029/2000JC900097.

Melnichenko, O., Hacker, P., Maximenko, N., Lagerloef, G., and Potemra, J. Optimum interpolation analysis of Aquarius sea surface salinity. *Journal of Geophysical Research: Oceans*, 121(1):602–615, 2016. doi: 10.1002/2015JC011343.

Mertens, C., Rhein, M., Walter, M., and Kirchner, K. Modulation of the inflow into the Caribbean Sea by North Brazil Current rings. *Deep Sea Research Part I: Oceanographic Research Papers*, 56(7):1057–1076, 2009. doi: 10.1016/j.dsr.2009.03.002.

Mertens, C., Rhein, M., Walter, M., Böning, C. W., Behrens, E., Kieke, D., Steinfeldt, R., and Stöber, U. Circulation and transports in the Newfoundland Basin, western subpolar North Atlantic. *Journal of Geophysical Research: Oceans*, 119(11):7772–7793, 2014. doi: 10.1002/2014JC010019.

Müller, V., Kieke, D., Myers, P. G., Pennelly, C., and Mertens, C. Temperature flux carried by individual eddies across 47°N in the Atlantic Ocean. *Journal of Geophysical Research: Oceans*, 122(3):2441–2464, 2017. doi: 10.1002/2016JC012175.

Nencioli, F., Dong, C., Dickey, T., Washburn, L., and Mcwilliams, J. C. A vector geometry-based eddy detection algorithm and its application to a high-resolution numerical model product and high-frequency radar surface velocities in the Southern California Bight. *Journal of Atmospheric and Oceanic Technology*, 27(3):564–579, 2010. doi: 10.1175/2009JTECHO725.1.

Okubo, A. Horizontal dispersion of floatable particles in the vicinity of velocity singularities such as convergences. *Deep-Sea Research and Oceanographic Abstracts*, 17(3):445–454, 1970. doi: 10.1016/0011-7471(70)90059-8.

Olbers, D., Willebrand, J., and Eden, C. *Ocean Dynamics*, volume 53. Springer Berlin Heidelberg, Berlin, Heidelberg, 2012. ISBN 978-3-642-23449-1. doi: 10.1007/978-3-642-23450-7.

Pérez-Brunius, P., Rossby, T., and Watts, D. R. Absolute Transports of Mass and Temperature for the North Atlantic Current-Subpolar Front System. *Journal of Physical Oceanography*, 34(8):1870–1883, 2004. doi: 10.1175/1520-0485(2004)034<1870:ATOMAT>2.0.CO;2.

Phillips, N. A. Energy Transforms and Meridional Circulations associated with simple Baroclinic Waves in a two-level, Quasi-geostrophic Model. *Tellus*, 6(3): 273–286, 1954. doi: 10.3402/tellusa.v6i3.8734.

Rahmstorf, S. Bifurcations of the Atlantic thermohaline circulation in repsonse to changes in the hydrological cycle. *Nature*, 378(November):145–149, 1995.

Rahmstorf, S. Ocean circulation and climate during the past 120,000 years. *Nature*, 419(6903):207–214, 2002. doi: 10.1038/nature01090.

Rahmstorf, S., Crucifix, M., Ganopolski, A., Goosse, H., Kamenkovich, I., Knutti, R., Lohmann, G., Marsh, R., Mysak, L. A., Wang, Z., and Weaver, A. J. Thermohaline circulation hysteresis: A model intercomparison. *Geophysical Research Letters*, 32(23):L23605, 2005. doi: 10.1029/2005GL023655.

Redi, M. H. Oceanic Isopycnal Mixing by Coordinate Rotation. *Journal of Physical Oceanography*, 12(10):1154–1158, 1982. doi: 10.1175/1520-0485(1982)012<1154:OIMBCR>2.0.CO;2.

Reynolds, R. W., Smith, T. M., Liu, C., Chelton, D. B., Casey, K. S., and Schlax, M. G. Daily high-resolution-blended analyses for sea surface temperature. *Journal of Climate*, 20(22):5473–5496, 2007. doi: 10.1175/2007JCLI1824.1.

Rhein, M., Kieke, D., Hüttl-Kabus, S., Roessler, A., Mertens, C., Meissner, R., Klein, B., Böning, C. W., and Yashayaev, I. Deep water formation, the subpolar gyre, and the meridional overturning circulation in the subpolar North Atlantic. *Deep-Sea Research Part II: Topical Studies in Oceanography*, 58(17-18):1819–1832, 2011. doi: 10.1016/j.dsr2.2010.10.061.

Rhein, M., Kieke, D., and Steinfeldt, R. Advection of North Atlantic Deep Water from the Labrador Sea to the southern hemisphere. *Journal of Geophysical Research*, 120(4):2471–2487, 2015. doi: 10.1002/2014JC010605.Received.

Rhines, P., Häkkinen, S., and Josey, S. A. *Is Oceanic Heat Transport Significant in the Climate System?*, In *Arctic–Subarctic Ocean Fluxes: Defining the Role of the Northern Seas in Climate*, pages 87–109. Springer Netherlands, Dordrecht, 2008. ISBN 978-1-4020-6774-7. doi: 10.1007/978-1-4020-6774-7_5. URL `https://doi.org/10.1007/978-1-4020-6774-7_5`.

Richardson, P. L., Worthington, L. V., and Cheney, R. E. A census of Gulf Stream rings, spring 1975. *Journal of Geophysical Research*, 83(8):6136–6144, 1978. doi: 10.1029/JC083iC12p06136.

Robinson, A. R., editor. *Eddies in Marine Science*. Springer Berlin Heidelberg, Berlin, Heidelberg, 1983. ISBN 978-3-642-69005-1. doi: 10.1007/978-3-642-69003-7.

Roessler, A., Rhein, M., Kieke, D., and Mertens, C. Long-term observations of North Atlantic Current transport at the gateway between western and eastern Atlantic. *Journal of Geophysical Research: Oceans*, 120(6):4003–4027, 2015. doi: 10.1002/2014JC010662.

Rossby, T. The North Atlantic Current and surrounding waters: At the crossroads. *Reviews of Geophysics*, 34(4):463, 1996. doi: 10.1029/96RG02214.

Saenko, O. A. Strong eddy compensation for the Gulf Stream heat transport. *Geophysical Research Letters*, 42(24):10739–10744, 2015. doi: 10.1002/2015GL066111.

Schanze, J. J., Schmitt, R. W., and Yu, L. L. The global oceanic freshwater cycle: A state-of-the-art quantification. *Journal of Marine Research*, 68(3):569–595, 2010. doi: 10.1357/002224010794657164.

Schlax, M. G. and Chelton, D. B. The "Growing Method" of Eddy Identification and Tracking in Two and Three Dimensions. *College of Earth, Ocean and Atmospheric Sciences , Oregon State University, Corvallis, Oregon*, 2016.

Schott, F., Stramma, L., and Fischer, J. Interaction of the North Atlantic Current with the deep Charlie Gibbs Fracture Zone throughflow. *Geophysical Research Letters*, 26(3):369–372, 1999. doi: 10.1029/1998GL900223.

Smith, G. C., Roy, F., Mann, P., Dupont, F., Brasnett, B., Lemieux, J.-F., Laroche, S., and Bélair, S. A new atmospheric dataset for forcing ice-ocean models: Evaluation of reforecasts using the Canadian global deterministic prediction system. *Quarterly Journal of the Royal Meteorological Society*, 140 (680):881–894, 2014. doi: 10.1002/qj.2194.

Smith, R. D., Maltrud, M. E., Bryan, F. O., and Hecht, M. W. Numerical Simulation of the North Atlantic Ocean at 1/10°. *Journal of Physical Oceanography*, 30(7):1532–1561, 2000. doi: 10.1175/1520-0485(2000)030<1532:NSOTNA>2.0.CO;2.

SSALTO/Duacs. A new version of SSALTO / Duacs products available in April 2014, v1.1. Technical report, CNES - Centre national d'études spatiales, Ra-

monville St Agne, France, 2014. URL http://www.aviso.altimetry.fr/fileadmin/documents/data/duacs/Duacs2014.pdf.

SSALTO/Duacs. Mesoscale Eddy Trajectory Atlas Product Handbook, v1.0. Technical report, CNES - Centre national d'études spatiales, Ramonville St Agne, France, 2017. URL https://www.aviso.altimetry.fr/fileadmin/documents/data/tools/hdbk_eddytrajectory.pdf.

Stammer, D. Global Characteristics of Ocean Variability Estimated from Regional TOPEX/POSEIDON Altimeter Measurements. *Journal of Physical Oceanography*, 27(8):1743–1769, 1997. doi: 10.1175/1520-0485(1997)027<1743:GCOOVE>2.0.CO;2.

Stendardo, I., Rhein, M., and Hollmann, R. A high resolution salinity time series 1993-2012 in the North Atlantic from Argo and Altimeter data. *Journal of Geophysical Research: Oceans*, 121(4):2523–2551, 2016. doi: 10.1002/2015JC011439.

Sun, W., Dong, C., Wang, R., Liu, Y., and Yu, K. Vertical structure anomalies of oceanic eddies in the Kuroshio Extension region. *Journal of Geophysical Research: Oceans*, 122(2):1476–1496, 2017. doi: 10.1002/2016JC012226.

Swart, S., Speich, S., Ansorge, I. J., and Lutjeharms, J. R. E. An altimetry-based gravest empirical mode south of Africa: 1. Development and validation. *Journal of Geophysical Research*, 115(C3):1–19, 2010. doi: 10.1029/2009JC005299.

Trenberth, K. E. and Solomon, A. The global heat balance: heat transports in the atmosphere and ocean. *Climate Dynamics*, 10(3):107–134, 1994. doi: 10.1007/BF00210625.

Vallis, G. K. *Athmospheric and oceanic fluid dynamics, Fundamental and large-scale circulation*. Cambridge University Press, Cambridge, U.K., 2006. ISBN 9780521849692. doi: 10.2277/0521849691.

Visbeck, M. Deep velocity profiling using lowered acoustic Doppler current profilers: Bottom track and inverse solutions. *Journal of Atmospheric and Oceanic Technology*, 19(5):794–807, 2002. doi: 10.1175/1520-0426(2002)019<0794:DVPULA>2.0.CO;2.

Volkov, D. L., Lee, T., and Fu, L. L. Eddy-induced meridional heat transport in the ocean. *Geophysical Research Letters*, 35(20):L20601, 2008. doi: 10.1029/2008GL035490.

Wang, J., Flierl, G. R., LaCasce, J. H., McClean, J. L., and Mahadevan, A. Reconstructing the Ocean's Interior from Surface Data. *Journal of Physical Oceanography*, 43(8):1611–1626, 2013. doi: 10.1175/JPO-D-12-0204.1.

Waugh, D. W. and Abraham, E. R. Stirring in the global surface ocean. *Geophysical Research Letters*, 35(20):L20605, 2008. doi: 10.1029/2008GL035526.

Weiss, J. The dynamics of enstrophy transfer in two-dimensional hydrodynamics. *Physica D: Nonlinear Phenomena*, 48(2-3):273–294, 1991. doi: 10.1016/0167-2789(91)90088-Q.

White, M. A. and Heywood, K. J. Seasonal and interannual changes in the North Atlantic subpolar gyre from Geosat and TOPEX/POSEIDON altimetry. *Journal of Geophysical Research*, 100(C12):24931, 1995. doi: 10.1029/95JC02123.

Wunsch, C. Where do ocean eddy heat fluxes matter? *Journal of Geophysical Research: Oceans*, 104(C6):13235–13249, 1999. doi: 10.1029/1999JC900062.

Wunsch, C. What Is the Thermohaline Circulation? *Science*, 298(5596):1179–1181, 2002. doi: 10.1126/science.1079329.

Wunsch, C. The total meridional heat flux and its oceanic and atmospheric partition. *Journal of Climate*, 18(21):4374–4380, 2005. doi: 10.1175/JCLI3539.1.

Wyrtki, K., Magaard, L., and Hager, J. Eddy energy in the oceans. *Journal of Geophysical Research*, 81(15):2641, 1976. doi: 10.1029/JC081i015p02641.

Yang, Q., Dixon, T. H., Myers, P. G., Bonin, J., Chambers, D., and van den Broeke, M. R. Recent increases in Arctic freshwater flux affects Labrador Sea convection and Atlantic overturning circulation. *Nature Communications*, 7:10525, 2016. doi: 10.1038/ncomms10525.

Zhang, Z., Zhang, Y., Wang, W., and Huang, R. X. Universal structure of mesoscale eddies in the ocean. *Geophysical Research Letters*, 40(14):3677–3681, 2013. doi: 10.1002/grl.50736.

Zhang, Z., Wang, W., and Qiu, B. Oceanic mass transport by mesoscale eddies. *Science*, 345(6194):322–324, 2014. doi: 10.1126/science.1252418.

Zweng, M. M., Reagan, J. R., Antonov, J. I., Locarini, R. A., Mishonov, A. V., Boyer, T. P., Garcia, H. E., Baranova, O. K., Johnson, D. R., Seidov, D.,

and Biddle, M. M. Salinity. In Levitus, S. and Mishonov, A., editors, *World Ocean Atlas 2013*, volume 2, page 39 pp. NOAA Atlas NESDIS 74, 2013. URL `http://www.nodc.noaa.gov/OC5/indprod.html`.

List of Publications

Results from this work have been published in the *Journal of Geophysical Research*:

Müller, V., D. Kieke, P. G. Myers, C. Pennelly, and C. Mertens (2017), Temperature flux carried by individual eddies across 47°N in the Atlantic Ocean, *J. Geophys. Res. Oceans*, 122, 2441–2464, doi:10.1002/2016JC012175.

Preliminary results were presented at the following international conferences:

Müller, V., I. Stendardo, D. Kieke, P. G. Myers, C. Pennelly, M. Rhein, and R. Steinfeldt, Volume heat and freshwater fluxes carried by eddies across 47°N in the Atlantic Ocean, *EGU General Assembly 2017*, Vienna, Austria, 23 - 28 April 2017. (poster)

Müller, V., D. Kieke, P. G. Myers, C. Pennelly, and C. Mertens, Eddy induced temperature flux across 47°N - observations vs. model, *EGU General Assembly 2016*, Vienna, Austria, 17 - 22 April 2016. (poster)

Müller, V., D. Kieke, P. G. Myers, C. Pennelly, and C. Mertens, Eddy-induced Temperature Exchange between the Subpolar and the Subtropical Gyre of the North Atlantic in observations and model, *Ocean Sciences Meeting 2016*, New Orleans, LA, USA, 21 - 26 February 2016. (talk)

Müller, V., D. Kieke, P. G. Myers, and C. Mertens, Eddy-induced temperature exchange between subpolar and subtropical gyre, *IGR Symposium 2015*, Edmonton, AB, Canada, 29 October 2015. (talk)

Müller, V., D. Kieke, P. G. Myers, and C. Mertens, Eddy-induced Temperature Exchange between the Subpolar and the Subtropical Gyre of the North Atlantic, *VITALS Conference 2015*, Halifax, NS , Canada, 19 - 21 October 2015. (talk)

Müller, V., D. Kieke, P. G. Myers, Eddy induced temperature flux in the Subpolar Gyre, *EGU General Assembly 2015*, Vienna, Austria, 12 - 17 April 2015. (poster)

Acknowledgments

First of all I want to thank my supervisor Dagmar Kieke. Dagmar, I don't know where I would be right now without your support and guidance, but I am fairly sure I would not have finished this thesis (at least not in this decade). You were always a great help with any questions regarding science, and I have benefited greatly from your knowledge and ideas. At the same time you gave me the freedom and opportunity to bring my own thoughts and questions to the table, and frame the project according to my own ideas and preferences. More importantly, you were a steadying influence in times when the stress was rising and I felt like everything might just be a bit too much. You showed me that there is not just "the one right way" of having a career in science. Sometimes all it took was some fresh air, the endless vastness of the North Atlantic and the smell of salt in the air to realize that I was exactly where I wanted to be.

I also want to thank Paul G. Myers for all his insightful comments on my work and especially for giving me the opportunity to come to Canada and be part of his research group at the University of Alberta. During my time in Canada I learned a lot about ocean models, hockey, bear spray, and what "winter" really means. Thanks also to the whole Numerical Modeling group at the UofA. You were so welcoming and and made it super easy to get started in a new place. Thank you Xianmin and Clark for providing the model runs and helping me with all model related questions.

I also want to express my gratitude to the International Graduate School ArcTrain, especially Michal Kucera and Gabriella Wehr. Doing my PhD project within the framework of ArcTrain was an absolute piece of good fortune. I got the chance to participate in numerous seminars, workshops, retreats and conferences, that were made possible through ArcTrain and I got to learn a lot about research outside of my own field. I also got to spend three months in Canada, which was a valuable experience. Most of all though, I cherish all the new people from all over the world I met through ArcTrain. Sharing these three and a

half years with you people was amazing. The time that we experienced together, talking (sometimes even about science), traveling to the Torngat Mountains and Banff together, meeting Polar Bears and seeing the Northern Lights, is something I will never forget.

Last but not least I want to mention my lunch crew for being there every day and allowing my brain to catch a break and I want to (and have to) thank my good friends and family for their patience with me during the time of writing this thesis and for their endless support, distraction and understanding.

Funding and Data Acknowledgments

This study was supported by the Deutsche Forschungsgemeinschaft (DFG) through the International Research Training Group "Processes and impacts of climate change in the North Atlantic Ocean and the Canadian Arctic" (IRTG 1904 ArcTrain). NOAA Optimum Interpolation (Reynolds) Sea Surface Temperatures (`https://www.ncdc.noaa.gov/oisst`) have been obtained in netCDF file format by the Integrated Climate Data Center (ICDC, `http://icdc.cen.uni-hamburg.de`), University of Hamburg, Hamburg, Germany. The altimeter products were produced by Ssalto/Duacs and distributed by AVISO, with support from Cnes (`http://www.aviso.altimetry.fr/duacs/`). The Mesoscale Eddy Trajectory Atlas products were produced by SSALTO/DUACS and distributed by AVISO+ (http://www.aviso.altimetry.fr/) with support from CNES, in collaboration with Oregon State University with support from NASA. The research was enabled in part by support provided by WestGrid (`http://www.westgrid.ca`) and Compute Canada (`http://www.computecanada.ca`). The Argo data were collected and made freely available by the International Argo Program and the national programs that contribute to it. (`http://www.argo.ucsd.edu`, `http://argo.jcommops.org`). The Argo Program is part of the Global Ocean Observing System. The subset of quality controlled Argo data from the North Atlantic used in this thesis was provided by Birgit Klein, Federal Institute of Hydrography (BSH), Hamburg, Germany. The data was downloaded from the Coriolis data repository on 5 February 2013. Support for the cruises came from the Co-Operative Project "RACE - Regional Atlantic Circulation and Global Change", and Co-Operative Project "Nordatlantik", all funded by the German Federal Ministry or Education and Research (BMBF), as well as the DFG through the Senate Commission on Oceanography. The model output was provided by Xianmin Hu (University of Alberta) and Clark Pennelly (University of Alberta). The LADCP data was

provided by Christian Mertens (University of Bremen). The ADT data as well as the scripts to compute temperature and salinity fields with the GEM method were provided by Ilaria Stendardo (University of Bremen), and the interpolation routines to merge the different GEM regions were provided Reiner Steinfeldt (University of Bremen). I want to thank Francesco Nencioli (Plymouth Marine Laboratory) for his helpful advice on using the eddy detection algorithm.